

---

**Hurricane Weather Research and  
Forecasting (HWRF) Model:  
2018 Scientific Documentation**

**November, 2018**

**Mrinal K Biswas<sup>1</sup>, Sergio Abarca<sup>3,6</sup>, Ligia Bernardet<sup>2</sup>, Isaac  
Ginis<sup>4</sup>, Evelyn Grell<sup>5</sup>, Michael Iacono<sup>8</sup>, Evan Kalina<sup>2</sup>, Bin  
Liu<sup>3,6</sup>, Qingfu Liu<sup>3</sup>, Timothy Marchok<sup>7</sup>, Avichal Mehra<sup>3</sup>,  
Kathryn Newman<sup>1</sup>, Jason Sippel<sup>8</sup>, Vijay Tallapragada<sup>3</sup>, Biju  
Thomas<sup>3,6</sup>, Weiguo Wang<sup>3,6</sup>, Henry Winterbottom<sup>3</sup>, and Zhan  
Zhang<sup>3,6</sup>**

<sup>1</sup>National Center for Atmospheric Research and Developmental Testbed Center, Boulder, CO, <sup>2</sup>University of Colorado Cooperative Institute for Research in Environmental Sciences at the NOAA Earth System Research Laboratory/Global Systems Division and Developmental Testbed Center, <sup>3</sup>NOAA/NWS/NCEP Environmental Modeling Center, College Park, MD, <sup>4</sup>University of Rhode Island, <sup>5</sup>University of Colorado Cooperative Institute for Research in Environmental Sciences at the NOAA Earth System Research Laboratory/Physical Systems Division and Developmental Testbed Center, <sup>6</sup>I. M. Systems Group Inc., Rockville, MD, <sup>7</sup>Geophysical Fluid Dynamics Laboratory, Princeton, NJ, <sup>8</sup>Hurricane Research Division, AOML, Miami, FL, RSMAS, CIMAS, University of Miami, Miami, FL., <sup>8</sup>Atmospheric and Environmental Research,

## Table of Contents

<b>1.0</b>	<b>Introduction .....</b>	<b>1</b>
1.1	2018 HWRF Upgrades .....	4
1.2	Document Overview .....	5
1.3	Future HWRF Direction .....	6
<b>2.0</b>	<b>HWRF Initialization .....</b>	<b>11</b>
2.1	Introduction .....	11
2.2	HWRF cycling system .....	11
2.3	Bogus vortex used to correct weak storms .....	15
2.4	Correction of vortex in previous 6-h HWRF or GDAS forecast .....	15
2.5	Data assimilation with GSI in HWRF .....	27
<b>3.0</b>	<b>Ocean and wave components in HWRF .....</b>	<b>38</b>
3.1	Introduction .....	38
3.2	MPIPOM-TC Overview .....	38
3.3	Purpose .....	41
3.4	Grid size, spacing, configuration, arrangement, coordinate system, and numerical scheme .....	41
3.5	Initialization .....	42
3.6	Physics and dynamics .....	45
3.7	Coupling .....	45
3.8	Output fields for diagnostics .....	46
<b>4.0</b>	<b>Physics Packages in HWRF .....</b>	<b>47</b>
4.1	HWRF physics .....	47
4.2	Microphysics parameterization .....	48
4.3	Cumulus parameterization .....	50
4.4	Surface-layer parameterization .....	53
4.5	Land-surface model .....	55
4.6	Planetary boundary-layer parameterization .....	56
4.7	Atmospheric radiation parameterization .....	58
4.8	Physics interactions .....	62
<b>5.0</b>	<b>Design of Moving Nest .....</b>	<b>63</b>
5.1	Grid Structure .....	63
5.2	Moving Nest Algorithm .....	66
5.3	Fine Grid Initialization .....	66
5.4	Lateral Boundary Conditions .....	69
<b>6.0</b>	<b>Use of the GFDL Vortex Tracker .....</b>	<b>71</b>
6.1	Introduction .....	71
6.2	Design of the tracking system .....	73
6.3	Parameters used for tracking .....	78

6.4	<i>Intensity and wind radii parameters</i> .....	79
6.5	<i>Thermodynamic phase parameters</i> .....	80
6.6	<i>Detecting genesis and tracking new storms</i> .....	81
6.7	<i>Tracker output</i> .....	82
<b>7.0</b>	<b>The idealized HWRF framework</b> .....	<b>89</b>
<b>8.0</b>	<b>References</b> .....	<b>92</b>
<b>9.0</b>	<b>ACRONYMS</b> .....	<b>102</b>

## List of Figures

Figure 1-1: Simplified overview of the HWRF system as configured for operations in the Atlantic basin. Components include the atmospheric initialization (WPS and prep\_hybrid), the vortex improvement, the GSI data assimilation, the HWRF atmospheric model, the atmosphere-ocean coupler, the ocean initialization, the MPIPOM-TC, the post processor, and the vortex tracker. For storms designated as priority by the NHC, a 40-member high-resolution HWRF ensemble provides the flow-dependent background-error covariances in the HWRF – Data Assimilation System (HDAS); otherwise, the GFS ensemble is employed.....2

Figure 1-2: Tropical oceanic basins covered by the NCEP operational HWRF model for providing realtime TC forecasts. Solid boxes represent atmosphere-ocean coupled HWRF forecast domains for National Hurricane Center and Central Pacific Hurricane Center areas of responsibility. Dashed boxes are HWRF forecast domains for Joint Typhoon Warning Center areas of responsibility. ....3

Figure 1-3: Absolute intensity error (kt) as a function of forecast lead time (h) for non-homogeneous multi-year runs of several HWRF configurations in the AL basin. Operational HWRF (HWRF (07-11)) runs prior to 2012 and retrospective pre-implementation runs identified by version of the operational model (H212, H213, H214, H215, H216, and H217) are shown. The dashed lines show the HFIP baseline (BASE), and the 5-, and 10-year HFIP goals for track and intensity errors. ....5

Figure 1-4: Proposed future operational coupled hurricane forecast system. The left/right parts of the diagram refer to the responsibilities of the NWS and National Ocean Service (NOS), respectively.....9

Table 1-1. Operational HWRF upgrades from 2013-2018 ..... 10

Figure 2-1: Simplified flow diagram for HWRF vortex initialization describing a) the split of the HWRF forecast between vortex and environment, b) the split of the background fields between vortex and analysis, and c) the insertion of the corrected vortex in the environmental field..... 14

Figure 2-2: HWRF data assimilation and model forecast domains. The blue region is the outer 13.5-km domain. The purple solid boxes show the sizes of the vortex-following 4.5-km and 1.5-km domains, while the black dashed lines are the ghost domains for d02 and d03. The red box is the unifies Atlantic MPIPOM-TC domain..... 30

Figure 2-3: NOAA TDR radial velocities between 800 hPa and 700 hPa assimilated at 12 Z on August 29, 2010..... 34

Figure 2-4: Flow diagram of self-cycled HWRF ensemble hybrid data-assimilation systems. The system is not supported with the HWRF 4.0a public release. .... 37

Table 3-1. . Ocean model, ocean initialization data, and wave model used in operations and available in the HWRF v4.0a public release. Capabilities of the public release are broken down between the default and experimental options. FB stands for

feature-based initialization, discussed later in this chapter. Wave model is not supported with the public release. ....	39
Figure 3-4: History of MPIPOM-TC development (adapted from Yablonsky et al. 2015a)....	41
Figure 3-5: MPIPOM-TC worldwide ocean domains.....	42
Figure 4-1: Water species used internally in the FA microphysics and their relationship to the total condensate. The left column represents the quantities available inside the microphysics scheme (mixing ratios of vapor, ice, snow, rain, and cloud water). The right column represents the quantities available in the rest of the model: only the water vapor and the total condensate are advected. After advection is carried out, the total condensate is redistributed among the species based on fractions of ice and rain water. ....	50
Figure 4-2: Six-h forecast of fractional area of deep updrafts over the parent domain (18-km grid spacing, top left), middle nest (6 km, top right), and innermost nest (2 km, bottom left) from a simulation of Hurricane Sandy initialized at 2012102600..	52
Figure 4-4: Sea-surface drag coefficient $C_d$ (left), and heat exchange coefficient $C_k$ (right), as a function of wind speed at 10 m above the surface for the 2017 HWRF model (magenta curve), comparing with the 2015 (blue curve) and 2016 (red curve) HWRF versions, together with various observational evidence. ....	55
Figure 4-5: RH-crit as a function of model grid spacing, $\Delta x$ (solid lines; bottom/left axes) for land (red curve) and ocean (blue curve) points. Fractional cloudiness as a function RH (dashed lines; top/right axes) following Sundqvist et al. (1989). The starting value on the ordinate represents RH-crit. ....	61
Figure 5-1: Schematic rotated latitude and longitude grid. The blue dot is the rotated latitude-longitude coordinate origin. The origin is the cross point of the new coordinate equator and zero meridian, and can be located anywhere on Earth.	64
Figure 5-2: An example of model topography differences for domains at 18- (blue) and 2-km (red) resolutions, respectively. The cross section is along latitude $\sim 22^\circ\text{N}$ , between longitudes $\sim 85^\circ\text{W}$ and $\sim 79^\circ\text{W}$ . The biggest differences are in the mountainous areas of Eastern Cuba. ....	65
Figure 5-3: An illustration of the vertical interpolation process and mass balance. Hydrostatic balance is assumed during the interpolation process.....	68
Figure 5-4: The schematic E-grid refinement - dot points represent mass grid. Big and small dots represent coarse- and fine-resolution grid points, respectively. The black square represents the nest domain. The diamond square on the right side is composed of four big-dot points representing the bilinear interpolation control points. ....	68
Figure 5-5: Lateral boundary-condition buffer zone - the outmost column and row are prescribed by external data from either a global model or regional model. The blending zone is an average of data prescribed by global or regional models and those predicted in the HWRF domain. Model integration is the solution predicted by HWRF. $\Delta\psi$ and $\Delta\lambda$ are the grid increment in the rotated latitude-longitude coordinate. ....	69

Figure 6-1: Mean sea-level pressure (contours, mb), 850-mb relative vorticity (shaded,  $s^{-1} \times 10^5$ ) and 850-mb winds (vectors,  $ms^{-1}$ ) from the NCEP GFS analysis for Tropical Storm Debby, valid at 06 UTC 24 August 2006. The triangle, diamond, and square symbols indicate the locations at which the GFDL vortex tracker identified the center position fix for each of the three parameters. The notation to the left of the synoptic plot indicates that the distance between the 850-mb vorticity center and the mslp center is 173 km..... 72

Figure 7.1. Vertical structure of the pressure-sigma coordinate used to create the idealized vortex..... 89

## List of Tables

Table 1-1. Operational HWRF upgrades from 2013-2018 .....	10
Table 3-1. Ocean model, ocean initialization data, and wave model used in operations and available in the HWRF v4.0a public release. Capabilities of the public release are broken down between the default and experimental options. FB stands for feature-based initialization, discussed later in this chapter. Wave model is not supported with the public release. ....	39

*If significant help was provided via the HWRF Scientific Documentation for work resulting in a publication, please acknowledge this document.*

**How to cite this document:**

Biswas M. K., S. Abarca, L. Bernardet, I. Ginis, E. Grell, M. Iacono, E. Kalina, B. Liu, Q. Liu, T. Marchok, A. Mehra, K. Newman, J. Sippel, V. Tallapragada, B. Thomas, W. Wang, H. Winterbottom, and Z. Zhang, 2018: Hurricane Weather Research and Forecasting (HWRF) Model: 2018 Scientific Documentation, Available at <https://dtcenter.org/HurrWRF/users/docs/index.php>

## **Acknowledgments**

The authors wish to acknowledge the Development Testbed Center (DTC) for facilitating the coordination of writing this document amongst the following institutions: NOAA/NWS/NCEP Environmental Modeling Center; NOAA/ESRL Global Systems Division; NOAA/AOML Hurricane Research Division; NOAA/OAR Geophysical Fluid Dynamics Laboratory; IM Systems Group Inc.; Graduate School of Oceanography, University of Rhode Island; RSMAS/CIMAS, University of Miami; and CIRES University of Colorado, Boulder, CO. Thanks to Sundararaman Gopalakrishnan, Young Kwon, Dmitry Sheinin, Subashini Subramanian, Mingjing Tong, Samuel Trahan, Richard Yablonsky, Xuejin Zhang, and Robert Tuleya for contributing to the documentation in the earlier versions. Thanks to Karen Slater of NCAR for her desktop publishing expertise in the preparation of this document.

## 1. INTRODUCTION

The Hurricane Weather Research and Forecast (HWRF) system has been in operation at the National Oceanic and Atmospheric Administration's (NOAA) National Centers for Environmental Prediction (NCEP) since 2007. The HWRF system was developed jointly by NCEP's Environmental Modeling Center (EMC) and NOAA's Geophysical Fluid Dynamics Laboratory (GFDL) and Atlantic Oceanographic and Meteorological Laboratory (AOML), and has received numerous contributions from the research community, notably from the University of Rhode Island (URI). The current release is Version 4.0a.

The purpose of this document is to describe the scientific aspects of the HWRF model. This includes the initialization, ocean coupling, physics schemes, moving nests, GFDL tracker, and idealized simulation. To learn how to run the HWRF model, please refer to the HWRF Users' Guide (Biswas et al. [2018]).

The HWRF system includes the WRF (Weather Research and Forecasting) model software infrastructure, the Non-Hydrostatic Mesoscale Model on the E Grid (NMM-E) dynamic core, the Message Passing Interface Princeton Ocean Model-Tropical Cyclone (MPIPOM-TC), and the NCEP coupler. HWRF employs a suite of advanced physical parameterizations developed for tropical cyclone applications. These include the GFDL surface-layer parameterization to account for air-sea interaction over warm water and under high-wind conditions, the Noah Land Surface Model (LSM), the Rapid Radiative Transfer Model for GCMs (RRTMG) radiation scheme, the Ferrier-Aligo microphysical parameterization, the Global Forecast System (GFS) Hybrid Eddy Diffusivity Mass-Flux (Hybrid-EDMF) Planetary Boundary Layer (PBL) scheme, and the scale-aware GFS Simplified Arakawa Schubert (SASAS) deep and shallow convection schemes. The Hybrid Coordinate Ocean Model (HYCOM) is now used operationally for the northern West Pacific (WP), North Indian Ocean (NIO), and Southern Hemisphere ocean basins. However, the only ocean model supported with the HWRF v4.0a public release is MPIPOM-TC. Figure 1-1 illustrates all components of HWRF supported by the Developmental Testbed Center (DTC), which also includes the WRF Preprocessing System (WPS), *prep\_hybrid* (used to process spectral coefficients of the Global Data Assimilation System [GDAS] and GFS in their native vertical coordinates), a sophisticated vortex-initialization package designed for HWRF, the regional hybrid Ensemble Kalman Filter (EnKF) — three-dimensional variational data assimilation system (3D-VAR) Gridpoint Statistical Interpolation (GSI), the NCEP Unified Post-Processor (UPP), and the GFDL vortex tracker. However, the one-way coupled Wave Watch III (WW3) wave model used for storm-surge prediction and HYCOM coupling is not supported by the DTC.

HWRF is an atmosphere-ocean model customized for hurricane/tropical storm applications. It is configured with a parent grid and two telescopic, high-resolution, movable 2-way nested grids that follow the storm, using a unique physics suite and diffusion treatment. The HWRF also contains a sophisticated initialization of both the ocean- and the storm-scale circulation.

Unlike other NCEP forecast systems that run continuously throughout the year, the HWRF hurricane model is launched for operational use only when the National Hurricane Center (NHC) or Joint Typhoon Warning Center (JTWC) determines that a disturbed area of weather has the potential to evolve into a depression anywhere over their area of responsibility. After an initial HWRF run is triggered, new runs are launched in cycled mode at 6-h intervals until the storm dissipates after making landfall, becomes extra-tropical, or degenerates into a remnant low, typically identified when convection becomes disorganized around the center of circulation. Currently, the HWRF model is run by NCEP Central Operations (NCO) for all global tropical cyclone basins, four times daily throughout the year, producing 126-h forecasts of Tropical Cyclone (TC) track, intensity, structure, and rainfall to meet operational forecast and warning process objectives.

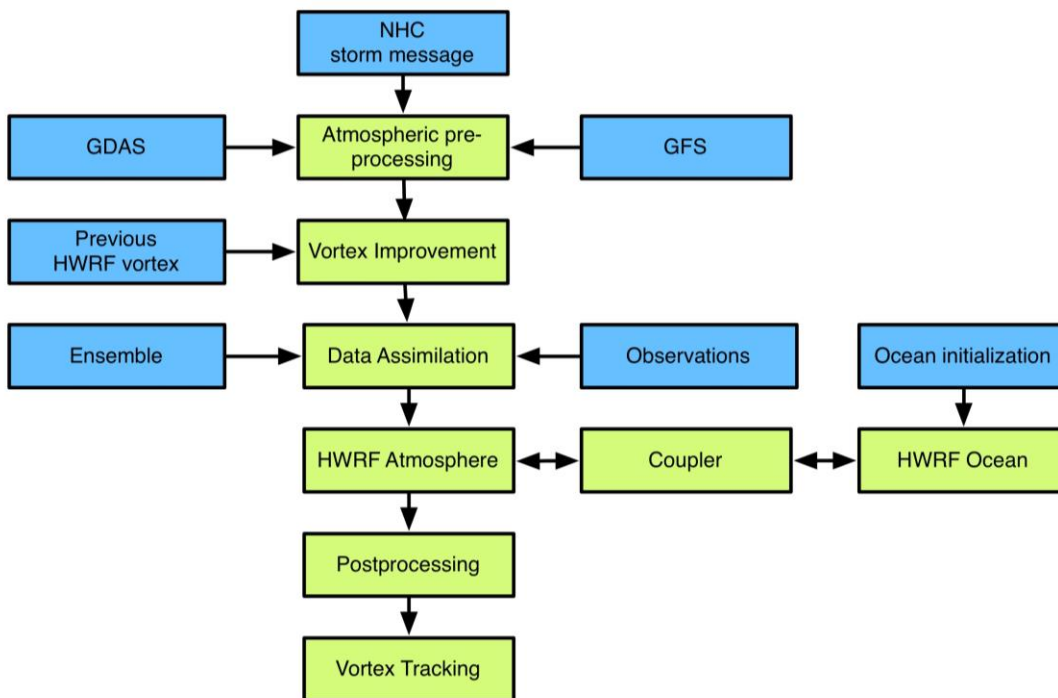


Figure 1-1: Simplified overview of the HWRF system as configured for operations in the Atlantic basin. Components include the atmospheric initialization (WPS and prep\_hybrid), the vortex improvement, the GSI data assimilation, the HWRF atmospheric model, the atmosphere-ocean coupler, the ocean initialization, the MPIPOM-TC, the post processor, and the vortex tracker. For storms designated as priority by the NHC, a 40-member high-resolution HWRF ensemble provides the flow-dependent background-error covariances in the HWRF – Data Assimilation System (HDAS); otherwise, the GFS ensemble is employed.

Figure 1-2 shows the regions for which the HWRF model is currently operated in real time.

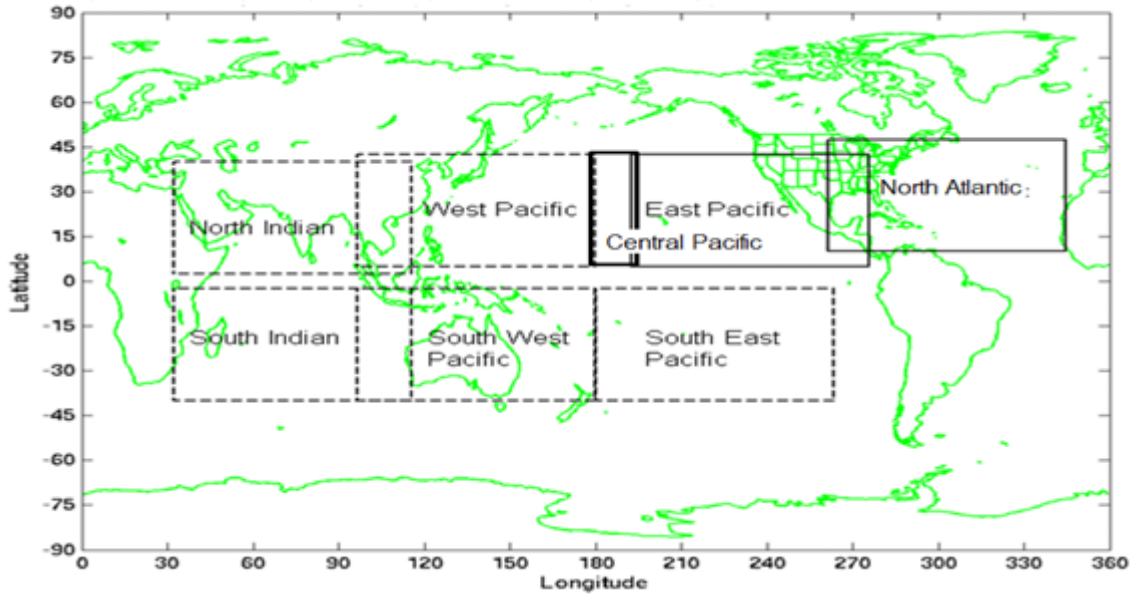


Figure 1-2: Tropical oceanic basins covered by the NCEP operational HWRF model for providing realtime TC forecasts. Solid boxes represent atmosphere-ocean coupled HWRF forecast domains for National Hurricane Center and Central Pacific Hurricane Center areas of responsibility. Dashed boxes are HWRF forecast domains for Joint Typhoon Warning Center areas of responsibility.

Upgrades to the HWRF system are performed on an annual basis depending on the retrospective testings and upgrades to GDAS and the GFS, which provide initial and boundary conditions for HWRF. Every year, prior to the start of the Eastern North Pacific basin (EP) and Atlantic basin (AL) hurricane seasons (15 May and 1 June, respectively), HWRF upgrades are approved by the NHC and implemented by NCO so that NHC forecasters have improved hurricane guidance at the start of each new hurricane season. These upgrades are chosen based on extensive testing and evaluation (T&E) of retrospective forecasts for at least three recent past hurricane seasons.

HWRF development typically occurs in two phases. The first phase focuses on developmental testing, which occurs prior to and during the hurricane season (roughly 1 April to 30 October) when potential upgrades to the system are tested individually in a systematic and coordinated manner. The pre-implementation testing starts in November and is designed to evaluate the most promising developments assessed in the development phase to define the HWRF configuration for the upcoming hurricane season. The results of the pre-implementation testing must be completed and the final HWRF configuration frozen by 15 March for each annual upgrade. Once frozen, the system is handed off to NCO for implementation by approximately 1 June. The cycle is then repeated for the next set of proposed upgrades to the HWRF system. During the hurricane season (1 June to 30 November) no changes are made to the operational HWRF so that forecasters are provided with consistent and documented numerical guidance performance characteristics.

The public release of HWRF includes many research capabilities (e.g., idealized simulations running with alternate physics options, running HWRF with alternate configurations, etc.). The v4.0 also includes capability to run with GFS Finite Volume

Cubed (FV3) output. These capabilities are described in detail in the HWRf Users' Guide (Biswas et al. 2018).

## 1.1 2018 HWRf Upgrades

Many updates to the HWRf modeling system were implemented in preparation for the 2018 hurricane season following the annual upgrade plans designed at EMC and supported by the Hurricane Forecast Improvement Program (HFIP). A brief description of model upgrades for the 2018 hurricane season is provided below:

***HWRf Infrastructure/Resolution Upgrades:*** The NMM core of the operational HWRf model was upgraded to the latest community version referred to as V4.0. Previously, the model resolution consisted of grids at 18-, 6-, and 2-km resolution. In the current configuration, the resolution was improved to 13.5-, 4.5-, and 1.5-km for the parent domain, intermediate nest, and innermost domain, respectively. The parent domain covers approximately  $77.2^\circ \times 77.2^\circ$ , while the intermediate domain covers  $\sim 17.8^\circ \times \sim 17.8^\circ$  and the innermost domain  $\sim 5.9^\circ \times \sim 5.9^\circ$ . This represents a slight decrease in areal coverage for the two model nests, compared to the 2017 configuration, but at higher resolution. In the vertical, the model has 75 levels for all ocean basins, with the model top at 10 hPa.

***HWRf Physics Upgrades:*** HWRf physics schemes were upgraded to include a new cloud overlap method in the RRTMG scheme and to adjust the horizontal diffusion and convergence damping coefficients.

***HWRf Data Assimilation System (HDAS) Upgrades:*** New observations (GOES-16 AMVs, NOAA-20, SFMR, TDR from G-IV) are now assimilated using an upgraded GSI system. The dropsonde drifting is also considered when assimilation is done.

***HWRf Post-Processing and Product Upgrades:*** HWRf post-processing upgrades include changes in file names to reflect the resolution change and adding the precipitation rate variable (PRATE) in GRIB2 files.

***Ocean Upgrades:*** A new POM domain was included for the CPAC basin. HYCOM is now used for ocean coupling in the Southern Hemisphere basins with RTOFS initialization, but HYCOM is not supported in this public release.

***Tracker Upgrades:*** Updates to the GFDL vortex tracker include the capability to use NetCDF files as tracker input. However, the HWRf system uses GRIB files as input to the tracker.

Pre-implementation tests showed a reduction in track and intensity forecast errors when the 2018 HWRf configuration was tested. A non-homogeneous comparison of various versions of the operational HWRf (Fig. 1-3) illustrates improvements obtained from the operational HWRf during the last six years (2012-2017). The HWRf model's progress towards reaching the 5 and 10-year goals of HFIP through steady and systematic improvements is also highlighted.

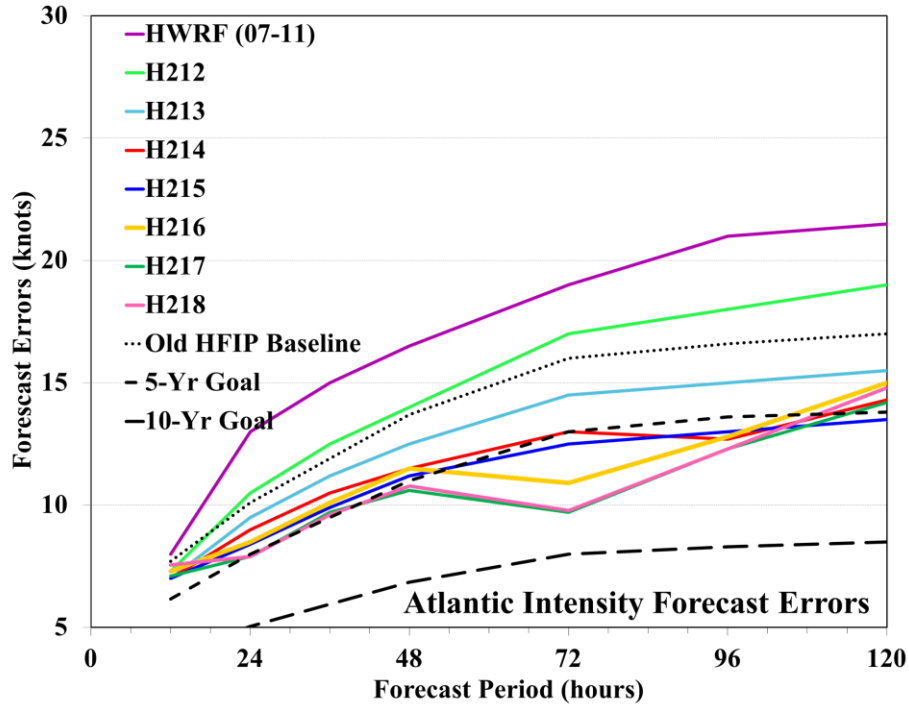


Figure 1-3: Absolute intensity error (kt) as a function of forecast lead time (h) for non-homogeneous multi-year runs of several HWRf configurations in the AL basin. Operational HWRf (HWRf (07-11)) runs prior to 2012 and retrospective pre-implementation runs identified by version of the operational model (H212, H213, H214, H215, H216, H217, and H218) are shown. The dashed lines show the HFIP baseline (BASE), and the 5-, and 10-year HFIP goals for track and intensity errors.

The list of upgrades to the HWRf for the hurricane seasons from 2011 through 2018 is available on EMC's HWRf website ([http://www.emc.ncep.noaa.gov/gc\\_wmb/vxt/HWRf/about.php?branch=impl](http://www.emc.ncep.noaa.gov/gc_wmb/vxt/HWRf/about.php?branch=impl)). Table 1.1 lists the major upgrades from 2013 onward. This documentation provides a description of HWRf v4.0a, which is functionally equivalent to the model implemented for the 2018 hurricane season, with the exception that the HYCOM, wave model, and HWRf ensemble are not supported.

The 2018 operational HWRf implemented at NCEP is a unified system for all basins, but the system is configured differently for specific basins to maximize the forecast performance based on extensive testing and evaluation. For example, the North Atlantic and eastern and central North Pacific ocean basins are coupled to the MIPOM-TC ocean model. However, the current operational HWRf configurations for WPAC and NIO, and Southern Hemispheric ocean basins are coupled to the HYCOM ocean model (initialized with RTOFS). However, the southern hemispheric basins are run in uncoupled mode because the coupled configuration has not been sufficiently tested. More details on HWRf model configurations for various basins are provided in the HWRf Users' Guide (Biswas et al. 2018).

## 1.2 Document Overview

The document covers these aspects of the HWRf system in the subsequent sections:

- HWRF initialization
- Ocean model and coupling
- HWRF moving nest
- GFDL vortex tracker
- Idealized HWRF framework

### 1.3 Future HWRF Direction

Starting with the 2011 hurricane season, all components of HWRF have been synchronized with their community code repositories to facilitate transition of developments from Research to Operations (R2O). This effort, led by the DTC, has fostered closer collaboration among HWRF developers and allowed accelerated R2O transfers from government laboratories and academic institutions to the operational HWRF.

The major HWRF upgrades for the 2013 - 2017 hurricane seasons listed in Table 1.1 provide a solid foundation for improved tropical cyclone intensity prediction. Future upgrades to the HWRF system include aligning with the NOAA HFIP and Next-Generation Global Prediction System (NGGPS) programs' strategy for implementing advanced physics packages, such as multi-moment microphysics schemes, higher-order closure PBL schemes and scale-aware and stochastic physical parameterization schemes with a focus on improved air-sea interactions and inner-core processes.

Future advancements to atmospheric initialization include assimilation of cloudy and all-sky radiances from various satellites, and additional observations from aircraft and/or Unmanned Aerial Vehicles (UAVs). It should be noted that, to support future data-assimilation efforts for the hurricane core, NOAA acquired the G-IV aircraft in the mid-1990s to supplement the data obtained by NOAA's P-3s. The high altitude of the G-IV allows collection of observations that help define the 3-D hurricane core structure from the outflow layer to the near-surface layer. For storms approaching landfall, the coastal 88-D high-resolution radar data also are available.

To make use of these newly expanded observations, several advanced data assimilation techniques are being explored within the operational and research hurricane modeling communities, including the self-cycled EnKF-GSI hybrid method, the first version of which was implemented in HWRF in 2017. Others methods being considered include hybrid EnKF-4DVAR, hourly cycling and Incremental Analysis Updating (IAU) approaches. Improvement of hurricane initialization has become a top priority in both the research and operational communities.

Planned enhancements to the HWRF modeling infrastructure include a much larger outer domain with multiple movable grids, including more vertical levels, higher resolution of nests (resources permitting) and an eventual transition to NOAA's Environmental Modeling System (NEMS) using the National Unified Operational Prediction Capability (NUOPC) layer, which can provide a global-to-regional-to-local-scale modeling framework.

The initialization of the MIPOM-TC ocean component (i.e., the feature-based model in the Atlantic and the RTOFS initialization in the eastern North Pacific) may be replaced with the Hybrid Coordinate Ocean Model (HYCOM) in the near future to be consistent with EMC's ocean model development plan for all EMC coupled applications. The HYCOM has its own data assimilation system that includes assimilation of altimetry data and data from other remote-based and conventional *in situ* ocean data platforms. This system can also assimilate Airborne eXpendable BathyThermograph (AXBT) data obtained by NOAA's P-3s for selected storm scenarios over the Gulf of Mexico and in the Caribbean.

In 2016, HWRF was coupled to an advanced version of the NCEP wave model, the WW3. Future plans include full 3-way coupling between atmosphere, ocean, and waves to include both the dynamic and thermodynamic (via sea-spray) feedback of surface waves on air-sea processes and the ocean. Further advancement of the WW3 to a multi-grid wave model (MWW3) will incorporate 2-way interactive grids at different resolutions. Eventually, this system will be fully coupled to a dynamic storm-surge model for more accurate prediction of inundation and forecasts of waves on top of storm surge for advanced prediction of impact of landfalling storms on coasts. Moreover, the 2015 adoption of the Noah LSM in HWRF opens the door to addressing inland flooding through future coupling with hydrologic and inland inundation models.

Other refinements to the HWRF modeling system include advanced products tailored to serve Weather Forecast Offices (WFOs) along the coastal regions, enhanced model diagnostic capabilities, and high-resolution ensembles. Figure 1-4 shows the proposed fully coupled operational hurricane system, with 2-way interaction between the atmosphere-land-ocean-wave models, providing feedback to high-resolution bay and estuary hydrodynamic models that predict storm-surge inundation.

In the long-term, advancements made in the HWRF system are expected to benefit the representation of TCs and hurricanes in future NCEP modeling applications using the Finite-Volume Cubed-Sphere (FV3) dynamical core. Development of one such effort called the Hurricane and Analysis and Forecast System (HAFS) is described next.

### **1.3.1 Development of Hurricane Analysis and Forecast System (HAFS)**

One of the key strategies defined in the revised HFIP in response to the proposed framework for addressing Section 104 of the Weather Research and Forecasting Innovation Act of 2017 is to advance an operational HAFS at NOAA/NWS. HAFS will be a multi-scale model and data assimilation package capable of providing analyses and forecasts of the inner core structure of the TC out to 7 days, which is key to improving size and intensity predictions, as well as the large-scale environment known to influence the TC's motion. HAFS will provide an operational analysis and forecast system out to 7 days for hurricane forecasters with reliable, robust, and skillful guidance on TC track and intensity (including RI), storm size, genesis, storm surge, rainfall, and tornadoes associated with TCs. It will provide an advanced analysis and forecast system for cutting-edge research on modeling, physics, data assimilation, and coupling to earth-system components for high-resolution TC predictions within the outlined Next Generation

Global Prediction System (NGGPS)/Strategic Implementation Plan (SIP) objectives of the Unified Forecast System (UFS).

Some of the objectives for establishing an operational HAFS are:

- Reduce forecast guidance errors, including during RI, by 50 percent from 2017;
- Produce 7-day forecast guidance as effective as the 2017 5-day forecast guidance;
- Improve guidance on pre-formation disturbances, including genesis timing, and track and intensity forecasts, by 20 percent from 2017; and
- Improve hazard guidance and risk communication, based on social and behavioral science, to modernize the TC product suite (products, information, and services) for actionable lead-times for storm surge and all other threats.

RI remains an especially important and challenging forecast problem, particularly in moderate shear. Specific goals and metrics are defined for the prediction of the basic TC forecast parameters, new extended range forecasts, RI, and TC formation. HAFS development will be based on key strategies that will continue improving track and intensity guidance, particularly for rapid intensification, and extend the focus to improving guidance on storm size, storm surge, and all other TC hazards at actionable lead times (e.g., 48-72 hours, depending on the hazard).

HAFS development will treat the current operational HWRF system as its initial version. All future developments will primarily focus on re-engineering capabilities and functionality of existing operational HWRF and Hurricane in a Multi-scale Ocean-coupled Non-hydrostatic model (HMON) into HAFS. These include (but are not limited to):

- Vortex Initialization
- Inner Core Data Assimilation
- Physics packages
- Algorithms of moving nests in FV3
- Algorithms for telescopic nests in FV3
- Coupling FV3 to other earth-system component models (Ocean, Waves, Land, Surge, etc.) using NEMS-NUOPC infrastructure

## Hurricane-Wave-Ocean-Surge-Inundation Coupled Models

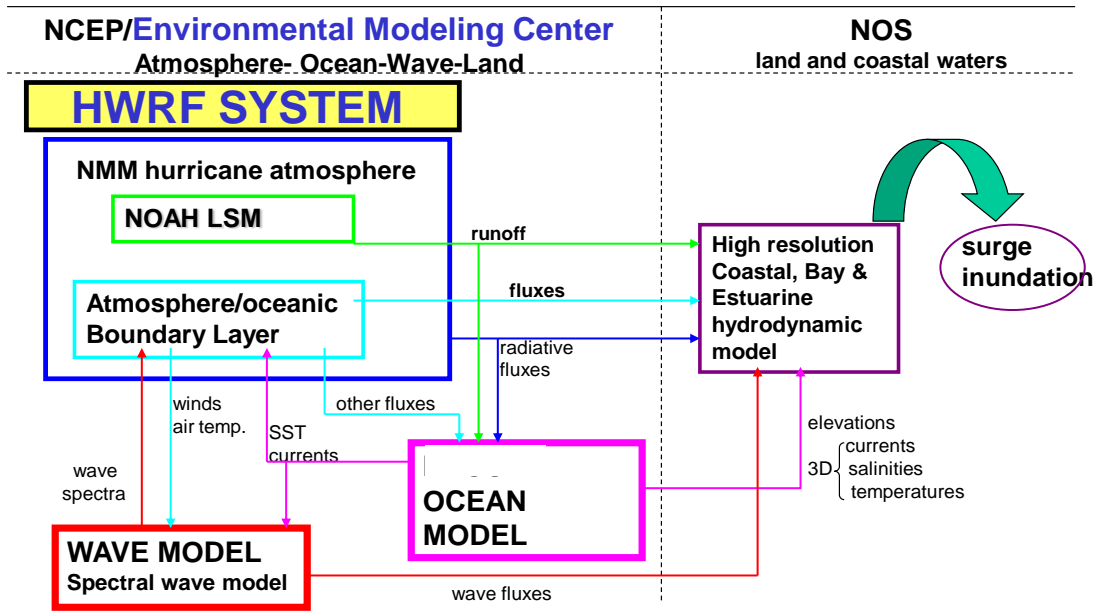


Figure 1-4: Proposed future operational coupled hurricane forecast system. The left/right parts of the diagram refer to the responsibilities of the NWS and National Ocean Service (NOS), respectively.

Table 1-1. Operational HWRF upgrades from 2013-2018

	2018	2017	2016	2015	2014	2013
<b>Domain size/resolution/vertical levels</b>	Increased resolution to 13.5/4.5/1.5 km. Reduced D02 and D03 domain size. 75 vertical levels with 10 hPa for all ocean basins.	Decreased D02 and D03 domain size, Increased vertical levels to 75, with 10 hPa model top for AL, EP and CPAC basins	Increased D02 and D03 domain size	18/6/2 km d02 domain increased by 20%	Vertical levels increased to 61, with model top at 2 hPa for AL and EP basins	
<b>Physics</b>	New cloud overlap scheme in RRTMG.	Updates to F-A microphysics, SASAS, GFS-EDMF, RRTMG and exchange coefficients in surface layer	<ul style="list-style-type: none"> <li>• SASAS scheme – enabled for all 3 domains</li> <li>• GFS-EDMF scheme</li> </ul>	<ul style="list-style-type: none"> <li>• RRTMG radiation</li> <li>• Ferrier-Aligo microphysics</li> <li>• improved PBL</li> <li>• Noah LSM</li> </ul>	Shallow convection in SAS	PBL updated to use variable critical Ri number
<b>Ocean</b>	Ocean coupling for S. Hemispheric basins.	HYCOM for WPAC and NIO basins	RTOFS initialization in the EP basin		<ul style="list-style-type: none"> <li>• MPIPOM-TC for transatlantic ocean</li> <li>• 3D coupling for E. Pac storms</li> </ul>	Improved atmospheric-ocean fluxes
<b>Nesting</b>						Nest movement tracking using GFDL vortex tracker
<b>Vortex Init</b>				Improved storm size correction		
<b>Data assimilation</b>	<ul style="list-style-type: none"> <li>• New data sets</li> <li>• Algorithm to account for dropsonde drift</li> </ul>	<ul style="list-style-type: none"> <li>• New data sets</li> <li>• Fully-cycled HWRF ensemble hybrid data assimilation when TDR present or NHC priority storm</li> <li>• Blending threshold increased to 65 kt</li> </ul>	<ul style="list-style-type: none"> <li>• Hybrid assimilation over EP basin</li> <li>• New datasets</li> </ul>	<ul style="list-style-type: none"> <li>• 40-member HWRF-based ensemble when TDR present</li> <li>• Assimilate MSLP from TCVitals</li> </ul>	Assimilation only on 9 and 3 km domains	Ensemble variational hybrid assimilation Ingest TDR data
<b>Post processing</b>	Include PRATE in GRIB2 output	New wave products		Simulated brightness temperature		
<b>Misc. (Software, additional components)</b>			One-way coupled WW3	Scripts converted to python		Allow ingestion of spectral data

## 2. HWRF INITIALIZATION

### 2.1 Introduction

Initializing hurricanes in the operational HWRF model requires several steps to prepare the analysis at various scales. The environmental fields in the parent domain are derived from the GFS analysis, and the fields in the nest domains are derived from 6-h forecasts from GDAS, enhanced through the vortex relocation and HDAS. The vortex-scale fields are generated by inserting a vortex corrected using Tropical Cyclone Vitals (TCVitals data (Trahan and Sparling [2012])), onto the large-scale fields. The vortex may originate from a GDAS 6-h forecast, from the previous HWRF 6-h forecast, or from a bogus calculation, depending on the storm intensity and on the availability of a previous HWRF forecast. Additionally, vortex-scale data assimilation is performed with conventional observations, satellite observations, and NOAA P3 Tail Doppler Radar radial velocities (when available) assimilated in the TC vortex area and its near environment. To avoid vortex spindown of strong storms (with maximum winds greater than 65 kt), a blending process is employed, causing data assimilation increments to be excluded within 150 km of the storm center and gradually reintroduced between 150–300 km.

Finally, the analyses are interpolated onto the HWRF outer domain and two inner domains to initialize the forecast.

The data assimilation systems for the GFS and for HWRF (GDAS and HDAS, respectively) follow similar procedures, but are run on different grids (global for GDAS and regional for HDAS). Both systems employ the community GSI, which is supported by the DTC.

This section discusses the details of the atmospheric initialization, while the ocean initialization is described in Section 3.

### 2.2 HWRF cycling system

The location of the HWRF outer- and inner-domain is calculated based on the observed hurricane's current and projected center position based on the NHC storm message. Therefore, if a storm is moving, the outer domain will not be in the same location for subsequent cycles.

Once the domains have been defined, the vortex replacement cycle and HDAS analysis are used to create the initial nest fields. If a previous 6-h HWRF forecast is available, and the observed intensity of the storm is greater than or equal to  $14 \text{ m s}^{-1}$ , the vortex is extracted from that forecast and corrected to be included in the current initialization. If the previous 6-hr HWRF forecast is not available, or the observed storm has a maximum wind speed of less than  $14 \text{ m s}^{-1}$ , the HDAS vortex is corrected using the vortex correction procedure and added to the current initialization.

The vortex correction process involves the following steps, partially represented in Figure 2-1:

1. Interpolate the GFS analysis fields onto the HWRF model parent grids (these data will be used in the final merge after HDAS analysis).
2. Interpolate the GDAS 6-h forecast onto the HWRF model parent grid, and interpolate this parent data onto nest grids and data-assimilation ghost grids. These ghost grid domains are created for storm (ghost d02) and inner-core environment (ghost d03) data assimilations, and have the same resolutions as the inner nests ( $0.033^\circ$  and  $0.011^\circ$ ). The domain size for ghost d02 is  $20^\circ \times 20^\circ$ , and  $11^\circ \times 11^\circ$  for ghost d03. After the data assimilation is complete, the d02 and d03 are interpolated from their respective ghost domains. More information will be described later in Section 2.5.
3. Remove the vortex from the GDAS 6-h forecast. The remaining large-scale flow is termed the “environmental field.”
4. Determine which vortex will be added to the environmental fields (create a new  $30^\circ \times 30^\circ$  dataset with  $0.011^\circ$  resolution). Check the availability of the HWRF 6-h forecast from the previous run (initialized 6 h before the current run) and the observed storm intensity.
  - a. If the previous forecast is not available:
    - i. if the observed storm maximum wind speed is greater than or equal to,  $20 \text{ m s}^{-1}$ , use a bogus vortex; or
    - ii. if the observed maximum wind speed is less than  $20 \text{ m s}^{-1}$ , use a corrected GDAS 6-h forecast vortex.
  - b. If the previous forecast is available:
    - i. if the observed maximum wind speed is greater than or equal to  $14 \text{ m s}^{-1}$ , extract the vortex from the forecast fields and correct it based on the TCVitals; or
    - ii. if the observed maximum wind speed is less than  $14 \text{ m s}^{-1}$ , use a corrected GDAS 6-h forecast vortex.
  - c. Interpolate the  $30^\circ \times 30^\circ$  new data onto ghost d02 ( $20^\circ \times 20^\circ$ ) and ghost d03 ( $11^\circ \times 11^\circ$ ) domains.

Note that for each HWRF forecast, steps 2 and 3 are performed three times: 3 h before, 3 h after, and at the HWRF initialization time. These three time levels are necessary to support the GSI First Guess at Appropriate Time (FGAT), described later in this chapter.

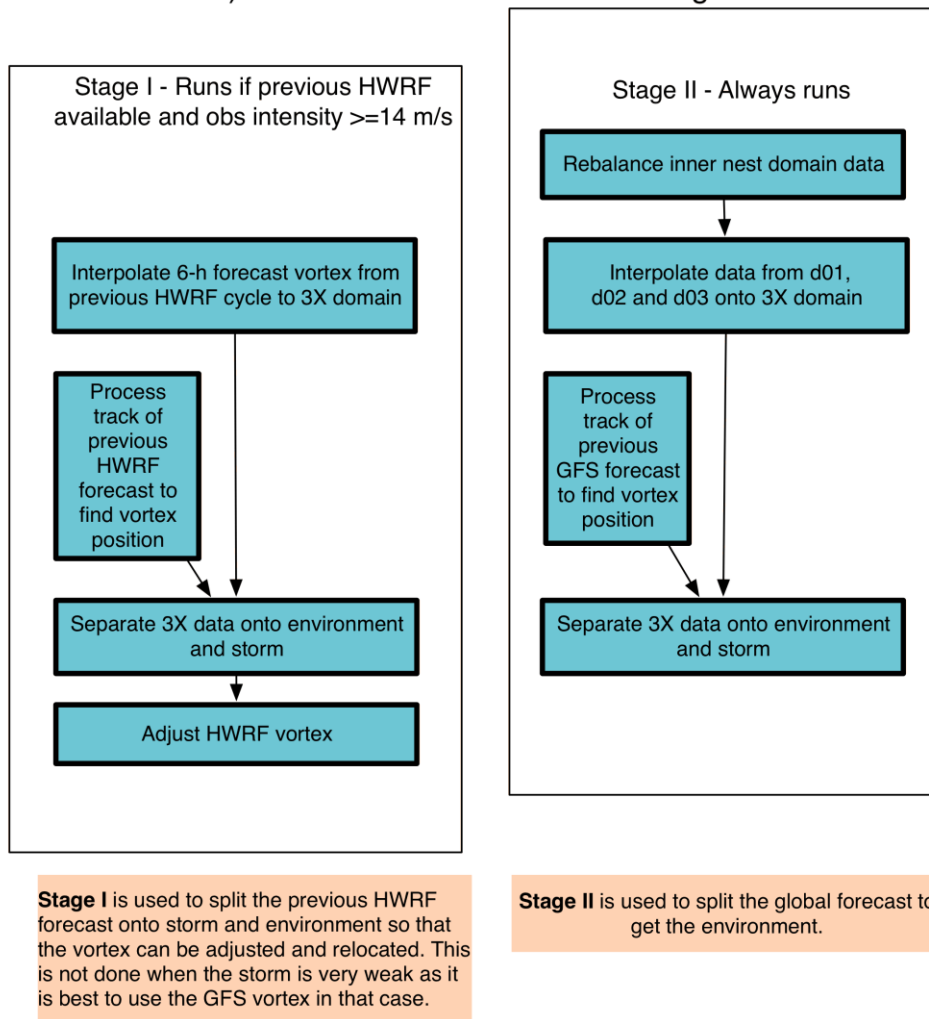
5. Perform two one-way hybrid ensemble-3DVAR GSI analyses, using all observation data and the GFS 80-member ensemble background-error

correlation, to create HDAS analysis fields for the HWRF ghost d02 and ghost d03 domains (see section 2.5).

6. Merge the data obtained from Step 5 onto the parent and nest domains, performing the blending process in which data assimilation increments for storms with maximum speed greater than 65 kt are excluded within 150 km of the storm center and gradually reintroduced between 150–300 km.

7. Run the HWRF forecast model.

#### a) HWRF Vortex Initialization - Stages I and II



## b) HWRF Vortex Initialization - Stage III - Always runs

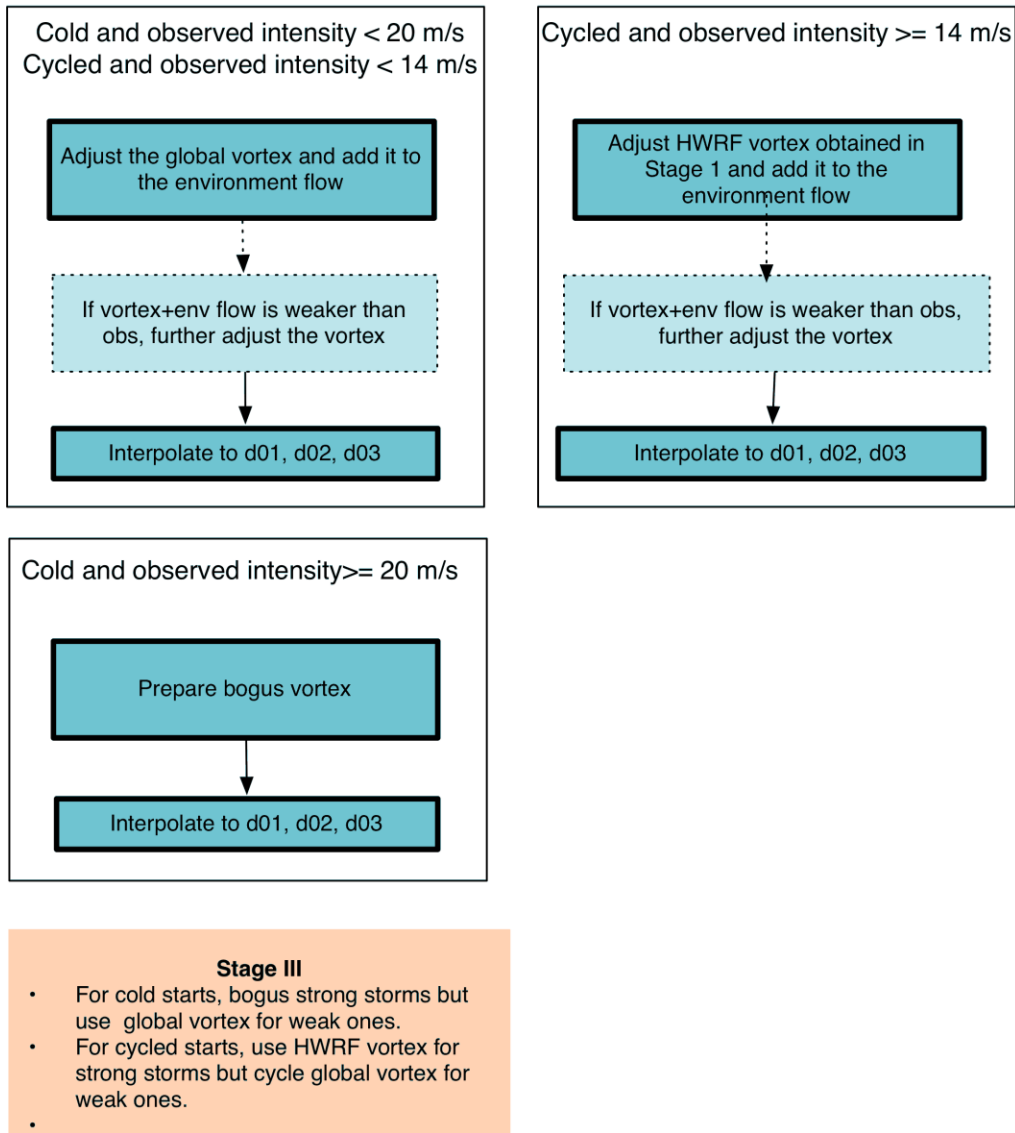


Figure 2-1: Simplified flow diagram for HWRF vortex initialization describing a) the split of the HWRF forecast between vortex and environment, b) the split of the background fields between vortex and analysis, and c) the insertion of the corrected vortex in the environmental field. The 3X in this figure denotes the  $30^{\circ} \times 30^{\circ}$  domain.

The vortex correction, described in Section 2.4, adjusts the vortex location, size, and structure based on the TCVitals:

- storm location (data used: storm-center position);
- storm size (data used: radius of maximum surface wind speed, 34-kt wind radii, and radius of the outermost closed isobar); and

- storm intensity (data used: maximum surface wind speed and, secondarily, the minimum sea-level pressure).

As noted above, a bogus vortex (described in Section 2.3) is only used in the initialization of strong storms (intensity greater than  $20 \text{ m s}^{-1}$ ) when the HWRF 6-h forecast is not available. Generally speaking, a bogus vortex does not produce the best intensity forecast. Also, cycling very weak storms (less than  $14 \text{ m s}^{-1}$ ) without inner-core data, assimilation often leads to large errors in intensity forecasts. To reduce the intensity forecast errors for cold starts and weak storms, the corrected GDAS 6-h forecast vortex is used in the operational HWRF. These changes improve the intensity forecast for the first several cycles, as well as for weak storms (less than  $14 \text{ m s}^{-1}$ ).

### 2.3 Bogus vortex used to correct weak storms

The bogus vortex discussed here is primarily used to cold-start strong storms (observed intensity greater than or equal to  $20 \text{ m s}^{-1}$ ) and to increase the storm intensity when the storm in the HWRF 6-h forecast is weaker than that of the observation (see Section 2.4.2). This procedure contrasts with previous HWRF implementations in which a bogus vortex was used in all cold starts. This change significantly improves the intensity forecasts in the first 1-3 cycles of a storm.

The bogus vortex is created from a 2-D axi-symmetric synthetic vortex generated from a past model forecast. The 2-D vortex only needs to be recreated when the model physics undergo changes that strongly affect the storm structure. Currently two composite storms are used, one created in 2007 for strong deep storms, another one created in 2012 for shallow and medium-depth storms.

For the creation of the 2-D vortex, a forecast storm (over the ocean) with small size and near axi-symmetric structure is selected. The 3-D storm is separated from its environment fields, and the 2-D axi-symmetric part of the storm is calculated. The 2-D vortex includes the hurricane perturbations of horizontal wind component, temperature, specific humidity, and sea-level pressure. This 2-D axi-symmetric storm is used to create the bogus storm.

To create the bogus storm, the wind profile of the 2-D vortex is smoothed until its RMW or maximum wind speed matches the observed values. Next, the storm size and intensity are corrected following a procedure similar to the cycled system.

The vortex in medium-depth and deep storms, receives identical treatment, while the vortex in shallow storms undergoes two final corrections: the vortex top is set to 400 hPa and the warm-core structures are removed (this shallow storm correction is only applied for a bogus storm, not for the cycled vortex).

### 2.4 Correction of vortex in previous 6-h HWRF or GDAS forecast

#### 2.4.1 Storm-size correction

Before describing the storm-size correction, some frequently used terms will be defined. Composite vortex refers to the 2-D axi-symmetric storm, which is created once and used for all forecasts. The bogus vortex is created from the composite vortex by smoothing

and performing size (and/or intensity) corrections. The background field, or guess field, is the output of the vortex initialization procedure, to which inner-core observations can be added through data assimilation. The environment field is defined as the HDAS analysis field after removing the vortex component.

For hurricane data assimilation, a good background field is needed. This background field can be the GFS analysis or, as in the operational HWRF, the previous 6-h forecast of GDAS. Storms in the background field may be too large or too small, so the storm size needs to be corrected based on observations. Two parameters are used for this correction, namely the radius of maximum winds and the radius of the outermost closed isobar to correct the storm size.

The storm-size correction can be achieved by stretching/compressing the model grid. Let's consider a storm of the wrong size in cylindrical coordinates. Assume the grid size is linearly stretched along the radial direction

$$\alpha_i = \frac{\Delta r_i^*}{\Delta r_i} = a + br_i, \quad (2.4.1.1)$$

where  $a$  and  $b$  are constants.  $r$  and  $r^*$  are the distances from the storm center before and after the model grid is stretched. Index  $i$  represents the  $i^{\text{th}}$  grid point.

Let  $r_m$  and  $R_m$  denote the radius of the maximum wind and radius of the outermost closed isobar (the minimum sea-level pressure is always scaled to the observed value before calculating this radius) for the storm in the background field, respectively. Let  $r_m^*$  and  $R_m^*$  be the observed radius of maximum wind and radius of the outermost closed isobar (which can be redefined if  $a$  in Equation [2.4.1.1] is set to be a constant). If the high-resolution model is able to resolve the hurricane eyewall structure,  $r_m^*/r_m$  will be close to 1; therefore, we can set  $b=0$  in Equation (2.4.1.1) and  $\alpha = r_m^*/r_m$  is a constant. However, if the model doesn't handle the eyewall structure well ( $r_m^*/r_m$  will be smaller than  $R_m^*/R_m$ ) within the background fields, Equation (2.4.1.1) must be used to stretch/compress the model grid.

Integrating Equation (1.4.1.1) results in

$$r^* = f(r) = \int_0^r \alpha(r) dr = \int_0^r (a + br) dr = ar + \frac{1}{2} br^2. \quad (2.4.1.2)$$

The model grids are compressed/stretched such that

$$\text{At } r = r_m, \quad r^* = f(r_m) = r_m^* \quad (2.4.1.3)$$

$$\text{At } r = R_m, \quad r^* = f(R_m) = R_m^*. \quad (2.4.1.4)$$

Substituting (2.4.1.3) and (2.4.1.4) into (2.4.1.2) results in

$$ar_m + \frac{1}{2}br_m^2 = r_m^* \quad (2.4.1.5)$$

$$aR_m + \frac{1}{2}bR_m^2 = R_m^* \quad (2.4.1.6)$$

Solving for a and b,

$$a = \frac{r_m^* R_m^2 - r_m^2 R_m^*}{R_m r_m (R_m - r_m)}, \quad b = 2 \frac{R_m^* r_m - R_m r_m^*}{R_m r_m (R_m - r_m)}. \quad (2.4.1.7)$$

Therefore,

$$r^* = f(r) = \frac{r_m^* R_m^2 - r_m^2 R_m^*}{R_m r_m (R_m - r_m)} r + \frac{R_m^* r_m - R_m r_m^*}{R_m r_m (R_m - r_m)} r^2 \quad (2.4.1.8)$$

One special case is  $\alpha$  being constant, so that

$$\alpha = \alpha_m = \frac{r_m^*}{r_m} = \frac{R_m^*}{R_m} \quad (2.4.1.9)$$

where  $b=0$  in equation (2.4.1.1), and the storm-size correction is based on one parameter only

To calculate the radius of the outermost closed isobar, it is necessary to scale the minimum surface pressure to the observed value as discussed below. A detailed discussion is given in the following. Two functions,  $f_1$  and  $f_2$ , are defined such that, for the 6-h HWRF or HDAS vortex (vortex #1),

$$f_1 = \frac{\Delta p_1}{\Delta p_{1c}} \Delta p_{obs} \quad (2.4.1.10)$$

and for the composite storm (vortex #2),

$$f_2 = \frac{\Delta p_2}{\Delta p_{2c}} \Delta p_{obs} \quad (2.4.1.11)$$

where  $\Delta p_1$  and  $\Delta p_2$  are the 2-D surface perturbation pressures for vortices #1 and #2, respectively.  $\Delta p_{1c}$  and  $\Delta p_{2c}$  are the minimum values of  $\Delta p_1$  and  $\Delta p_2$ , while  $\Delta p_{obs}$  is the observed minimum perturbation pressure.

The radius of the outermost closed isobar for vortices #1 and #2 can be defined as the radius of the 1 hPa contour from  $f_1$  and  $f_2$ , respectively.

It can be shown that after the storm-size correction is applied for vortices #1 and #2, the radius of the outermost closed isobar is unchanged for any combination of the vortices #1 and #2. For example,

$$\Delta p_1 + c\Delta p_2 = \frac{\Delta p_1}{\Delta p_{1c}} \Delta p_{1c} + c \frac{\Delta p_2}{\Delta p_{2c}} \Delta p_{2c}$$

where  $c$  is a constant. At the radius of the 1-hPa contour,  $f_1=1$  and  $f_2=1$ , or

$$\frac{\Delta p_1}{\Delta p_{1c}} = \frac{\Delta p_2}{\Delta p_{2c}} = \frac{1}{\Delta p_{obs}}$$

Thus,

$$\Delta p_1 + c\Delta p_2 = \frac{\Delta p_1}{\Delta p_{1c}} \Delta p_{1c} + c \frac{\Delta p_2}{\Delta p_{2c}} \Delta p_{2c} = \frac{1}{\Delta p_{obs}} (\Delta p_{1c} + c\Delta p_{2c}) = 1$$

where

$$(\Delta p_{1c} + c\Delta p_{2c}) = \Delta p_{obs}. \quad (2.4.1.12)$$

Similarly, to calculate the radius of 34-kt winds, the maximum wind speed for vortices #1 and #2 must be scaled. Two functions,  $g_1$  and  $g_2$ , are defined such that for the 6-h HWRF or GDAS vortex (vortex #1),

$$g_1 = \frac{v_1}{v_{1m}} (v_{obs} - \bar{v}_m) \quad (2.4.1.13)$$

for the composite storm (vortex #2),

$$g_2 = \frac{v_2}{v_{2m}} (v_{obs} - \bar{v}_m) \quad (2.4.1.14)$$

where  $v_{1m}$  and  $v_{2m}$  are the maximum wind speeds for vortices #1 and #2, respectively, and  $(v_{obs} - \bar{v}_m)$  is the observed maximum wind speed minus the environment wind. The environment wind is defined as

$$\bar{v}_m = \max(0, U_{1m} - v_{1m}) \quad (2.4.1.15)$$

where  $U_{1m}$  is the maximum wind speed at the 6-h forecast.

The radii of 34-kt wind for vortices #1 and #2 are calculated by setting both  $g_1$  and  $g_2$  to be 34 kt.

After the storm-size correction, the combination of vortices #1 and #2 can be written as

$$v_1 + \beta v_2 = \frac{v_1}{v_{1m}} v_{1m} + \beta \frac{v_2}{v_{2m}} v_{2m} .$$

At the 34-kt radius (i.e., for  $g_1=34$ ,  $g_2=34$ )

$$v_1 + \beta v_2 = \frac{v_1}{v_{1m}} v_{1m} + \beta \frac{v_2}{v_{2m}} v_{2m} = \frac{34}{v_{obs} - \bar{v}_m} (v_{1m} + \beta v_{2m}) = 34 .$$

Note, the following relationship is used in this

$$(v_{1m} + \beta v_{2m}) + \bar{v}_m = v_{obs} . \quad (2.4.1.16)$$

The radius of maximum winds and the radius of the outermost closed isobar or radius of the average 34-kt wind is used for storm-size correction. Storm-size correction can be problematic because the eyewall size produced in the model can be larger than the observed eyewall, and the model does not support observed small-sized eyewalls. For example, the radius of maximum winds for 2005's Hurricane Wilma was 9 km at 140 kt for several cycles. The model-produced radius of maximum wind was larger than 20 km. If the radius of maximum winds is compressed to 9 km, the eyewall will collapse and significant spin-down will occur. Thus, the minimum value for the storm eyewall size is currently set to 19 km. The eyewall size in the model is related to model resolution, model dynamics, and model physics.

In the storm-size correction procedure, the observed radius of maximum winds is not matched. Instead,  $r_m^*$  is replaced by the average maximum radius between the model value and the observation. The correction is also limited to be 15% of the model value. The limits are set as follows: 10% if  $r_m^*$  is less than 20 km; 10-15% if  $r_m^*$  is between 20 and 40km; and 15% if  $r_m^*$  is greater than 40 km. For the radius of the outermost closed isobar (or average 34-kt wind if storm intensity is higher than 64 kt), the correction limit is set to 15% of the model value.

Even with the current settings, major spin-down may occur if the eyewall size is small and lasts for many cycles, due to the consecutive reduction of the storm eyewall size in the initialization. To fix this problem, size reduction is stopped if the model storm size (measured by the average radius of the filter domain) is smaller than the radius of the outermost closed isobar.

### 2.4.1.1 Surface-pressure adjustment after the storm size correction

In HWRF, only the surface pressure of the axi-symmetric part of the storm is corrected. The governing equation for the axi-symmetric components along the radial direction is

$$(2.4.1.1.1)$$

where  $u$ ,  $v$  and  $w$  are the radial, tangential, and vertical velocity components, respectively.

$F_r$  is friction, where  $F_r \approx -C_d \frac{u}{H_B} v$  and  $H_B$  is the top of the boundary layer.  $F_r$  can be

estimated as  $F_r \approx -10^{-6} v$  away from the storm center, and  $F_r \approx -10^{-5} v$  near the storm center. Dropping the small terms, Equation (2.4.1.1.1) is close to the gradient wind balance.

Because the hurricane component is separated from its environment in this representation, the contribution from the environmental flow to the average tangential wind speed can be dismissed. From now on, the tangential velocity refers to the vortex component.

The gradient wind-stream function  $\psi$  is defined as

$$\frac{\partial \psi}{\partial r} = \frac{v^2}{rf_0} + v \quad (2.4.1.1.2)$$

and

$$\psi = \int_{\infty}^r \left( \frac{v^2}{rf_0} + v \right) dr. \quad (2.4.1.1.3)$$

Due to the coordinate change, Equation (2.4.1.1.2) can be rewritten as

$$\frac{\partial \psi}{\partial r} = \frac{\partial \psi}{\partial r^*} \frac{\partial r^*}{\partial r} = \alpha \frac{\partial \psi}{\partial r^*}$$

$$\frac{v^2}{rf_0} + v = \frac{v^2}{r^*} \frac{r^*}{rf_0} + v = \frac{v^2}{r^*} \frac{f(r)}{rf_0} + v \quad (r = r(r^*)).$$

Therefore, the gradient wind stream function becomes (due to the coordinate transformation)

$$\psi = \int_{\infty}^{r^*} \frac{1}{\alpha(r^*)} \left[ \frac{v^2}{r^*} \frac{f(r^*)}{r(r^*)f_0} + v(r^*) \right] dr^* \quad (2.4.1.1.4)$$

A new gradient wind stream function can also be defined for the new vortex as

$$\frac{\partial \psi^*}{\partial r^*} = \frac{v^2}{r^* f_0} + v, \quad (2.4.1.1.5)$$

where  $v$  is a function of  $r^*$ . Therefore,

$$\psi^* = \int_0^{r^*} \left( \frac{v^2}{r^* f_0} + v \right) dr^*. \quad (2.4.1.1.6)$$

Assuming the hurricane sea-level pressure component is proportional to the gradient wind-stream function at the top of the boundary layer (roughly 850-hPa level), i.e.,

$$\Delta p(r^*) = c(r^*) \psi(r^*) \quad (2.4.1.1.7)$$

and

$$\Delta p^*(r^*) = c(r^*) \psi^*(r^*), \quad (2.4.1.1.8)$$

where  $c(r^*)$  is a function of  $r^*$  and represents the impact of friction on the gradient wind balance. If friction is neglected,  $c(r^*) = 1.0$ , it's the gradient wind balance.

From equations (2.4.1.1.7) and (2.4.1.1.8),

$$\Delta p^* = \Delta p \frac{\psi^*}{\psi}, \quad (2.4.1.1.9)$$

where  $\Delta p = p_s - p_e$  and  $\Delta p^* = p_s^* - p_e$  are the hurricane sea-level pressure perturbations before and after the adjustment, and  $p_e$  is the environment sea-level pressure.

Note that the pressure adjustment is minor due to the grid stretching. For example, if in Equation (2.4.1.1)  $\alpha$  is a constant, it can be shown that Equation (2.4.1.1.4) becomes

$$\psi = \int_0^{r^*} \left( \frac{v^2}{r^* f_0} + \frac{1}{\alpha} v \right) dr^*. \quad (2.4.1.1.10)$$

This value is very close to that of Equation (2.4.1.1.6) because the first term dominates.

#### 2.4.1.2 Temperature adjustment

Once the surface pressure is corrected, the temperature field must be corrected.

Next, consider the vertical equation of motion. Neglecting the Coriolis, water load, and viscous terms,

$$\frac{dw}{dt} = -\frac{1}{\rho} \frac{\partial p}{\partial z} - g. \quad (2.4.1.2.1)$$

The first term on the right-hand side is the pressure gradient force, and  $g$  is gravity.  $dw/dt$  is the total derivative (or Lagrangian air-parcel acceleration) which, in the large-scale environment, is relatively small when compared with either of the last two terms.

Therefore,

$$-\frac{1}{\rho} \frac{\partial p}{\partial z} - g = 0$$

or

$$\frac{\partial p}{\partial z} = -\frac{p}{RT_v} g \quad (2.4.1.2.2)$$

Applying equation (2.4.1.2.2) to the environmental field and integrating from surface to model top, the following relationship results:

$$\ln \frac{p_s}{p_T} = \frac{g}{R} \int_0^H \frac{dz}{\bar{T}_v} \quad (2.4.1.2.3)$$

where  $H$  and  $p_T$  are the height and pressure at the model top, respectively, and  $\bar{T}_v$  is the virtual temperature of the environment.

The hydrostatic equation for the total field (environment field + vortex) is

$$\ln \frac{p_s + \Delta p}{p_T} = \frac{g}{R} \int_0^H \frac{dz}{(\bar{T}_v + \Delta T_v)}, \quad (2.4.1.2.4)$$

where  $\Delta p$  and  $\Delta T_v$  are the sea-level pressure and virtual temperature perturbations for the hurricane vortex. Since  $\Delta p \ll p_s$  and  $\Delta T_v \ll \bar{T}_v$ , Equation (2.4.1.2.4) can be linearized as

$$\ln \frac{p_s}{p_T} \left(1 + \frac{\Delta p}{p_s}\right) = \frac{g}{R} \int_0^H \frac{dz}{(\bar{T}_v + \Delta T_v)} \approx \frac{g}{R} \int_0^H \frac{dz}{\bar{T}_v} \left(1 - \frac{\Delta T_v}{\bar{T}_v}\right). \quad (2.4.1.2.5)$$

Subtracting Equation (2.4.1.2.3) from Equation (2.4.1.2.5) leads to

$$\ln\left(1 + \frac{\Delta p}{p_s}\right) \approx -\frac{g}{R} \int_0^H \frac{\Delta T_v}{\bar{T}_v^2} dz,$$

or

$$\frac{\Delta p}{p_s} \approx -\frac{g}{R} \int_0^H \frac{\Delta T_v}{\bar{T}_v^2} dz. \quad (2.4.1.2.6)$$

Multiplying Equation (2.4.1.2.6) by  $\Gamma(r^*) = \psi^* / \psi$  ( $\Gamma$  is a function of  $x$  and  $y$  only) results in

$$\frac{\Gamma \Delta p}{p_s} \approx -\frac{g}{R} \int_0^H \frac{\Gamma \Delta T_v}{\bar{T}_v^2} dz. \quad (2.4.1.2.7)$$

A simple solution to equation (2.4.1.2.7) – assuming the virtual temperature correction is proportional to the magnitude of the virtual temperature perturbation – is then applied, and the new virtual temperature is

$$T_v^* = \bar{T}_v + \Gamma \Delta T_v = T_v + (\Gamma - 1) \Delta T_v. \quad (2.4.1.2.8)$$

In terms of the temperature field,

$$T^* = \bar{T} + \Gamma \Delta T = T + (\Gamma - 1) \Delta T \quad (2.4.1.2.9)$$

where  $T$  is the 3-D temperature before the surface-pressure correction, and  $\Delta T$  is perturbation temperature for vortex #1.

#### 2.4.1.3 Water-vapor adjustment

It is assumed that the relative humidity is unchanged before and after the temperature correction:

$$RH = \frac{e}{e_s(T)} \approx \frac{e^*}{e_s^*(T^*)} \quad (2.4.1.3.1)$$

where  $e$  and  $e_s(T)$  are the vapor pressure and the saturation vapor pressure in the model guess fields, respectively.  $e^*$  and  $e_s^*(T^*)$  are the vapor pressure and the saturation vapor pressure respectively, after the temperature adjustment.

Using the definition of the mixing ratio,

$$q = 0.622 \frac{e}{p - e} \quad (2.4.1.3.2)$$

at the same pressure level and from Equation (2.4.1.3.1),

$$\frac{q^*}{q} \gg \frac{e^*}{e} \gg \frac{e_s^*(T^*)}{e_s(T)}. \quad (2.4.1.3.3)$$

Therefore, the new mixing ratio becomes

$$q^* \approx \frac{e^*}{e} q \approx \frac{e_s^*}{e_s} q \approx q + \left( \frac{e_s^*}{e_s} - 1 \right) q. \quad (2.4.1.3.4)$$

From the saturation water pressure

$$e_s(T) = 6.112 \exp\left[17.67 \frac{(T - 273.16)}{(T - 29.66)}\right] \quad (2.4.1.3.5)$$

it can be shown that

$$\frac{e_s^*}{e_s} = \exp\left[\frac{17.67 * 243.5(T^* - T)}{(T^* - 29.66)(T - 29.66)}\right]. \quad (2.4.1.3.6)$$

Substituting Equation (2.4.1.3.6) into (2.4.1.3.4), the new mixing ratio can be derived after the temperature field is adjusted.

## 2.4.2 Storm intensity correction

Generally speaking, the storm in the background field has a different maximum wind speed compared to the observations. The storm intensity must be corrected based on the observations, which is discussed in detail in the following sections.

### 2.4.2.1 Computation of intensity correction factor $\beta$

Consider the general formulation in the traditional x, y, and z coordinates; where  $u_1^*$  and  $v_1^*$  are the background horizontal velocity, and  $u_2$  and  $v_2$  are the vortex horizontal velocity to be added to the background fields. First, define

$$F_1 = \sqrt{(u_1^* + u_2)^2 + (v_1^* + v_2)^2} \quad (2.4.2.1.1)$$

and

$$F_2 = \sqrt{(u_1^* + \beta u_2)^2 + (v_1^* + \beta v_2)^2}. \quad (2.4.2.1.2)$$

Function  $F_1$  is the wind speed if we simply add a vortex to the environment (or background fields). Function  $F_2$  is the new wind speed after the intensity correction.

We consider two cases here.

Case I:  $F_1$  is larger than the observed maximum wind speed. We set  $u_1^*$  and  $v_1^*$  to be the environment wind component; that is,  $u_1^* = U$  and  $v_1^* = V$  (the vortex is removed and the field is relatively smooth); and  $u_2 = u_1$  and  $v_2 = v_1$  are the vortex horizontal wind components from the previous cycle's 6-h forecast (this is called vortex #1, which contains both the axi-symmetric and asymmetric parts of the vortex).

Case II:  $F_1$  is smaller than the observed maximum wind speed. The vortex is added back into the environment fields after the grid stretching; that is,  $u_1^* = U + u_1$  and  $v_1^* = V + v_1$ .

$u_2$  and  $v_2$  are chosen to be an axi-symmetric composite vortex (vortex #2) which has the same radius of maximum wind as the first vortex.

For both cases, it is acceptable to assume that the maximum wind speeds for  $F_1$  and  $F_2$  are at the same model grid point. To find  $\beta$ , first the model grid point is located where  $F_1$  is at its maximum. The wind components at this model grid point are denoted as  $u_1^m$ ,  $v_1^m$ ,  $u_2^m$ , and  $v_2^m$  (for convenience, we drop the superscript  $m$ ), so that

$$(u_1^* + \beta u_2)^2 + (v_1^* + \beta v_2)^2 = v_{obs}^2 \quad (2.4.2.1.3)$$

where  $v_{obs}$  is the 10-m observed wind converted to the first model level.

Solving for  $\beta$ ,

$$\beta = \frac{-u_1^* u_2 - v_1^* v_2 + \sqrt{v_{obs}^2 (u_2^2 + v_2^2) - (u_1^* v_2 - v_1^* u_2)^2}}{(u_2^2 + v_2^2)}. \quad (2.4.2.1.4)$$

The procedure to correct wind speed is as follows:

First, the maximum wind speed is calculated using Equation (2.4.2.1.1) by adding the vortex into the environment fields. If the maximum of  $F_1$  is greater than the observed wind speed, it is classified as Case I and the value of  $\beta$  is calculated. If the maximum of  $F_1$  is smaller than the observed wind speed, it is classified as Case II so that the asymmetric part of the storm is not amplified. Amplifying it may negatively affect the track forecasts. In Case II, the original vortex is first added to the environment fields after the storm-size correction, and then a small portion of an axi-symmetric composite storm is added. The composite storm portion is calculated from Equation (2.4.2.1.4). Finally, the new vortex 3-D wind field becomes

$$u(x, y, z) = u_1^*(x, y, z) + \beta u_2(x, y, z)$$

$$v(x, y, z) = v_1^*(x, y, z) + \beta v_2(x, y, z).$$

#### 2.4.2.2 Surface pressure, temperature, and moisture adjustments after the intensity correction

If the background fields are produced by high-resolution models (such as in HWRF), the intensity corrections are minor and the correction of the storm structure is not necessary. The guess fields should be close to the observations; therefore,

In Case I       $\beta$  is close to 1;

In Case II      $\beta$  is close to 0.

After the wind-speed correction, the sea-level pressure, 3-D temperature, and the water vapor fields must be adjusted. These adjustments are described below.

In Case I,  $\beta$  is close to 1. Following the discussion in Section 2.4.1.1, the gradient wind-stream function  $\psi$  is defined as

$$\frac{\partial \psi}{\partial r} = \frac{v_2}{rf_0} + v_2 \quad (2.4.2.2.1)$$

and

$$\psi_2 = \int_{\infty}^r \left( \frac{v_2^2}{rf_0} + v_2 \right) dr . \quad (2.4.2.2.2)$$

The new gradient wind-stream function is

$$\psi^{new} = \int_{\infty}^r \left[ \frac{(\beta v_2)^2}{rf_0} + \beta v_2 \right] dr . \quad (2.4.2.2.3)$$

The new sea-level pressure perturbation is

$$\Delta p^{new} = \Delta p \frac{\psi^{new}}{\psi_2} \quad (2.4.2.2.4)$$

where  $\Delta p = p_s - p_e$  and  $\Delta p^{new} = p_s^{new} - p_e$  are the hurricane sea-level pressure perturbations before and after the adjustment and  $p_e$  is the environment sea-level pressure.

In Case II,  $\beta$  is close to 0.  $\psi_1$  is defined as:

$$\psi_1 = \int_{\infty}^r \left( \frac{v_1^2}{rf_0} + v_1 \right) dr , \quad (2.4.2.2.5)$$

and the new gradient wind-stream function is

$$\psi^{new} = \int_{\infty}^r \left[ \frac{(v_1 + \beta v_2)^2}{rf_0} + (v_1 + \beta v_2) \right] dr . \quad (2.4.2.2.6)$$

The new sea-level pressure perturbation is calculated as

$$\Delta p^{new} = \Delta p \frac{\psi^{new}}{\psi_1} . \quad (2.4.2.2.7)$$

Equations (2.4.2.2.4) and (2.4.2.2.7) should be close to the observed surface pressure. However, if the model has an incorrect surface pressure-wind relationship, Equations (2.4.2.2.4) and (2.4.2.2.7) may have a large surface-pressure difference from the observation. The pressure-wind relationship was improved in the 2013 HWRF, where the limit is set to be 10% of the observation  $\Delta p_{obs}$  without producing large spin up/spin down problems.

The correction of the temperature field is as follows:

In Case I,

$$\Gamma = \frac{\psi^{new}}{\psi_2}. \quad (2.4.2.2.8)$$

Then the following equation is used to correct the temperature fields.

$$T^* = T_e + \Gamma \Delta T_1 = T + (\Gamma - 1) \Delta T_1 \quad (2.4.2.2.9)$$

In Case II,

$$\Gamma = \frac{\psi^{new}}{\psi_1} \quad (2.4.2.2.10)$$

is defined and

$$T^* = T_e + \Delta T_1 + (\Gamma - 1) \Delta T_2 = T + (\Gamma - 1) \Delta T_2, \quad (2.4.2.2.11)$$

where  $T$  is the 3-D background temperature field (environment+vortex1), and  $\Delta T_2$  is the temperature perturbation of the axi-symmetric composite vortex.

The corrections of water vapor in both cases are the same as those discussed in Section 2.4.1.3.

The storm-intensity correction is, in fact, a data analysis. The observation data used here is the surface maximum wind speed (single point data), and the background error correlations are flow dependent and based on the storm structure. The storm structure used for the background error correlation is vortex #1 in Case I, and vortex #2 in Case II (except for water vapor which still uses the vortex #1 structure). Vortex #2 is an axi-symmetric vortex. If the storm structure in vortex #1 could be trusted, one could choose vortex #2 as the axi-symmetric part of vortex #1. In HWRF, the structure of vortex #1 is not completely trusted when the background storm is weak; therefore, an axi-symmetric composite vortex from old model forecasts is employed as vortex #2.

## 2.5 Data assimilation with GSI in HWRF

The HDAS has been upgraded and now includes three different methods for hybrid ensemble-variational data assimilation: one-way hybrid with the GFS EnKF ensemble, one-way hybrid with the HWRF ensemble, and two-way hybrid (i.e., self-cycled) with

the HWRF ensemble. The GSI-based, one-way hybrid data assimilation (DA) using the GFS ensemble has been used in the operational HWRF since 2013. During 2015, the capability to use a 40-member high-resolution HWRF ensemble was added. The advantage that this upgrade provided was the use of HWRF flow-dependent background-error covariances rather than covariances estimated from the GFS ensemble. The first cycle of the HWRF ensemble is always initialized from the GFS ensemble analysis. Subsequent HWRF ensemble cycles can either be initialized from the GFS analysis ensemble in a one-way hybrid procedure, or the HWRF ensemble can be self-cycled and initialized from six-hour forecasts from the previous ensemble cycle. The self-cycled option was added to the HWRF system in 2017. In general, the HWRF ensemble hybrid DA option is activated for high-priority storms – namely, those storms with planned TDR missions. Due to the complexity and the computational resources required, the HWRF ensemble hybrid DA options are not supported in the HWRF v4.0a public release. However, the hybrid assimilation of TDR data using HWRF v4.0a can be performed using the GFS ensemble. A brief introduction to the unsupported HWRF ensemble hybrid DA options are provided in Section 2.5.4.

### 2.5.1 GSI hybrid data assimilation scheme

The background-error covariance of the hybrid scheme is a combination of the static background-error covariance obtained through the National Meteorological Center (now NCEP) method and the flow-dependent background-error covariance estimated from the short-term ensemble forecast. The hybrid method provides better analysis when compared with stand-alone ensemble-based methods (e.g., Ensemble Kalman filter, EnKF), especially when the ensemble size is small, or large model error is present (Wang et al. 2007b).

In the GSI, the ensemble covariance is incorporated into the variational scheme through the extended control variable method (Lorenz 2003 and Buehner 2005). The following description of the algorithm is based on Wang (2010).

The analysis increment, denoted as  $\mathbf{x}'$ , is a sum of two terms:

$$\mathbf{x} = \mathbf{x}'_1 + \sum_{k=1}^K (\alpha_k \circ \mathbf{x}_k^e), \quad (2.5.1)$$

where  $\mathbf{x}'_1$  is the increment associated with the GSI static background covariance, and the second term is the  $k^{\text{th}}$  increment associated with the flow-dependent ensemble covariance. In the second term  $\mathbf{x}_k^e$  is the  $k^{\text{th}}$  ensemble perturbation normalized by  $(K - 1)^{1/2}$ , where  $K$  is the ensemble size. The vector  $\alpha_k, k = 1, \dots, K$ , contains the extended control variables for each ensemble member. The second term represents a local linear combination of ensemble perturbations, and  $\alpha_k$  is the weight applied to the  $k^{\text{th}}$  ensemble perturbation.

The cost function minimized to obtain  $\mathbf{x}'$  is

$$J(\mathbf{x}'_1, a) = b_1(\mathbf{x}'_1)^T B_1^{-1}(\mathbf{x}'_1) + b_2(a)^T A^{-1}(a) + (\mathbf{y}^0 - H\mathbf{x}')^T R^{-1}(\mathbf{y}^0 - H\mathbf{x}') + J_c, \quad (2.5.2)$$

where

- $\mathbf{B}_1$  is the static background-error covariance matrix;
- $\beta_1$  is the weight applied to the static background-error covariance;
- $\mathbf{A}$  defines the spatial correlation of  $\boldsymbol{\alpha}$ ;
- $\beta_2$  is the weight applied to the ensemble covariance;
- $\mathbf{y}$  is the innovation vector;
- $\mathbf{R}$  is the observational and representativeness error covariance matrix;
- $\mathbf{H}$  is the observation operator; and
- $J_c$  is the constraint term.

Wang et al. (2010) illustrated the equivalence of using Eqs. (2.5.1) - (2.5.2) to compute the updated analysis as compared to the scheme that replaces the background-error covariance in Eq. (2.5.2) with the weighted sum of the static background-error covariance and the ensemble covariance modulated by the correlation matrix in  $\mathbf{A}$ . The paper shows that matrix  $\mathbf{A}$  determines the covariance localization on the ensemble covariance.

The same conjugate gradient-minimization algorithm used for the 3DVAR scheme is used to find the optimal solution for the analysis problem (2.5.1) and (2.5.2), except the control variable and the background covariance are extended as

$$\mathbf{x} = \begin{pmatrix} \mathbf{x}'_1 \\ \boldsymbol{\alpha} \end{pmatrix}, \quad (2.5.3)$$

and

$$\mathbf{B} = \begin{pmatrix} \frac{1}{\beta_1} \mathbf{B}_1 & \mathbf{0} \\ \mathbf{0} & \frac{1}{\beta_2} \mathbf{A} \end{pmatrix}.$$

$$B = \begin{pmatrix} \frac{1}{b_1} B_1 & 0 \\ 0 & \frac{1}{b_2} A \end{pmatrix} \quad (2.5.4)$$

More information about the hybrid algorithm can be found in Wang (2010).

### 2.5.2 HWRF data assimilation configurations

Many experiments have demonstrated that a regional analysis at the same resolution shows little or no benefit over the global analysis for the large-scale TC environment. Therefore, the GFS analysis is directly interpolated to the HWRF outer domain. This helps to facilitate computational resources for data assimilation at the TC vortex scales. Data assimilation is performed on HWRF domains of dimension  $28^\circ \times 28^\circ$  (with grid spacing of  $0.045^\circ$ ) and  $15^\circ \times 15^\circ$  (with grid spacing of  $0.015^\circ$ ; see Fig. 2.2). The data-assimilation domains are referred to as *ghost* domains. The ghost domain for d02 can

cover the entire storm and the near-storm environment, while the ghost domain for d03 is specifically used to assimilate aircraft reconnaissance observations. The analyses of the two DA domains are then interpolated to the forecast intermediate and inner nests, and merged to the outer domain in the vortex and its near-environment area.

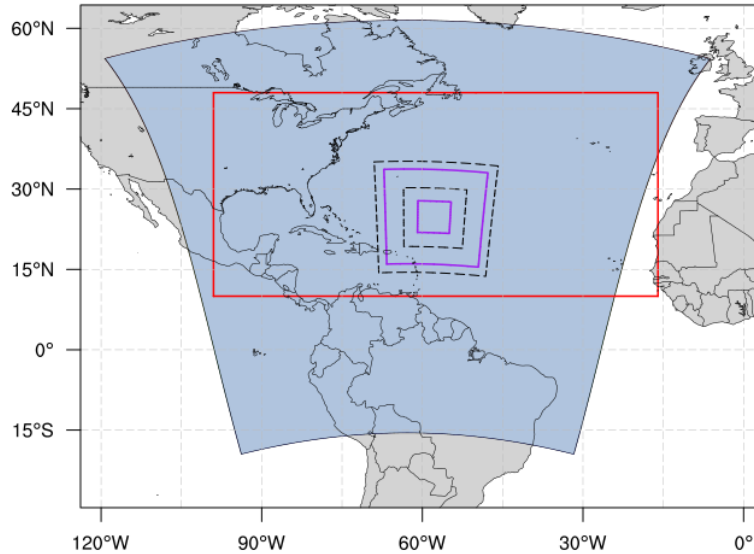


Figure 2-2: HWRF data assimilation and model forecast domains. The blue region is the outer 13.5-km domain. The purple solid boxes show the sizes of the vortex-following 4.5-km and 1.5-km domains, while the black dashed lines are the ghost domains for d02 and d03. The red box is the unified Atlantic MIPOM-TC domain.

Vortex initialization is performed before data assimilation. The HWRF vortex initialization code now supports the option to conduct only vortex relocation, without size and intensity correction. While this capability is not used operationally, it is often employed in research as the implications of performing vortex initialization along with data assimilation (specifically, the assimilation of inner-core observations) has been shown to degrade forecast skill in some cases.

The first-guess forecast for the HWRF hybrid data-assimilation at each analysis time is the global GDAS 6-h forecast. The GDAS 3- and 9-h forecasts bound the observation time window (i.e.,  $\pm 3$  hours from the analysis time). The GDAS forecasts have a spectral-truncation of T1534 and contain 64 vertical levels. For the 3-, 6-, and 9-h forecasts, the TC vortex is relocated and corrected for both size and intensity (see section 2.4). This procedure is referred to as the First-Guess at Appropriate Time (FGAT). It is used to allow data within the 6-h time window to be better assimilated. In traditional 3DVAR data assimilation schemes, observations are assumed to be valid only at the analysis time. With FGAT, observations are compared with the first guess at the observation time to obtain the innovation. The FGAT is obtained by interpolating the two closest background fields in time within GSI. Therefore, multiple first guess times (here, 3-, 6-, and 9-h forecasts) are required. The system can also be configured to use FGAT with hourly first guesses (FGATINV = 1 in hwrf.conf), so that the first guess at observation time can be more accurately represented.

As shown in Equation 2.5.2, the role of matrix  $\mathbf{A}$  is to apply covariance localization to the ensemble covariances. In GSI, a recursive filter is used to approximate the static background-error covariance  $\mathbf{B}_1$ , as well as  $\mathbf{A}$ . The correlation length scale of the recursive filter used to approximate  $\mathbf{A}$  prescribes the covariance localization length scale for the ensemble covariances. The parameters in the GSI namelist that define the horizontal and vertical localization length scales refer to the recursive filter e-folding length scale. In most EnKF applications, the correlation function given by Eq. (4.10) of Gaspari and Cohn (1999) is used for covariance localization. The Gaspari-Cohn type of localization length scale refers to the distance at which the covariance is forced to be zero, which is roughly equivalent to the e-folding length scale divided by 0.388. For the ghost d02 and d03 ghost domain analyses, the horizontal localization length scale is set to 300/150 km ( $s\_ens\_h=300/150$ ). The vertical localization length scales for both analysis domains are set to be 0.5 in units of  $\ln p$  ( $s\_ens\_v=-0.5$ ), where  $p$  is the pressure in units of centibar (cb). Note that if the vertical localization length scale is measured in units of  $\ln p$ ,  $s\_ens\_v$  is expressed as a negative value and the length scale is the absolute value of  $s\_ens\_v$ . For both the d02 and d03 ghost domains,  $\beta_1^{-1}$  beta1\_inv in the GSI namelist) is set to 0.2, which means that 80% of the weight is placed on the ensemble covariance.

When using GSI with HWRF, “wrf\_nmm\_regional” and “uv\_hyb\_ens” in the GSI namelist should be set to “true.” The use of “uv\_hyb\_ens=.true.” means that ensemble perturbations contain the zonal and meridional components of the wind instead of stream function and velocity potential.

The GSI analysis is obtained through iterative minimization of the cost function (Eq. [2.5.2]). The iteration algorithm can be found in the [GSI Advanced User’s Guide](#) Chapter 4, Section 4.2. Two outer loops with 50 iterations each are used for HWRF (miter=2, niter[1]=50, niter[2]=50). The outer loop consists of more complete (nonlinear) observation operators and quality control. Usually, simpler observation operators are used in the inner loop.

The GSI analysis variables, computed from the HWRF variables, are streamfunction, unbalanced part of velocity potential, unbalanced part of temperature, unbalanced part of surface pressure, pseudo-relative humidity (qoption = 1) or normalized relative humidity (qoption = 2), surface-skin temperature (sea-surface temperature, plus skin temperature over land and ice), and the extended control variable  $\alpha$ . HWRF uses the normalized relative humidity as it allows for a multivariate coupling of the moisture, temperature, and pressure increments, as well as flow dependence (Kleist et al. 2009). An accurate specification of the surface-skin temperature is extremely important for the estimation of the simulated brightness temperature (Derber and Wu 1998). Therefore, it is included as an analysis variable, but is not introduced into the forecast model (Derber and Wu 1998). Currently, the ozone and cloud variables are not analyzed. Finally, because satellite bias correction coefficients are obtained from GDAS and directly used for the data assimilation into HWRF, the bias correction coefficients are not updated (e.g., cycled) (upd\_pred=0).

Variational quality control (VarQC [Andersson and Järvinen 1999]), which operates during the iterative minimization, is used for most of the conventional observations (niter\_no\_qc[1]=20, niter\_no\_qc[2]=0, noiqc=.true., njqc=.false., vqc=.true.,). In VarQC,

the observation cost function is modified to account for the non-Gaussian nature of the gross error. The modified cost function reduces the impact (e.g., the analysis weights) given to observations with large departures from the current-state vector. Unlike Optimum Interpolation quality control (OIQC, Lorenc 1981) where data are immediately rejected due to large differences relative to the first-guess forecast, observations may be better assimilated during later iterations if the difference between the updated first-guess and the observations decreases. The incorporation of quality control adds non-linearity to the variational problem while non-Gaussian observation error statistics lead to a non-quadratic cost function. This problem is partly mitigated by partially minimizing the cost function without quality control. For HWRF analysis, VarQC is switched on after the first 20 inner loop minimizations (`niter_no_qc[1]=20`).

### 2.5.3 Observations

Several observations are assimilated into the HWRF analysis:

- conventional observations (contained in `prepbufr` file) with some satellite AMVs;
- NOAA P3 aircraft Tail Doppler Radar;
- satellite radiance observations including data from CrIS, SSMIS, Metop-B AMSU-A, Metop-B MHS and IASI; and
- HS3 Global Hawk dropsonde and TCVital mean sea-level pressure (MSLP) data;
- High-resolution flight-level data;
- Hourly shortwave, clear air-water vapor, and visible Atmospheric Motion Vectors (AMVs) from GOES.

New data added for the 2018 implementation include GOES-16, NOAA-20, SFMR, Dropsonde drifts and TDR from G-IV.

New data added for the 2017 implementation include high-resolution flight-level data as well as hourly shortwave, clear air-water vapor, and visible Atmospheric Motion Vectors (AMVs) from GOES. The inner-core wind observations from Global Hawk dropsondes are excluded from assimilation similar to the way wind data are used for other dropsondes.

Conventional observations assimilated include:

- Radiosondes;
- dropwindsondes;
- aircraft reports (AIREP/PIREP, RECCO, MDCRS-ACARS, TAMDAR, AMDAR);
- surface ship and buoy observations;
- surface observations over land;
- pibal winds;

- wind profilers;
- radar-derived Velocity Azimuth Display (VAD) wind;
- WindSat scatterometer winds; and
- integrated precipitable water derived from the Global Positioning System.

Satellite observations assimilated include:

- Radiances from IR instruments: HIRS, AIRS, IASI, GOES Sounders, CrIS, SSMIS;
- Radiances from MW instruments: AMSU-A, MHS, ATMS; and
- Satellite derived wind: IR/VIS cloud drift winds and water vapor winds from GOES, EUMETSAT, MODIS, JMA.

Dropwindsonde observations are obtained from the U.S. Air Force WC-130J, NOAA P3, G-IV, and the Global Hawk aircrafts. The default configuration of the current HWRF system now assimilates inner-core dropsonde (e.g., TEMP-DROP) observations collected from the aforementioned aircraft by accounting for the wind-induced drift of the dropsonde as it falls from the aircraft to the ocean surface. This is accomplished during the bufrprep step, which processes available inner-core dropsonde observations and appends them to the existing prepbufr file (with drift information added). The previous behavior (prior to HWRF v4.0a) of rejecting dropsonde wind reports within a radius of 111 km (or three times the estimated RMW -- whichever is larger) and surface-pressure (e.g., synthetic or bogus observations) reports near the storm center can be retained by setting prepbufrprep=3 in parm/hwrf.conf. This flags inner-core wind and surface-pressure reports in the prepbufr (i.e., a large quality control [QC] mark is assigned to them). This QC mark causes the data to be rejected, and, therefore, not used in the GSI analysis. All other dropsonde reports, including temperature and moisture profiles near the storm center, will still be assimilated. This strategy was originally adopted because experiments revealed that assimilating inner-core wind and surface-pressure reports negatively impacted the forecasts. However, with the inclusion of the dropsonde drift information, this is no longer the case.

High-density flight-level wind, temperature, and moisture measurements are assimilated into HWRF collected by the aircraft listed above. More information about the high-density flight-level data can be found on the NHC website (<http://www.nhc.noaa.gov/recon.php>).

The NOAA P3 and G-IV TDR, using the Fore-Aft Scanning Technique (FAST), probes the 3-D wind field within the inner core of the TC (Gamache et al. 1995). The antenna is programmed to scan as much as 25° fore or aft of the plane perpendicular to the fuselage. Significant quality-control reviews of the radial velocity data are conducted aboard the P3 aircraft before the data are sent to the ground, including: (1) removing the projection of the aircraft motion on the observed Doppler velocity; (2) removing the reflection of the main lobe and side lobes off the sea surface; (3) removing noise; and (4) unfolding. The TDR data in Binary Universal Form for the Representation of meteorological data (BUFR) format contain quality-controlled radial velocities averaged over 8 gates along

the radial direction. Further data thinning to the model grid spacing and quality control of the TDR radial velocities are performed before the data are assimilated. Figure 2-3 is an example of the TDR radial velocity data assimilated for Hurricane Earl at 12Z on August 29, 2010. The observation error, including the representativeness error, of the radial velocity dataset is set to be  $5 \text{ m s}^{-1}$ . When the difference between the observation and the background field is more than  $10 \text{ m s}^{-1}$ , the observation error gradually increases to  $10 \text{ m s}^{-1}$ . Observations differing from the background by more than  $20 \text{ m s}^{-1}$  are rejected. The benefit of assimilating TDR data into HWRF was discovered in a realtime demo experiment performed during the 2012 hurricane season (Gall et al. 2013).

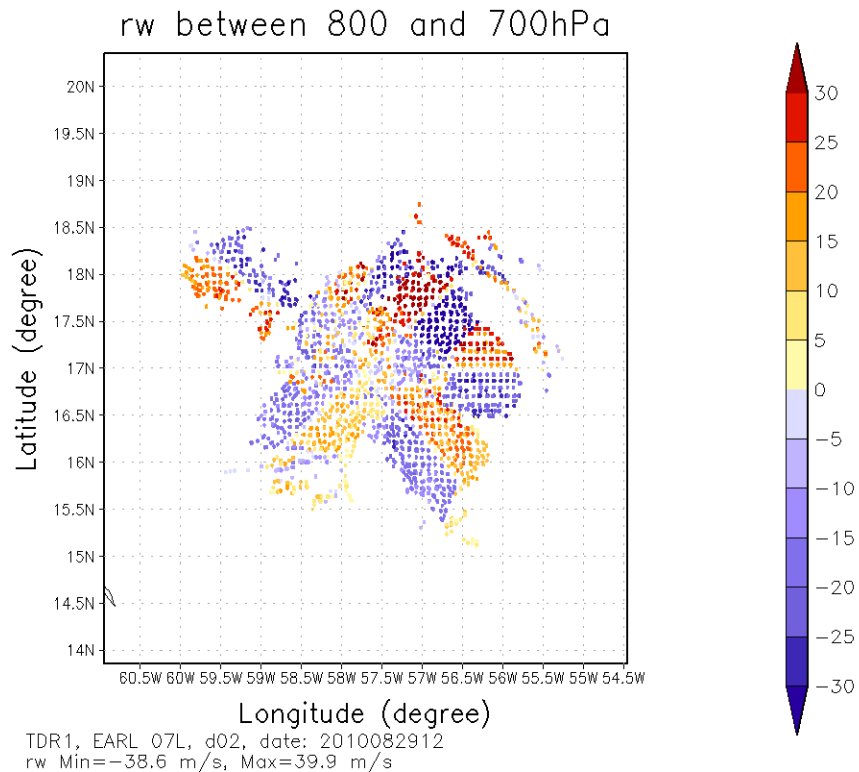


Figure 2-3: NOAA TDR radial velocities between 800 hPa and 700 hPa assimilated at 12 Z on August 29, 2010.

HWRF has assimilated TC Vital mean sea-level pressure (MSLP) data since the 2015 implementation. The MSLP dataset is useful when high-resolution aircraft reconnaissance observations are not available. When high-resolution aircraft reconnaissance observations are available, the impact of the MSLP data is very limited.

To assimilate satellite radiance observations properly, biases between the observed radiances and those simulated from the model first guess must be corrected. The biases can originate from systematic errors in the data (e.g., due to poor calibration), inadequacies in the observation operator (e.g., interpolation or radiative transfer errors), or biases in the forecast model (Derber and Wu 1998; McNally 2000; Harris and Kelly 2001). In GSI, the coefficients of the chosen bias predictors are treated as additional control variables estimated simultaneously with the rest of the analysis variables (Derber and Wu 1998; McNally 2000). Because HWRF is only run when TCs are present, the

short cycling period and variable sample size due to movable forecast domains make the spin up of bias correction problematic. An alternative is to use bias-correction coefficients estimated from GDAS. However, direct utilization of global bias-correction coefficients in a regional analysis may not be appropriate because the vertical coordinates and the radiance data assimilated (which directly affect the result of bias correction) differ between the global and the regional model.

A solution that allows for using global bias-correction coefficients in the regional analysis is to use a global-regional blended vertical coordinate in the GSI analysis. The GFS and HWRf model levels are blended together in the stratosphere, smoothly transitioning from the HWRf coordinate to the GFS coordinate. With the blended coordinate, the vertical resolution in the stratosphere is increased and the model top is further extended to 0.26 hPa with vertical levels increased to 85 levels. The GDAS forecast valid at the same time is added as additional levels in the first guess. It was found that using a blended vertical coordinate significantly improved the data usage and model fit to observation for both microwave (MW) and infrared (IR) instruments.

HWRf does not provide ozone profiles, which are used in the radiative transfer calculation to obtain simulated brightness temperature. The lack of ozone profiles can lead to a biased analysis, especially for IR instruments. To address this deficiency, the ozone profiles from GFS are used in the HWRf analysis. Using GFS ozone profiles improved the data coverage and model fit to observations across the entire IR spectrum significantly.

Using the global-regional blended vertical coordinate for the analysis, together with using the GFS ozone profile, improved the assimilation of satellite radiance data in HWRf. When using the global-regional blended vertical coordinate for radiance assimilation, the model top of the analysis grid is raised to be the same as the global model.

The bias correction scheme used in GDAS has recently been upgraded (Zhu et. al. 2014). Therefore, the bias correction coefficients estimated from the enhanced scheme have been used in the GSI analysis since 2015.

#### **2.5.4 Self-cycled HWRf ensemble hybrid DA system**

In 2017, the operational data assimilation system underwent a major upgrade with the addition of the self-cycled HWRf ensemble hybrid DA system. The system was developed through collaboration between the University of Oklahoma and the NOAA Earth System Research Laboratory (ESRL). To run this new system, the “run\_ensemble\_da” in *hwr\_f\_basic.conf* needs to be set to “yes” and “ensda\_opt” needs to be set to 1. “ensda\_opt=0” is the one-way HWRf ensemble hybrid DA option. Running and utilizing the HWRf ensemble in hybrid data assimilation is not supported in the HWRf 4.0a public release. Please refer to the User’s Guide on how to use other GSI options within the HWRf system.

HWRf is run in 6-h analysis cycles. The first HWRf ensemble forecast is initialized from a previous 6-h GDAS EnKF analysis, the same approach used with the previously operational one-way HWRf ensemble utilized in 2015 and 2016. The domains used to run the ensemble forecast are the outer domain, which is the same as the outer domain of

the control forecast, and a  $30^{\circ} \times 30^{\circ}$  nest with grid spacing of  $0.033^{\circ}$ . Both the outer domain and the nest domain are fixed during the forecast and are recentered to the TC center at each analysis time. Therefore, the previous cycle's HWRF ensemble forecast domain center is different from the GSI analysis domain center. The ensemble forecast nest is large enough to cover the GSI analysis domain for d03, but may not be able to cover the GSI analysis domain for d02. The 6-h ensemble forecast for d02 on the nest with  $0.033^{\circ}$  grid spacing is used to provide flow-dependent background covariance for the GSI analysis d03 domain. The GFS ensemble at T574L64 is currently used in the GSI hybrid analysis for d02. Alternatively, the HWRF ensemble can be used instead of the GFS on the outer domain during the GSI d02 analysis.

The issues that led to using the global-regional blended coordinate previously discussed above are aggravated when the regional HWRF ensemble is used to calculate the ensemble covariance in a GSI hybrid analysis. This is because the ensemble perturbations are not available in the extended vertical levels above the model top of the regional ensemble. One solution is to use the static background-error covariance above the blending zone. In addition, the same blending factors used to blend the global and regional first guesses in the blending zone are applied to the weights assigned to the static covariance and the ensemble covariance. This capability is available with the GSI public release but is not supported for HWRF.

The workflow of the self-cycled hybrid DA system is shown in Fig. 2.4. This is a two-way coupled system. The HWRF ensemble forecast is used in the GSI hybrid analysis to provide the background covariance. Each HWRF d02 and d03 ensemble member is updated using the EnKF. The ensemble mean of the HWRF first-guess is used to select a uniform set of observations to be assimilated by each ensemble member during the EnKF analysis. After the EnKF analysis, ensemble members are recentered around the GSI hybrid analysis by replacing the ensemble mean with the higher resolution GSI analysis. For the subsequent ensemble forecast cycles, the HWRF d02 and d03 ensemble members are initialized from GFS EnKF analysis. Finally, the vortex defined by the HWRF EnKF analysis is interpolated and merged to the GFS EnKF analysis within HWRF d01.

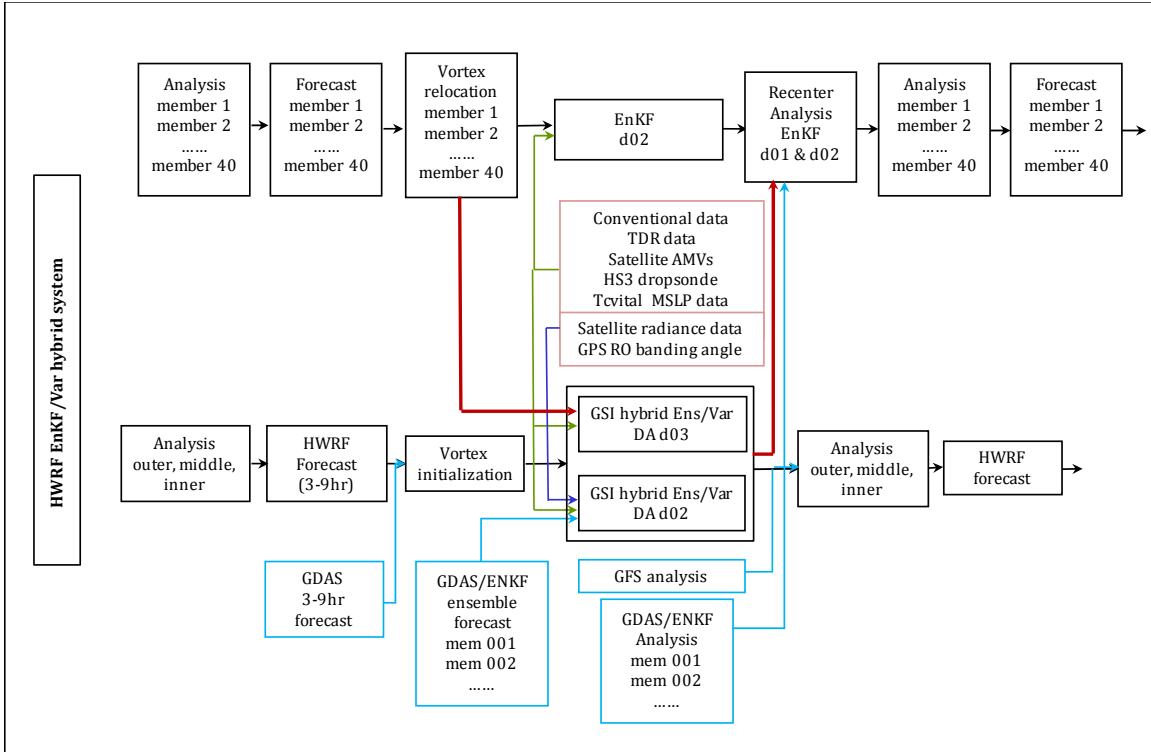


Figure 2-4: Flow diagram of self-cycled HWRF ensemble hybrid data-assimilation systems. The system is not supported with the HWRF 4.0a public release.

## 3. OCEAN AND WAVE COMPONENTS IN HWRF

### 3.1 Introduction

The HWRF system uses differing approaches for representing the ocean and waves in the various tropical cyclone basins (Table 3.1). The choices of which model to use, how to initialize, whether to couple one- or two-way, are carefully re-examined before each operational implementation to incorporate the latest scientific and technical-readiness developments.

The 2018 operational HWRF employs ocean coupling with MPIPOM-TC in the AL, EP, and CP basins and with HYCOM in the WP, NIO, SIO and SPAC basins. However, to minimize complexity, the HWRF v4.0a public release does not include HYCOM; instead, MPIPOM-TC is available for use in all basins, and is activated by default in the AL, CP, WP, and NIO basins. The v4.0a release only supports GDEM and RTOFS ocean initialization (See Table 3.1 for supported/unsupported ocean capabilities).

The 2018 HWRF operational implementation employs one-way coupling between the atmospheric and wave models in the AL, EP, and CP basins. The surface-wind forcing causes sea-surface waves but the feedback from surface waves on the atmosphere is disabled. Also, for purposes of reducing complexity for community users, WW3 is not included in the HWRF v4.0a public release.

The following sections describe in more detail the MPIPOM-TC model, the importance of ocean coupling for hurricane prediction, the model configuration, initialization, physics, and dynamics. The chapter ends with information about the coupler and output fields from the ocean.

The remainder of this chapter primarily describes capabilities of URI's MPIPOM-TC and of the coupler used in HWRF. Important features of MPIPOM-TC include: 1) MPI (to run on multiple processors); 2) high resolution; 3) large relocatable ocean domain; 4) improved physics; 5) several years of community-based improvements and bug fixes; 6) flexible initialization options; and 7) a variety of outputs for diagnostic purposes.

### 3.2 MPIPOM-TC Overview

The 3-D primitive-equation numerical ocean model that has become widely known as the POM was originally developed by Alan F. Blumberg and George L. Mellor in the late 1970s. One of the more popularly cited references for the early version of POM is Blumberg and Mellor (1987), in which the model was principally used for a variety of coastal ocean circulation applications. Many modifications were made to the POM code by a variety of users, and some of these changes were included in the "official" versions of the code housed at Princeton University, which has since been moved to Old Dominion University (ODU, <http://www.ccpo.odu.edu/POMWEB/>). Mellor (2004), currently available on the aforementioned website, is the latest version of the POM User's Guide and is an excellent resource for understanding the details of the more recent versions of the official POM code.

Table 3-1. Ocean model, ocean initialization data, and wave model used in operations and available in the HWRF v4.0a public release. Capabilities of the public release are broken down between the default and experimental options. FB stands for feature-based initialization, discussed later in this chapter. Wave model is not supported with the public release.

	Operational			V 4.0a public release			
Basin	Ocean Model	Initializa- tion	Wave model	Default Ocean Model	Other ocean model available	Default Initiali- zation	Other initiali- zations available
AL	MPIPOM- TC	GDEM + FB	WW3 one-way	MPIPOM- TC	N/A	GDEM + FB	None
EP	MPIPOM- TC	RTOFS	WW3 one-way	MPIPOM- TC	N/A	RTOFS	GDEM3
CP	MPIPOM- TC	RTOFS	WW3 one-way	MPIPOM- TC	N/A	RTOFS	GDEM3
WP	HYCOM	RTOFS	None	MPIPOM- TC	N/A	GDEM3	None
NIO	HYCOM	RTOFS	None	MPIPOM- TC	N/A	GDEM3	None
SIO	HYCOM	RTOFS	None	None	MPIPOM- TC	N/A	GDEM3
SPAC	HYCOM	RTOFS	None	None	MPIPOM- TC	N/A	GDEM3

In 1994, the version of POM available at the time was transferred to URI for the purpose of coupling to the GFDL hurricane model. At this point, POM code changes were made specifically to address the problem of the ocean's response to hurricane wind forcing to create a more realistic Sea Surface Temperature (SST) field for input to the hurricane model, and ultimately to improve 3- to 5-day hurricane intensity forecasts in the model. Initial testing showed hurricane intensity forecasts improved when ocean coupling was included (Bender and Ginis 2000). Since operational implementation of the coupled GFDL/POM model at NCEP in 2001, additional changes to POM were made at URI and subsequently implemented in the operational GFDL model, including improved ocean initialization (Falkovich et al. 2005; Bender et al. 2007; Yablonsky and Ginis 2008). This POM version was then coupled to the atmospheric component of the HWRF model in the AL basin (but not in the EP basin) before operational implementation of HWRF at

NCEP/EMC in 2007. Then for the 2012 operational implementation of HWRF, a simplified 1-D (vertical columnar) version of POM was coupled to the atmospheric component of HWRF in the EP basin. This version of POM, used as the ocean component of the operational HWRF model through 2013 to forecast tropical cyclones in the AL and EP basins, is known as POM-TC (Yablonsky et al. 2015b).

In 2014, the POM-TC was upgraded to a new high-resolution ocean model with message passing interface (MPI) capability (called MPIPOM –TC; Yablonsky et al. 2015a; Figure 3-1) adopted from sbPOM (Jordi and Wang 2012). The main motive was to have a single, 3-D, ocean model code for the AL and EP basins, with the capability to use a variety of ocean initial conditions. The two overlapping North Atlantic domains in POM-TC were replaced by a single unified transatlantic domain, a capability made possible by enabling parallelization through domain decomposition, resulting in a revised model dubbed MPIPOM-TC. MPIPOM-TC was coupled to HWRF and the coupled system was run operationally for the AL and EP basins.

In 2015, the operational HWRF was expanded to provide model guidance for all global TC basins. Subsequent tests conducted by EMC using 2015 storms indicated that intensity forecasts were substantially improved in the WP basin when HWRF was run in a coupled mode. Based on this result, since 2016 the operational HWRF has been configured to run in coupled mode in all the Northern Hemisphere TC basins, including the AL, EP, CP, WP, and NIO basins. In 2018, HWRF is run in coupled mode operationally for all oceanic basins. Starting in 2016, the NCEP global operational Real-Time Ocean Forecast System (RTOFS, Mehra and Rivin, 2010; <http://polar.ncep.noaa.gov/global/>) nowcast product was used to initialize the ocean model for the EP basin, which provides much more realistic ocean initial structure. RTOFS initialization was added for the CP basin in 2017. An increase in the vertical levels for MPIPOM-TC from 23 to 40 (with more vertical levels especially in the upper ocean), was added for the 2017 HWRF implementation, to better resolve upper-ocean responses especially under hurricane forcing.

In 2018, the atmosphere-ocean coupling capabilities of the operational HWRF have been extended to the basin-scale HWRF system (Alaka et. al 2017). The MPIPOM-TC is configured for a domain bounded in latitude from 5°N to 45°N and in longitude from 178°W to 15°W for the basin-scale HWRF. Such a large domain covers Gulf of Mexico, Caribbean, Atlantic, and east Pacific regions. Note: The basin-scale HWRF is not supported by the DTC.

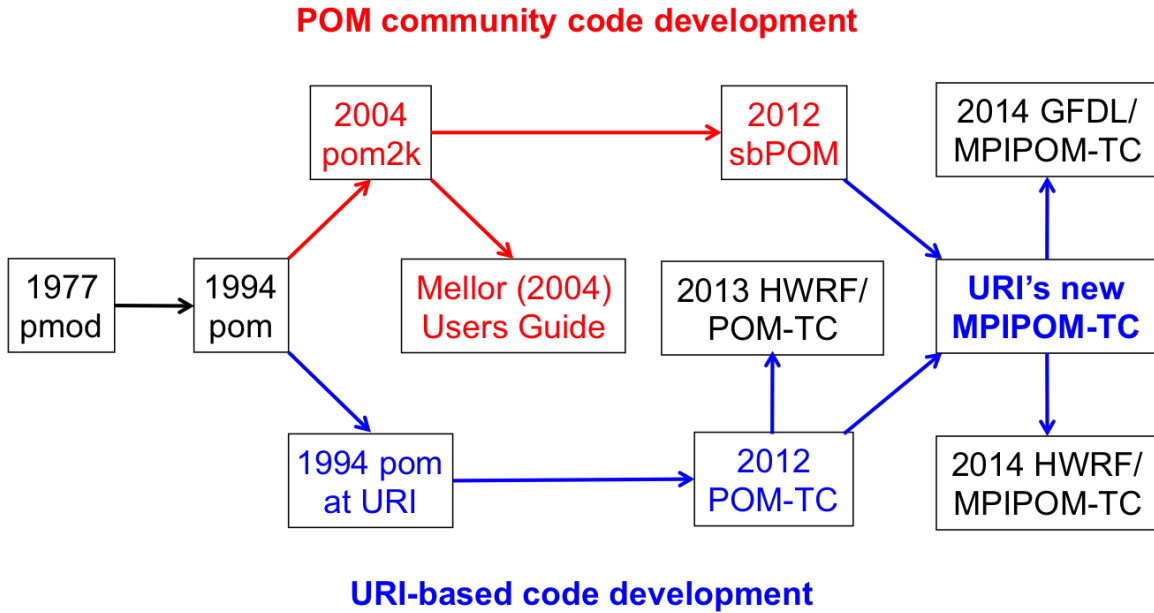


Figure 3-1: History of MPIPOM-TC development (adapted from Yablonsky et al. 2015a).

### 3.3 Purpose

The primary purpose of coupling a 3-D ocean model to HWRf (or to any hurricane model) is to create an accurate SST field for input into the atmospheric model. The SST field is subsequently used by the atmospheric model to calculate the surface heat and moisture fluxes from the ocean to the atmosphere. An uncoupled hurricane model with a static SST field is restricted by its inability to account for SST changes during model integration, which can contribute to a high-intensity bias (e.g., Bender and Ginis 2000). Similarly, a hurricane model coupled to an ocean model that does not account for fully 3-D ocean dynamics may only account for some of the hurricane-induced SST changes during model integration (e.g., Yablonsky and Ginis 2009, 2013).

### 3.4 Grid size, spacing, configuration, arrangement, coordinate system, and numerical scheme

To extend HWRf capabilities worldwide, MPIPOM-TC domains are designed to be relocatable to regions around the world (Yablonsky et al. 2015a). Currently, these regions include the Transatlantic, EP, CP, WP, NIO, South Indian, Southwest Pacific, and, Southeast Pacific (Fig. 3-2). Domain overlap helps to prevent loss of ocean coupling. To avoid domain-specific code, all worldwide domains are set to the same size: 869 (449) longitudinal (latitudinal) grid points, covering 83.2° (37.5°) of longitude (latitude) and yielding a horizontal grid spacing of ~9 km. Horizontal domain decomposition is 3 x 3, yielding 291 (151) local grid points on each of 9 processors. An additional grid for an idealized ocean region has been developed, but this grid is not yet supported to the community as part of the HWRf system.

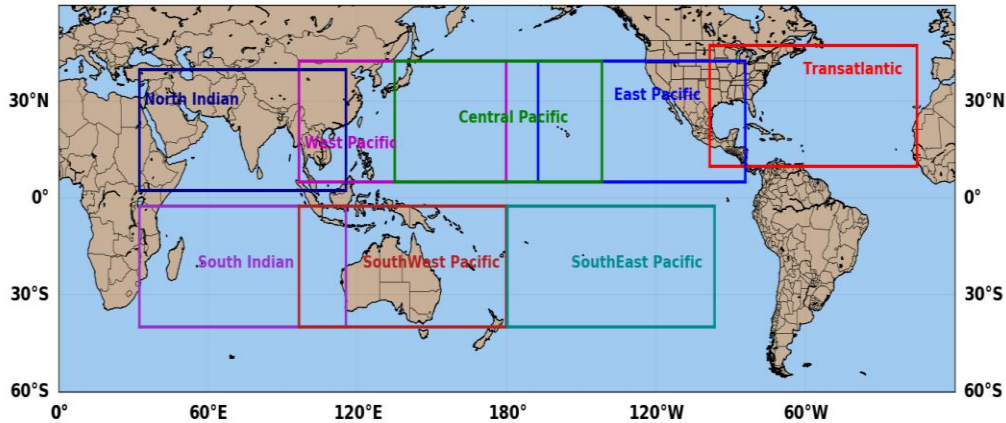


Figure 3-2: MPIPOM-TC worldwide ocean domains.

The vertical coordinate is the terrain-following sigma coordinate system (Phillips 1957; Mellor 2004; Figure 1 and Appendix D). There are 40 half-sigma vertical levels, where the level placement is scaled based on the bathymetry of the ocean at a given location. The greatest vertical spacing occurs where the ocean depth is 5500 m; here, the 40 full-sigma vertical levels (“Z” in Mellor 2004) are located at 0, 5, 10, 16, 23, 31, 40, 50, 62, 75, 90, 108, 128, 150, 176, 205, 238, 276, 320, 369, 426, 490, 563, 647, 742, 850, 974, 1115, 1276, 1459, 1668, 1906, 2178, 2488, 2840, 3243, 3701, 4224, 4820, and 5500 m depths.

During model integration, horizontal spatial differencing of the MPIPOM-TC variables occurs on the so-called staggered Arakawa-C grid. With this grid arrangement, some model variables are calculated at a horizontally shifted location from other model variables. See Mellor (2004), Section 4 for a detailed description and pictorial representations of MPIPOM-TC’s Arakawa-C grid.

MPIPOM-TC has a free surface and a split time step. The external mode is 2-D and uses a short time step (6 s) based on the well known Courant-Friedrichs-Lewy (CFL) condition and the external wave speed. The internal mode is 3-D and uses a longer time step (3 min) based on the CFL condition, the internal wave speed, and the frequency of coupling with the atmosphere (6 min). Horizontal time differencing is explicit, whereas the vertical time differencing is implicit. The latter eliminates time constraints for the vertical coordinate and permits using fine vertical resolution in the surface and bottom boundary layers. See Mellor (2004), Section 4, for a detailed description and pictorial representations of MPIPOM-TC’s numerical scheme.

### 3.5 Initialization

Prior to coupled model integration of the HWRF system, MPIPOM-TC is initialized with a realistic, 3-D temperature (T) and salinity (S) field and subsequently integrated to generate realistic ocean currents and incorporate the pre-existing hurricane-generated cold wake. The starting point for the ocean initialization in the AL basin is the GDEM monthly ocean T and S climatology (Teague et al. 1990), which has 0.5° horizontal grid spacing and 33 vertical z-levels located at 0, 10, 20, 30, 50, 75, 100, 125, 150, 200, 250,

300, 400, 500, 600, 700, 800, 900, 1000, 1100, 1200, 1300, 1400, 1500, 1750, 2000, 2500, 3000, 3500, 4000, 4500, 5000, and 5500 m depth. The GDEM climatology is then modified diagnostically by interpolating it in time to the MPIPOM-TC initialization date (using two months of GDEM data), horizontally interpolating it onto the MPIPOM-TC transatlantic grid, assimilating a land/sea mask and bathymetry data, and employing a feature-based modeling procedure that incorporates historical and near-realtime observations of the ocean in the western portion of the grid to 50°W longitude (i.e., the old POM-TC United grid; Falkovich and Lord 2005; Yablonsky and Ginis 2008). This feature-based modeling procedure has also been configured to utilize alternative T and S climatologies with 0.25° grid spacing, including a newer GDEM climatology and a Levitus climatology (Boyer and Levitus 1997), but tests with these climatologies in the AL basin in the GFDL model do not show increased skill over the original GDEM climatology used operationally (Yablonsky et al. 2006). To prevent T and S discontinuities across 50°W longitude, the GDEM T and S values that have been modified by the feature-based modeling procedure west of this longitude are blended with the raw GDEM T and S values that have not been modified by the feature-based modeling procedure east 50°W longitude.

The basic premise of the feature-based modeling procedure is that major oceanic fronts and eddies in the western North Atlantic Ocean, namely the Gulf Stream (GS), the Loop Current (LC), and Loop Current warm and cold core rings (WCRs and CCRs), are poorly represented by the GDEM climatology's T and S fields. By defining the spatial structure of these fronts and eddies using historical observations gathered from various field experiments (Falkovich and Lord 2005, Section 3), cross-frontal "sharpening" of the GDEM T and S fields can be performed to obtain more realistic fields. These sharpened fields yield stronger geostrophically adjusted ocean currents along the front than would be obtained directly from GDEM, causing the former to be more consistent with observations than the latter. In addition, algorithms were incorporated into the feature-based modeling procedure to initialize the GS and LC with prescribed paths, and to insert WCRs and CCRs in the Gulf of Mexico based on guidance from near-realtime observations, such as satellite altimetry (Yablonsky and Ginis 2008, Section 2).

After the aforementioned diagnostic modifications to the GDEM climatology (including the feature-based modifications in the transatlantic region), at the beginning of what is referred to as ocean spin-up "phase 1" (also commonly known as "phase 3" for historical reasons), the upper-ocean temperature field is modified by assimilating the realtime daily SST data (with 1° grid spacing) used in the operational NCEP GFS global analysis (hereafter NCEP SST; Reynolds and Smith 1994). Further details of the SST assimilation procedure can be found in Yablonsky and Ginis (2008, Section 2). Finally, the 3-D T and S fields are interpolated from the GDEM z-levels onto the MPIPOM-TC vertical sigma levels, and the density (RHO) is calculated using the modified United Nations Educational, Scientific, and Cultural Organization (UNESCO) equation of state (Mellor 1991), ending the diagnostic portion of the ocean initialization.

Ocean spin-up phase 1 involves 48 h of MPIPOM-TC integration, primarily for dynamic adjustment of the T and S (and ultimately, RHO) fields and generation of geostrophically adjusted currents. During phase 1, SST is held constant. Once phase 1 is complete, the phase 1 output is used to initialize ocean spin-up "phase 2" (also commonly known as

“phase 4” for historical reasons). During phase 2, the cold wake at the ocean surface and the currents produced by the hurricane prior to the beginning of the coupled model forecast are generated by a 72-h integration of MPIPOM-TC with the observed hurricane surface wind distribution provided by NOAA’s NHC along the storm track. Or, if the observed wind field is very weak, phase 2 is skipped. Once phase 2 is complete (or skipped), the phase 2 output (or phase 1 output) is used to initialize the MPIPOM-TC component of the coupled HWRF.

The procedure for operational ocean initialization in the EP and CP are quite distinct from the one used in the AL. Up until 2015, the EP was initialized using GDEM3, but starting from the 2016 operational HWRF implementation, MPIPOM-TC utilizes the NCEP global eddy resolving  $1/12^\circ$  operational RTOFS temperature and salinity data for initialization in the EP basin. The NCEP global RTOFS runs once a day and produces 2-day nowcasts and 6-day forecasts using the daily initialization fields produced at the Navy Oceanographic Office using the Navy Coupled Ocean Data Assimilation (NCODA), a 3-D multi-variate data assimilation methodology (Cummings 2005), which facilitates the ingestion of various datasets including *in situ* profiles of temperature and salinity from a variety of sources and remotely sensed SST, SSH, and sea-ice concentrations. The RTOFS forecast system is forced with 3-h momentum, radiation, and precipitation fluxes from the operational GFS fields. The 3-D temperature and salinity fields from the RTOFS nowcast valid at 00UTC is then used for ocean model initialization for all four HWRF forecast cycles in the same day (00UTC, 06UTC, 12UTC, 18UTC). Horizontal and vertical interpolations are carried out to map the data from the RTOFS grid to the POM grid. Ocean spin-up phase 1 involves 48 h of MPIPOM-TC integration primarily for dynamic adjustment of mass and current fields. Unlike the climatology-based initialization used by HWRF in the AL basin, the cold-wake generation (phase 2 Ocean spin up) is not employed when using RTOFS for initialization because the cold wake associated with the storm is typically already present in the RTOFS fields. Up until 2017, MPIPOM-TC configured for EP was used to run some of the storms originated in the central Pacific. However, sometimes this results in loss of coupling during 126-h forecast run when the storms move out of the EP domain. In 2018, MPIPOM-TC with RTOFS-based initialization was configured for a new CP domain. The decision to employ RTOFS was based on retrospective tests that indicated that the RTOFS initialization improves HWRF intensity forecasting, especially for storms that intensify rapidly. The basin-scale HWRF also uses the RTOFS based MPIPOM-TC as its ocean component.

In WP and NIO basins, HWRF v4.0a uses GDEM3 climatology data together with GFS model SST output to create the ocean initial conditions. For those using the non-default coupling with the ocean in the SIO and SPAC versions, this initialization method is also available.

One particular innovative and important aspect of MPIPOM-TC is the development of flexible, plug-and-play, Fortran-based initial condition modules (Yablonsky et al. 2015a). In addition to the feature-based initialization procedure in the AL and RTOFS-based initialization in the EP and CP, initial condition modules have also been developed for the stand-alone NCODA daily *T* and *S* fields (Cummings 2005; Cummings and Smedstad 2013), recent version of GDEMv3 (Carnes 2009) and versions of the HYbrid Coordinate

Ocean Model (HYCOM) that use NCODA (Chassignet et al. 2009) in all TC basins. All of these ocean products are available in the public domain for realtime tropical cyclone forecasting. However, the DTC only supports the operational configuration that uses the GDEM and RTOFS-based initializations.

### 3.6 Physics and dynamics

As previously stated, the primary purpose of coupling the MPIPOM-TC to the HWRF is to create an accurate SST field for input into the HWRF. An accurate SST field requires ocean physics that can generate accurate SST change in response to wind (and to a lesser extent, thermal) forcing at the air-sea interface. The leading-order mechanism driving SST change induced by wind forcing is vertical mixing and entrainment in the upper ocean. Vertical mixing occurs because wind stress generates ocean surface-layer currents, and the resulting vertical current shear leads to turbulence, which then mixes the upper ocean and entrains colder water from the thermocline up into the well mixed ocean surface layer, ultimately cooling the SST. In MPIPOM-TC, turbulence is parameterized using a second moment turbulence closure submodel, which provides the vertical mixing coefficients. This submodel is widely known as the Mellor-Yamada Level 2.5 turbulence closure model (Mellor and Yamada 1982; Mellor 2004, Sections 1 and 14).

If vertical mixing (and the resulting entrainment) was the only ocean response to hurricane wind forcing that impacted SST, then a 1-D (vertical columnar) ocean model would be sufficient. However, idealized experiments comparing 3-D and 1-D versions of POM-TC (or equivalently, MPIPOM-TC), show that the 1-D (MPI)POM-TC underestimates SST cooling for slow-moving hurricanes (Yablonsky and Ginis 2009). This finding is consistent with previous studies (e.g., Price 1981). The primary reason a 1-D ocean model fails to capture the magnitude of SST cooling for slow-moving storms is the neglect of upwelling, which is a fully 3-D process. The cyclonic wind stress induced by a hurricane creates divergent surface currents in the upper ocean, causing upwelling of cooler water from the thermocline towards the sea surface. For slow-moving storms, this upwelling increases the efficiency with which vertical mixing can entrain cooler water from the thermocline into the well mixed ocean surface layer, ultimately cooling the SST. Finally, horizontal advection, which is also neglected by 1-D ocean models, may impact the SST distribution, especially in oceanic fronts and eddies where strong background currents exist (Yablonsky and Ginis 2013). Horizontal diffusion in MPIPOM-TC, which generally has relatively little impact on the SST over the time scale of the hurricane, uses Smagorinsky diffusivity (Smagorinsky 1963).

### 3.7 Coupling

At NCEP, a coupler was developed to act as an independent interface between the HWRF atmospheric component and the MPIPOM-TC or HYCOM ocean component. During forecast integration of HWRF, the east-west and north-south momentum fluxes at the air-sea interface (“wusurf” and “wvsurf” in Mellor 2004) are passed from the atmosphere to the ocean, along with temperature flux (“wtsurf”) and the shortwave radiation incident on the ocean surface (“swrad”). During forecast integration of MPIPOM-TC, the SST is passed from the ocean to the atmosphere.

The time integration of the coupled system is carried out with three executables working in Multiple Program Multiple Data (MPMD) mode for the HWRF atmospheric component, MPIPOM-TC, and the coupler. The coupler serves as a hub for MPI communications between HWRF atmosphere and MPIPOM-TC and performs the interpolation of the surface fluxes from the fixed and moving HWRF atmospheric grids to the MPIPOM-TC grid and of the SST from the MPIPOM-TC grid to the two outermost HWRF atmospheric grids. A generalized bilinear interpolation for non-rectangular quadrilateral grid cells is used. Only sea-point values of the surface fields are employed for the interpolation. For missing values due to model domain inconsistencies, a limited extrapolation within the relevant connected components of the model sea surface is used. The computations that establish the mutual configuration of the grids (interpolation initialization) are performed prior to the forecast, using an algorithm with the number of operations reduced to the order of  $N^3$ , where  $N$  is the number of points in a grid row. The coupler also provides run-time analysis and diagnostics of the surface data.

Finally, the coupler includes the capability for three-way coupling, in which the third model component is the WW3 wave model. One-way coupling with WW3 is used operationally in the AL, EP, and CP basins but not supported as part of the v4.0a public release. Although the capability of three-way coupling among the WRF model, the MPIPOM-TC, and WW3 is available in the HWRF system, additional tests are needed before it can be implemented in the operational configuration.

### 3.8 Output fields for diagnostics

Some of the 2-D and 3-D MPIPOM-TC variables are saved in netCDF output files for diagnostic purposes every 6 h (by default). The format of the names of these netCDF output files is “name.NNNN.nc” where “name” is the storm name and “NNNN” is the four-digit file number. The first output time is always the model initialization time (for the particular model phase being simulated), and can therefore be used to diagnose the current model phase’s initial condition. Note that variables in these netCDF output files retain their native MPIPOM-TC C-grid and sigma-level navigation information, so “u,” “v,” “wusurf,” and “wvsurf,” for example, are defined at horizontally-shifted locations from “t” and “s,” and “q2” and “w” are defined at vertically-shifted locations from “t” and “s.”

## 4. PHYSICS PACKAGES IN HWRF

The HWRF system was designed to utilize the strengths of the WRF software system, the well tested NMM-Edynamic core, and the physics packages of other NCEP modeling systems, such as the NAM, the GFS, and the now-retired GFDL hurricane model. Since the HWRF system became operational in 2007, the physics packages of the HWRF model have been upgraded on a yearly basis, and this document describes the HWRF physics suites implemented for the 2017 hurricane season.

The 2018 operational implementation included updated radiation schemes, as well as air-sea momentum and enthalpy exchange coefficients for the surface-layer scheme. These changes were designed to increase the realism of physical processes in HWRF, and therefore more closely align the HWRF predictions with observations. The physics packages of HWRF will be briefly described and contrasted with other NOAA models such as GFS, GFDL, and NAM. Descriptions of the GFS and its physics suite can be found at <http://www.emc.ncep.noaa.gov/GFS/doc.php> and [http://www.dtcenter.org/GMTB/gfs\\_phys\\_doc](http://www.dtcenter.org/GMTB/gfs_phys_doc), while more information on additional physics available in the WRF model are available in Skamarock et al. (2008) and at <http://www2.mmm.ucar.edu/wrf/users/tutorial/201607/physics.pdf>. See Bender et al. (2007) for more information on the now-retired GFDL hurricane model. Note that the POM coupling component of HWRF is described in Section 3.

### 4.1 HWRF physics

This section outlines the physical parameterizations used in the operational HWRF model, which fall into the following categories: (1) microphysics, (2) cumulus parameterization, (3) surface layer, (4) PBL, (5) LSM, and (6) radiation. It closely follows the basic WRF physics tutorial of Jimmy Dudhia ([https://dtcenter.org/events/wrf-nmm\\_tutorial06\\_summer/Presentations/NMM\\_Physics\\_Dudhia.pdf](https://dtcenter.org/events/wrf-nmm_tutorial06_summer/Presentations/NMM_Physics_Dudhia.pdf)). Horizontal diffusion, which may also be considered part of the physics, is not described in this section. The WRF system has been expanded to include all HWRF physics and, for each category, the operational HWRF employs a specific choice within the WRF spectrum of physics options. The HWRF physics initially followed the physics suite used by the now-retired GFDL hurricane model, but in the last few years, several modifications have been introduced.

In the WRF framework, the physics section is insulated from the rest of the dynamics solver by the use of physics drivers. These drivers are located between the following solver-dependent steps: pre-physics preparations and post-physics modifications of the tendencies. The physics preparation involves filling arrays with physics-required variables, such as temperature, pressure, heights, layer thicknesses, and other state variables in MKS units at half-level and full levels. The velocities are de-staggered so that the physics code is independent of the dynamical solver's velocity staggering. Because HWRF uses the E-grid on the rotated lat-long projection of the WRF-NMM dynamic core, this velocity de-staggering involves interpolating the momentum variables from the velocity to the mass grid points. Physics packages compute tendencies for the un-staggered velocity components, potential temperature, and moisture fields. The solver-dependent post-physics step re-staggeres the tendencies as necessary, couples tendencies

with coordinate metrics, and converts to variables or units appropriate to the dynamics solver. As in other regional models, the physics tendencies are generally calculated less frequently than dynamic tendencies for computational expediency. The interval of physics calls is controlled by namelist parameters.

## 4.2 Microphysics parameterization

Microphysics parameterizations explicitly handle the behaviors of hydrometeor species by solving prognostic equations for their mixing ratio and/or number concentration, so they are sometimes called explicit cloud schemes (or gridscale cloud schemes) in contrast to cumulus schemes, which parameterize sub-grid scale convection. The adjustment of water vapor exceeding saturation values is also included inside the microphysics. The treatment of water species such as rain, cloud, ice, and graupel was first utilized in the development of cloud models, which simulated individual clouds and their interactions. Gradually, as it became more computationally feasible to run simulations at high grid resolutions, microphysics schemes were incorporated into regional atmospheric models. At high enough resolution (~1 km or less), convective parameterization of cloud processes may not be needed because convection can be resolved explicitly by a microphysics scheme. In the simpler microphysics schemes (single-moment schemes), such as the one used in HWRF, only the mixing ratios of the water species are carried as predicted variables, while the number concentration of the variables is assumed to follow standard distributions. If number concentrations are also predicted, the schemes are coined “double moment.” A further sophistication in microphysics schemes is introduced if the water species are predicted as a function of size. This added level of complexity is termed a “bin” scheme. The present HWRF model, like the NAM, uses the Ferrier-Aligo (FA) scheme, simplified so that the cloud microphysical variables are considered in the physical column, but only the combined sum of the microphysical variables, the total cloud condensate, is advected horizontally and vertically. A possible upgrade of HWRF microphysics would be to extend the FA scheme to handle advection of cloud species. Note that the HWRF model can now be run in research mode with alternate microphysics packages, including the Thompson and WRF single-moment 6-class (WSM6) parameterizations.

### *The Ferrier-Aligo scheme*

The FA microphysics scheme is a modified version of the tropical Ferrier microphysics scheme, which is based on the Eta Grid-scale Cloud and Precipitation scheme (Rogers et al. 2001; Ferrier et al. 2002). The scheme predicts changes in water vapor and condensate in the forms of cloud water, rain, cloud ice, and precipitation ice (snow/graupel/sleet). The individual hydrometeor fields are combined into total condensate, and the water vapor and total condensate are advected in the model. This approach is taken for computational expediency. Local storage arrays retain first-guess information of the contributions of cloud water, rain, cloud ice, and precipitation ice of variable density in the form of snow, graupel, or sleet (Figure 4-1).

The density of precipitation ice is estimated from a local array that stores information on the total growth of ice by vapor deposition and accretion of liquid water. Sedimentation is treated by partitioning the time-averaged flux of precipitation into a grid box between

local storage in the box and leaking through the bottom of the box. This approach, together with modifications in the treatment of rapid microphysical processes, permits large time steps to be used with stable results. The mean size of precipitation ice is assumed to be a function of temperature following the observational results of Ryan (1996). Mixed-phase processes are now considered at temperatures warmer than  $-40\text{ }^{\circ}\text{C}$ , whereas ice saturation is assumed for cloudy conditions at colder temperatures.

The FA scheme was developed to improve simulations of deep convective clouds in high-resolution modeling configurations, particularly in the 1-4-km range of grid spacings. The modified microphysics assumes the maximum number concentration of large ice varies in different cloud regimes. Some of the relevant changes in the FA scheme, as compared to the tropical Ferrier scheme, are:

1. Maximum number concentration of large ice (NLI) is a function of Rime Factor (RF) and temperature. In the *stratiform regime*, defined as  $\text{RF} < 10$ , the maximum NLI ranges from 10-20  $\text{l}^{-1}$ . In the *convective regime*, defined as  $\text{RF} \geq 10$ , maximum  $\text{NLI}=1\text{ l}^{-1}$ . In the *hail regime*, defined as  $\text{RF} \geq 10$  with mean diameters  $\geq 1\text{ mm}$ , NLI also does not exceed  $1\text{ l}^{-1}$ ;
2. Additional supercooled liquid water;
3. Increased radar backscatter from wet, melting ice, and at  $T < 0\text{ }^{\circ}\text{C}$  when rain and ice coexist in intense updrafts;
4. Modest reduction in rimed-ice fall speeds; and
5. Cloud ice production algorithm.

Minor updates in the FA scheme were introduced to HWRF in 2017, responding to reflectivity biases and lack of stratiform precipitation reported by comparisons with observations over land. A drizzle parameterization (Aligo et al. 2017) allowing for smaller, more numerous drops was added to the scheme to reduce high reflectivity bias of PBL clouds. The largest possible number concentration of snow was increased to  $250\text{ L}^{-1}$ , reducing a high reflectivity bias associated with anvil clouds. A constant mean raindrop size during rain evaporation is now used to reduce evaporation and increase stratiform precipitation.

A configuration of the FA scheme with separate advection of the species and of the mass-weighted RF ( $Q_s * \text{RF}$ ) is being tested for HWRF and is not yet supported. Advecting the mass-weighted RF helps the establishment of higher RFs at temperatures colder than  $-40\text{ }^{\circ}\text{C}$ , allowing for more realistic RFs in the convective region. Tests in the North American Model (NAM) suggested that this treatment could improve simulation of convective reflectivity more closely matching observations in many cases. For more details about the FA scheme, see Aligo et al. (2014).

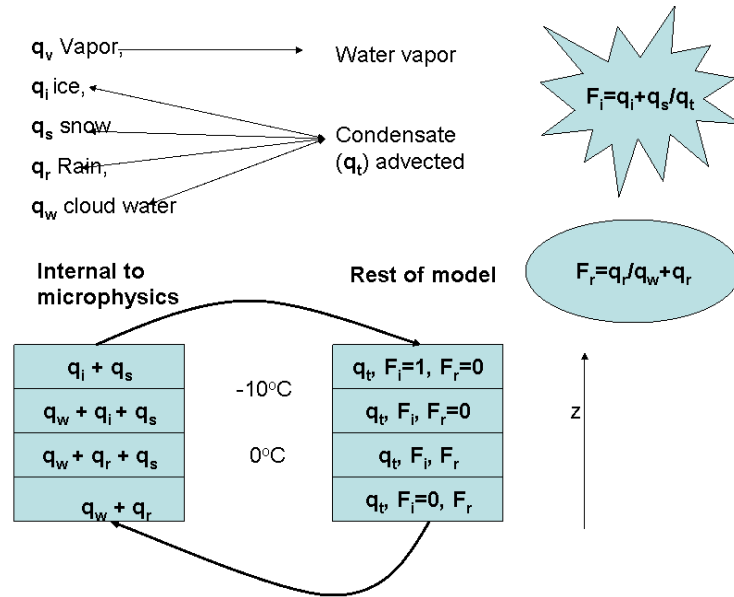


Figure 4-1: Water species used internally in the FA microphysics and their relationship to the total condensate. The left column represents the quantities available inside the microphysics scheme (mixing ratios of vapor, ice, snow, rain, and cloud water). The right column represents the quantities available in the rest of the model: only the water vapor and the total condensate are advected. After advection is carried out, the total condensate is redistributed among the species based on fractions of ice and rain water.

### 4.3 Cumulus parameterization

Cumulus parameterization schemes, or convective parameterization schemes, are responsible for the sub-grid-scale effects of deep and/or shallow convective clouds. These schemes are intended to represent vertical fluxes unresolved by grid-scale microphysics schemes such as updrafts, downdrafts, and compensating motion outside the clouds. In its early development, convective parameterization was believed necessary to avoid possible numerical instability due to simulating convection at coarse resolutions. The schemes operate only on individual vertical columns where the scheme is triggered and provide vertical heating and moistening profiles. Some schemes also provide hydrometeor and precipitation field tendencies in the column, and some schemes, such as the one used in HWRF, provide momentum tendencies due to convective transport of momentum. The schemes all provide the convective component of surface rainfall.

Some cumulus parameterizations, such as the one employed in earlier versions of HWRF, are theoretically only valid for coarser grid sizes, (e.g., greater than 10 km), where they are necessary to properly release latent heat on a realistic time scale in the convective columns. They assume that the convective eddies are entirely at a sub-grid-scale and are invalid for grid resolutions finer than 10 km, in which updrafts may be partially resolved. To address this issue, since 2016, HWRF has adopted an extension of the Simplified Arakawa-Schubert (SAS) scheme that is scale-dependent and does not rely on scale separation between the resolved and subgrid convection. For this reason, the cumulus

parameterization is activated in both the parent domain (13.5-km horizontal grid spacing) and two nests (4.5- and 1.5-km horizontal grid spacing).

### ***The Scale-Aware Simplified Arakawa-Schubert (SASAS) scheme***

The SASAS cumulus scheme is a modified version of SAS scheme, which is briefly described in this section. For more details about the SAS scheme, readers are referred to scientific documentations of earlier versions of the HWRF system and references therein.

The Arakawa and Schubert (1974) cumulus parameterization was simplified by Grell (1993) to consider only one cloud top at a specified time and location and not a spectrum of cloud sizes, as in the computationally expensive original scheme. Further modifications by Pan and Wu (1995) and adaptation for operational use resulted in the scheme known as SAS, which was employed in the GFS and GFDL models. One important modification made to the SAS scheme employed in the HWRF and GFS models in 2011 was the use of a single cloud-top value per grid box, instead of the original use of a random distribution of cloud tops. The scheme, described in detail in some publications (Pan and Wu 1995; Hong and Pan 1998; Pan 2003; Han and Pan 2011), has also been revised to make cumulus convection stronger and deeper by increasing the maximum allowable cloud-base mass flux and having convective overshooting from a single cloud top.

While the operational HWRF has always relied on a deep convection parameterization, a shallow convection scheme has been in use only since 2012. The parameter used to differentiate shallow from deep convection is the depth of the convective cloud. When the extent of the convective cloud is greater than 150 hPa, convection is defined as deep; otherwise it is treated as shallow. In the HWRF model, precipitation from shallow convection is prohibited when the convection top is located below the PBL top and the thickness of the shallow convection cloud is less than 50 hPa. These customizations were made to remove widespread light precipitation in the model domain over open ocean areas. Note that because the shallow convection scheme requires knowledge of the PBL height, it needs to be run in conjunction with a PBL parameterization that provides that information. In the current code, only the GFS PBL scheme has been tested to properly communicate the PBL height to the HWRF SASAS parameterization.

The SASAS employs a cloud model that incorporates a downdraft mechanism as well as evaporation of precipitation. Entrainment of the updraft and detrainment of the downdraft in the sub-cloud layers is included. Downdraft strength is based on vertical wind shear through the cloud.

The SASAS scheme uses a scale-aware feature to modulate the updraft area according to the horizontal grid spacing. The cloud-base mass flux of an updraft over a grid can be written as,

$$m'_b = (1 - \sigma_u)^2 m_b \quad (4.3.1),$$

where  $\sigma_u$  is the updraft area fraction (0 ~ 1.0),  $m_b$  is the original cloud-base mass flux from the SAS quasi-equilibrium closure, and  $m'_b$  is the updated cloud-base mass flux with a finite area  $\sigma_u$ . The key is to estimate the updraft area fraction.

In the SASAS, the updraft area fraction is computed as,

$$\sigma_u = \frac{\pi R_{conv}^2}{A_{grid}} \quad (4.3.2),$$

where  $A_{grid}$  is the horizontal area of the grid cell, and  $R_{conv}$  is the updraft radius, which is estimated as  $0.2/\varepsilon$ .  $\varepsilon$  is the updraft entrainment rate. Grell and Freitas (2014) uses a constant  $\varepsilon$ ,  $7 \times 10^{-5}$ , while SASAS uses the actual entrainment rate at the cloud base.

Figure 4-2 presents an example of the distribution of  $\sigma_u$  of deep updrafts for the 6-h forecast in a simulation of Hurricane Sandy initialized at 2012102600. The fractional area generally increases as grid size decreases.

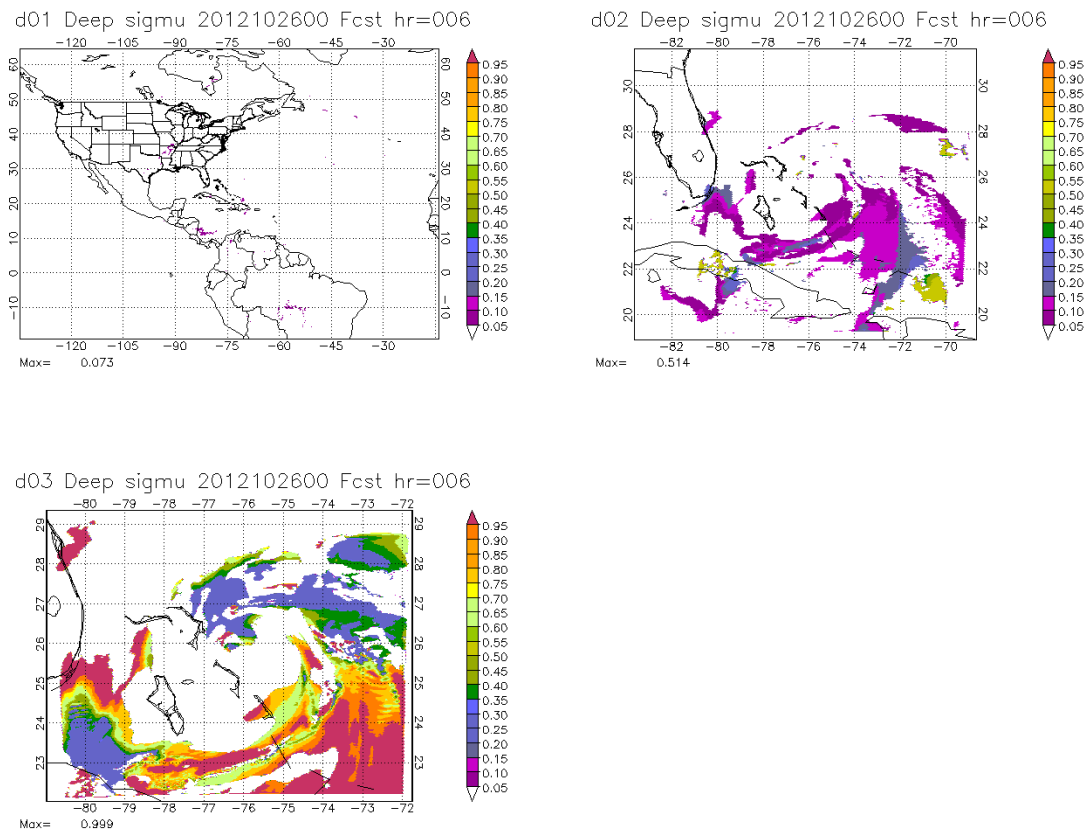


Figure 4-2: Six-h forecast of fractional area of deep updrafts over the parent domain (18-km grid spacing, top left), middle nest (6 km, top right), and innermost nest (2 km, bottom left) from a simulation of Hurricane Sandy initialized at 2012102600.

The SASAS scheme adopted in 2016 differs from the previously used SAS in various ways, in addition to the scale-aware aspects. Some examples are:

- 1) Adoption of a convective turnover time as the cumulus time scale in the cloud-mass flux computation.

- 2) Additional convective inhibition in the trigger function, suppressing unrealistically noisy (popcorn-like) rainfall especially over high terrain.
- 3) Decrease of rain conversion rate with decreasing air temperature above the freezing level, based on cloud-resolving model results.
- 4) Tuning of the non-precipitating shallow cumulus convection to reduce excessive light rain.

Further updates in the scale-aware convection scheme in 2017 (Han et al. 2017), can be summarized as follows:

- 1) For deep convection, the cloud-base mass flux is a function of mean updraft velocity when grid spacing is smaller than 8 km, rather than derived from Arakawa-Schubert's quasi-equilibrium assumption.
- 2) For shallow convection, the cloud-mass flux is a function of mean updraft velocity, rather than a function of convective velocity scale.

When the advective time ( $ADT$ ) is less than the convective turnover time ( $CTT$ ) of a cumulus cloud, the convective mixing is not fully conducted, the base mass flux is reduced by  $ADT/CTT$  )

- 3) and the base mass flux is reduced by  $ADT/CTT$ .

Other updates include the reduction of the decrease rate of the rain conversion rate with decreasing air temperature above the freezing level, entrainment enhancement in dry environments, precipitating shallow convection to reduce excessive low clouds, and the use of a cumulus depth of 200 hPa (i.e., instead of 150 hPa) as separation between deep and shallow convections.

#### 4.4 Surface-layer parameterization

The surface-layer schemes calculate friction velocities and exchange coefficients that enable the calculation of surface heat, moisture, and momentum fluxes by the LSM. Over water, the surface fluxes and surface diagnostic fields are computed by the surface-layer scheme itself. These fluxes, together with radiative surface fluxes and rainfall, are used as input to the ocean model. Over land, the surface-layer schemes are capable of computing both momentum and enthalpy fluxes as well. However, if a land model is invoked, only the momentum fluxes are retained and used from the surface-layer scheme. The schemes provide no tendencies, only the stability-dependent information about the surface layer for the land-surface and PBL schemes.

Each surface-layer option is normally tied to a particular boundary-layer option but, in the future, more interchangeability may become available. The HWRF operational model uses a modified GFDL surface layer and a modified GFS PBL scheme.

##### ***The HWRF surface-layer scheme***

The surface-layer parameterization over water in HWRF is based on Kwon et al. (2010), Powell et al. (2003), and Black et al. (2007). The air-sea flux calculations use a bulk

parameterization based on the Monin-Obukhov similarity theory (Sirutis and Miyakoda 1990; Kurihara and Tuleya 1974). The HWRF scheme retains the stability-dependent formulation of the GFDL surface parameterization, with the exchange coefficients now recast to use momentum and enthalpy roughness lengths that conform to observations. In this formulation, the neutral drag coefficient  $C_d$  is defined as:

$$C_d = \kappa^2 \left( \ln \frac{z_m}{z_0} \right)^{-2}, \quad (4.4.1)$$

where  $\kappa$  is the von Karman constant ( $= 0.4$ ),  $z_0$  is the roughness length for momentum, and  $z_m$  is the lowest model-level height. The neutral heat and humidity coefficients (assumed equal,  $C_k$ ) are expressed as

$$C_k = \kappa^2 \left( \ln \frac{z_m}{z_0} \right)^{-1} \left( \ln \frac{z_m}{z_T} \right)^{-1}, \quad (4.4.2)$$

where  $z_T$  is the roughness length for heat and humidity.

Since the 2016 HWRF implementation,  $C_d$  and  $C_k$  are prescribed as a function of wind speed at the standard 10-m level; this is in contrast to its early versions where the first-level wind speed was used. This supports comparisons with observations of  $C_d$  and  $C_k$ , which are usually given as a function of 10-m wind speed.

These prescribed values of  $C_d$  and  $C_k$  are valid only in neutral conditions. In HWRF,  $C_d$  and  $C_k$  also depend on atmospheric stability, and are greater in unstable conditions when vertical mixing is more vigorous. Over land, the roughness length in HWRF is specified (as in the NAM model) with  $z_0 = z_T$ . Over water, the HWRF momentum roughness length,  $z_0$ , is obtained by inverting Equation 4.4.1. The enthalpy roughness length,  $z_T$ , is obtained by inverting Equation 4.4.2. Note that, since the 2016 implementation,  $z_0$  and  $z_T$  are calculated as a function of standard 10-m wind speed, rather than the first-level wind speed.

In the 2017 HWRF implementation, the surface exchange coefficients ( $C_d$  and  $C_k$ ) and correspondingly surface roughness lengths ( $z_0$  and  $z_T$ ) are further refined to be consistent with observational evidence-supported relationships to sea-surface wind at 10-m height. Figure 4-3 provides the 2017 HWRF version relationships between surface exchange coefficients and 10-m wind, comparing with 2015 and 2016 HWRF versions as well as the available observational evidence. For the drag coefficient, under low-to-moderate winds, the 2017 HWRF version  $C_d$  fits to the COARE algorithm V3.5 (Edson et al. 2013), which is supported by numerous observations. Under high-wind conditions, the 2017 HWRF version  $C_d$  comes from curve-fitting to available field measurements from recent observations under high winds (Powell et al. 2003; Jarosz et al. 2007; French et al. 2007; Bell et al. 2012; Holthuijsen et al. 2012; Potter et al. 2015; Zhao et al. 2015; Bi et al. 2015; Richter et al. 2016). For the surface sensible and latent heat-exchange coefficient, the 2017 HWRF version  $C_k$  takes the sea-surface scalar roughness from the

COARE algorithm V3.0 (Fairall et al. 2003), which again, was obtained from numerous field measurements under low-to-moderate winds. Meanwhile, for high-wind conditions, the 2017 HWRf version  $C_k$  is the same as 2015 HWRf version  $C_k$ .

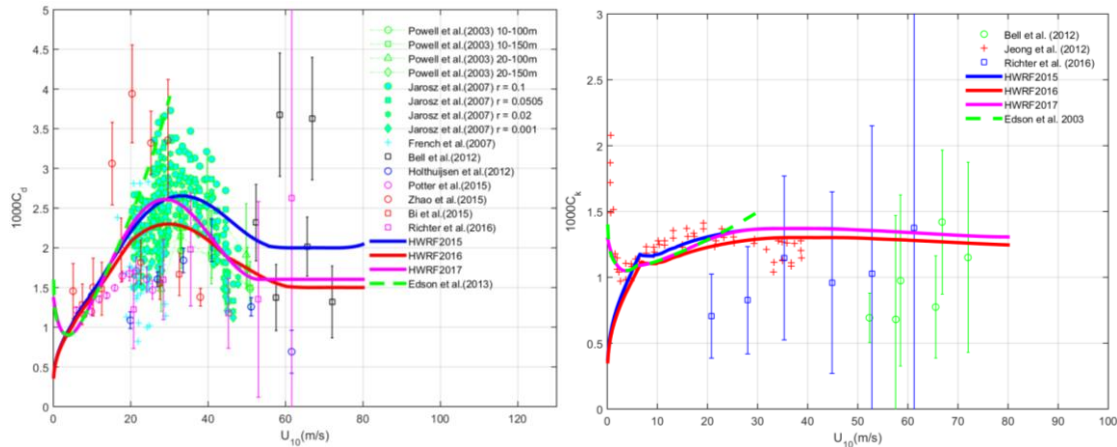


Figure 4-3: Sea-surface drag coefficient  $C_d$  (left), and heat exchange coefficient  $C_k$  (right), as a function of wind speed at 10 m above the surface for the 2017 HWRf model (magenta curve), comparing with the 2015 (blue curve) and 2016 (red curve) HWRf versions, together with various observational evidence.

## 4.5 Land-surface model

LSMs use atmospheric information from the surface-layer scheme, radiative forcing from the radiation scheme, and precipitation forcing from the microphysics and convective schemes, together with internal information on the land's state variables and land-surface properties, to provide heat and moisture fluxes over land points and sea-ice points. These fluxes provide a lower boundary condition for the vertical transport done in the PBL schemes (or the vertical diffusion scheme in the case where a PBL scheme is not run, such as in large-eddy mode). Land-surface models have various degrees of sophistication in dealing with thermal and moisture fluxes in multiple layers of the soil and also may handle vegetation, root, and canopy effects and surface snow-cover prediction. In WRF, the LSM provides no tendencies, but updates the land-state variables, which include the ground (skin) temperature, soil temperature profile, soil moisture profile, snow cover, and possibly canopy properties. There is no horizontal interaction between neighboring points in the LSM, so it can be regarded as a 1-D-column model for each WRF land grid-point, and many LSMs can be run in a stand-alone mode when forced by observations or atmospheric model input. One of the simplest land models involves only one soil layer (slab) and predicts only surface temperature. In this formulation, all surface fluxes (both enthalpy and momentum) are predicted by the surface-layer routines. HWRf uses the Noah LSM.

### The Noah LSM

The Noah LSM is widely used by NCEP and WRF community, and has a long history of development (Mahrt and Ek 1984; Mahrt and Pan 1984; Pan and Mahrt 1987; Chen et al. 1996; Schaake et al. 1996; Chen et al. 1997; Koren et al. 1999; Ek et al. 2003). It has been incorporated into HWRf since the 2015 implementation. The model was developed jointly by NCAR and NCEP, and is a unified code for research and operational purposes.

The Noah LSM has one canopy layer and utilizes the following prognostic variables: soil moisture and temperature in the soil layers, water stored in the canopy, and snow stored on the ground. It is a 4-layer soil temperature and moisture model with canopy moisture and snow-cover prediction. The layer thicknesses of 10, 30, 60, and 100 cm (i.e., a total of 2 meters) from the top down are chosen to simulate the daily, weekly, and seasonal evolution of soil moisture (Chen and Dudhia 2001). The model includes the root zone, evapotranspiration, soil drainage, and runoff; taking into account vegetation categories, monthly vegetation fraction, and soil texture. The scheme provides sensible and latent heat fluxes to the boundary-layer scheme. The Noah LSM additionally predicts soil ice, and fractional snow-cover effects, has an improved urban treatment (Liu et. al. 2006), and considers surface emissivity properties. More information about the Noah LSM can be found in Chen and Dudhia (2001) and Mitchell (2005).

#### 4.6 Planetary boundary-layer parameterization

The PBL parameterization is responsible for vertical sub-grid-scale fluxes due to eddy transports in the whole atmospheric column, not just the boundary layer. Thus, when a PBL scheme is activated, no explicit vertical diffusion is activated, under the assumption that the PBL scheme will handle this process. Horizontal and vertical mixing are therefore treated independently. The surface fluxes are provided by the surface layer and land-surface schemes. The PBL schemes determine the flux profiles within the well mixed boundary layer and the stable layer, and thus provide atmospheric tendencies of temperature, moisture (including clouds), and horizontal momentum in the entire atmospheric column. Most PBL schemes consider dry mixing, but can also include saturation effects in the vertical stability that determine the mixing. Conceptually, it is important to keep in mind that PBL parameterization may both complement and conflict with the cumulus parameterization. PBL schemes are 1-D, and assume that there is a clear scale separation between sub-grid eddies and resolved eddies. This assumption will become less clear at grid sizes below a few hundred meters, where boundary-layer eddies may begin to be resolved, and in these situations, the scheme should be replaced by a fully 3-D local sub-grid turbulence scheme. HWRF uses a non-local vertical mixing scheme based on the GFS PBL option with several modifications to fit hurricane and environmental conditions

##### ***The HWRF PBL scheme***

Since 2016, HWRF uses the non-local Hybrid Eddy-Diffusivity Mass-Flux (Hybrid EDMF), where the non-local mixing under convective conditions is represented by a mass-flux approach. This is the same scheme used in the NCEP GFS. This is in contrast with earlier versions of HWRF, in which a counter-gradient flux parameterization was used.

The overall diffusive tendency of a variable  $C$  can therefore be expressed as

$$\frac{\partial C}{\partial t} = \frac{\partial}{\partial z} \left[ K_c \left( \frac{\partial C}{\partial z} \right) - M (C_u - \bar{C}) \right] \quad (4.6.1),$$

where  $C_u$  is  $C$  in the updraft,  $\bar{C}$  is  $C$  in the environment,  $M$  is the updraft mass flux,

$\frac{\partial}{\partial z} K_c \left( \frac{\partial C}{\partial z} \right)$  is the local flux and  $M(C_u - \bar{C})$  is the nonlocal flux. Details on the derivation of the nonlocal flux can found in Han et al. (2016), while details of the local flux calculation, evolved from Hong and Pan (1996) and Troen and Mahrt (1986), and similar to the Yonsei University (YSU) and Medium-Range Forecast (MRF) schemes, can be found below.

The local scheme is a first-order vertical diffusion parameterization that uses the surface bulk-Richardson approach to iteratively estimate the PBL height starting from the ground upward. The PBL height ( $h$ ) depends on the virtual temperature profile between the surface and the PBL top, on the wind speed at the PBL top and on the critical Richardson number ( $Ric$ ), and is given by

$$h = Ric \frac{\theta_{vg} U^2(h)}{g (\theta_v(h) - \theta_s)} \quad (4.6.2),$$

where,  $\theta_{vg}$  and  $\theta_v(h)$  are the virtual potential temperature at surface and at the PBL top, respectively,  $U(h)$  is wind speed at the PBL top, and  $\theta_s$  is the surface potential temperature. Once the PBL height is determined, a preliminary profile of the eddy diffusivity is specified as a cubic function of the PBL height. This value is then refined by matching it with the surface-layer fluxes. The process above determines the local component of the momentum eddy diffusivity, which can be expressed as

$$K_m(z) = kZ \left( \frac{u_*}{F_m} \right) \left[ \alpha \left( 1 - \frac{z}{h} \right)^2 \right], \quad (4.6.3),$$

where  $\mathbf{K}$  is the von Karman constant ( $=0.4$ ),  $u_*$  is the surface frictional velocity,  $Z$  is the height above ground,  $\Phi_m$  is a wind-profile function evaluated at the top of the surface layer, and  $\alpha$  is a parameter that controls the eddy diffusivity magnitude (Gopalakrishnan et al. 2013).

In HWRF, the  $\alpha$  is used to control the eddy diffusivity in the PBL. Up until the 2014 implementation,  $\alpha$  only depended on the grid spacing. Since the 2015 HWRF implementation,  $\alpha$  has been made variable as part of a new approach to cap the eddy diffusivity based on the wind speed over the hurricane area. An effective  $\alpha$  is computed based on diagnosed eddy diffusivity of momentum ( $K_m$ ) at a single level ( $Z_s = 500$  m) and then applied through the entire PBL within that model column. At each level,  $K_m$  cannot exceed  $K_m(\text{cap}) = WS/0.6$ , where  $WS$  is wind speed at  $Z_s$ . The model first diagnoses  $K_m$  with  $\alpha = 1$ , denoted as  $K_m(\text{guess})$ . Then  $K_m(\text{guess})$  is compared with  $K_m(\text{cap})$ . If the PBL height is lower than  $Z_s$  or if  $K_m(\text{guess})$  is smaller than  $K_m(\text{cap})$ ,  $\alpha$  is set to be 1. In this case, the vertical profile of  $K_m$  is unmodified. Otherwise,  $\alpha$  is set to  $K_m(\text{cap})/K_m(\text{guess})$ , and used throughout the entire PBL at that column. The operational variable  $\alpha$  scheme is triggered by setting variable  $\alpha$  to  $-1$  in the WRF namelist. Details for the approach are outlined in Bu (2015).

The height-independent  $\alpha$  in used up until the 2015 HWRF implementation causes a discontinuity of  $K_m$  at the top of the surface layer. In the 2016 implementation,  $\alpha$  was modified to vary with height, decreasing from 1 at the top of the surface layer to  $K_m$  (cap)/  $K_m$  (guess) at the height of the maximum  $K_m$ , then increasing to 1 near the PBL top. Some tests suggest that this update can improve intensity forecasts and low-level wind profiles, especially in the eyewall area (Wang et al. 2018).

It should be noted that the Hybrid EDMF scheme also considers dissipative heating, the heat produced by molecular friction of air at high wind speeds (Bister and Emanuel 1998). This contribution is controlled by the WRF namelist parameter *disheat*.

The Hybrid EDMF scheme can be contrasted with local schemes such as the MYJ PBL scheme used in North America Mesoscale Model (NAM), which is an option for experimental, unsupported, versions of HWRF. This parameterization of turbulence in the PBL and in the free atmosphere (Janjic 1990a,b, 1996, 2002) represents a nonsingular implementation of the Mellor-Yamada Level 2.5 turbulence closure model (Mellor and Yamada 1982) through the full range of atmospheric turbulent regimes. In this implementation, an upper limit is imposed on the master length scale. This upper limit depends on the TKE as well as the buoyancy and shear of the driving flow. In the unstable range, the functional form of the upper limit is derived from the requirement that the TKE production be nonsingular in the case of growing turbulence. In the stable range, the upper limit is derived from the requirement that the ratio of the variance of the vertical velocity deviation and TKE cannot be smaller than that corresponding to the regime of vanishing turbulence. The TKE production/dissipation differential equation is solved iteratively. The empirical constants used in the original Mellor-Yamada scheme have been revised (Janjic 1996, 2002). Note that the TKE in the MYJ PBL scheme has a direct connection to the horizontal diffusion formulation in the NNM-E grid and NMM-B grid dynamic cores, but this has been turned off in HWRF.

#### 4.7 Atmospheric radiation parameterization

Radiation schemes provide atmospheric heating due to radiative flux divergence and surface downward longwave and shortwave radiation for the ground-heat budget. Longwave radiation includes infrared or thermal radiation absorbed and emitted by gases and surfaces. Upward longwave radiative flux from the ground is determined by the surface emissivity that in turn depends upon land-use type, as well as the ground (skin) temperature. Shortwave radiation includes visible and surrounding wavelengths that make up the solar spectrum. Hence, the only source is the sun, but processes include absorption, reflection, and scattering in the atmosphere and at the surface. For shortwave radiation, the upward flux is the reflection due to surface albedo. Within the atmosphere, radiation responds to model-predicted cloud and water-vapor distributions, as well as specified carbon dioxide, ozone, and (optionally) trace gas concentrations and particulates. All the radiation schemes in WRF currently are columnar (1-D) schemes, so each column is treated independently, and the fluxes correspond to those in infinite horizontally uniform planes, which is a good approximation if the vertical thickness of the model layers is much less than the horizontal grid length. This assumption would become less accurate at high horizontal resolution, especially where there is sloping topography. Atmospheric radiation codes are quite complex and computationally

intensive and are therefore often invoked at less frequent intervals than the rest of the model physics. The HWRF radiation parameterization used in operations is the RRTMG scheme described below. Compared with extra-tropical phenomena, hurricanes are less dependent on radiative fluxes except when migrating out of the tropics and/or progressing over land. Radiation-cloud interactions may be more important than direct radiative impacts, except during extra-tropical transition.

### ***The RRTMG longwave and shortwave radiation schemes***

The 2016 HWRF implementation was modified to use the RRTMG (Iacono et al. 2008) longwave and shortwave codes, which are modified from RRTM (Mlawer et al. 1997) to provide improved computational efficiency and a treatment of subgrid-scale cloud variability. Absorption and emission from water vapor, carbon dioxide, ozone, methane, nitrous oxide, oxygen, nitrogen, and the halocarbons are included in the longwave, while the radiative effects of water vapor, carbon dioxide, ozone, oxygen and methane are included in the shortwave. The ozone profile and mixing ratios of CO<sub>2</sub> and other trace gases are specified. Calculations are made over 16 spectral bands in the longwave and 14 spectral bands in the shortwave. Flux integration in the longwave uses a single standard diffusivity angle, and a two-stream adding-doubling method is used for multiple scattering in the shortwave. Scattering in the longwave is not included. Longwave aerosol absorption and shortwave aerosol extinction (absorption + scattering) are available, though these features are not used in the current HWRF implementation. The specified cloud fraction is used to represent the vertical overlap of clouds using the Monte Carlo Independent Column Approximation (McICA [Barker et al. 2007; Pincus et al. 2003]), which is a statistical technique for representing the sub-grid variability of clouds within the radiative transfer calculations. As a result, the temperature tendencies are sensitive to the resolved and sub-grid model cloud fields. Cloud optical properties are calculated for each spectral band following Hu and Stamnes (1993) for water clouds and Fu et al. (1998) for ice clouds. The cloud optical depth, single-scattering albedo, and asymmetry parameter are parameterized as a function of the cloud-particle equivalent radius and the liquid and ice-water paths.

For horizontal grid resolutions that do not fully resolve clouds, specification of the cloud fraction requires selecting an assumption for how partial cloudiness overlaps in the vertical within a grid box, which can have a significant impact on radiative transfer. Available cloud overlap assumptions in RRTMG include random (no correlation between disassociated, separated cloud layers), maximum (fully overlapping in the vertical within adjacent, multiple cloud layers), and a blend of these two, called maximum-random (MR), which has been the default cloud overlap assumption in RRTMG. The MR method presumes maximum overlap in adjacent cloud layers and random overlap among separated groups of cloud layers. Recently, RRTMG was modified to use an exponential (EXP) cloud overlap method, which presumes that the vertical correlation of cloud layers transitions inverse exponentially from maximum to random with increasing layer thickness and vertical distance. The exponential method is in effect a compromise between the more extreme random and MR assumptions. The EXP approach defines the exponential transition,  $\alpha$ , of cloud overlap from maximum to random across vertical layers as a function of layer thickness,  $\Delta z$ , and a decorrelation length,  $Z_0$ :

$$\alpha = e^{-(\Delta z/Z_0)}. \quad (4.7.1)$$

High decorrelation lengths or small vertical distances ( $\alpha \rightarrow 1$ ) infer a greater tendency toward maximum overlap, and low decorrelation lengths or greater vertical distances ( $\alpha \rightarrow 0$ ) infer a greater tendency toward random overlap. Finely spaced vertical layering implies smaller values of  $\Delta z$ , higher  $\alpha$ , and maximum overlap, while coarser vertical spacing corresponds to higher values of  $\Delta z$ , lower  $\alpha$ , and more random vertical correlation. Through multiple adjacent cloudy layers, the vertical correlation becomes increasingly random as the exponential transition is applied at each layer. Relative to the MR approach, EXP generally increases the effective total cloud cover as represented in the radiation calculation in the presence of fractional cloudiness. The 2018 HWRF implementation has adopted EXP cloud overlap using a constant decorrelation length of 2.5 km as a representative tropical value consistent with radar cloud measurements (Pincus et al. 2005).

The use of subgrid cloud fields is motivated by recent research revealing that numerical weather prediction (NWP) models generally predict insufficient cloud coverage when compared with observations. This low bias in cloud amount has been observed in numerous global circulation models (Ma et al. 2014) as well as regional/mesoscale models such as the German COSMO model (Eikenberg et al. 2015) and the WRF model (Cintineo et al. 2014). One consistency across the various models is the under-prediction of relatively low-altitude clouds such as boundary-layer clouds, but also clouds that attain heights in the mid-troposphere. To mitigate this low bias, HWRF uses a cloud-fraction scheme developed by G. Thompson, based on Sundqvist et al. (1989). The scheme uses a critical relative humidity (RH) threshold (hereafter called *RH-crit*) for the onset of non-zero cloud amount along with increasing cloud fraction as RH increases. As in Mocko and Cotton (1995), different *RH-crit* over oceanic versus land-model points are applied, because it is quite likely that near ocean surfaces, the RH will typically be very high. Therefore, a higher *RH-crit* over ocean is required when compared with land to reduce the likelihood that most ocean surfaces would be considered partly cloudy.

One difference in the adoption of the Mocko and Cotton (1995) implementation is an explicit dependence on model grid spacing,  $\Delta x$ . This was deemed necessary to consider future variable-mesh grid frameworks and computational advances in which the model grid spacing is likely to be near or below 1.0 km. It is logical to assume that high-resolution numerical models will create better cloud forecasts due to resolving explicitly those vertical motions responsible for creating clouds. Therefore, at first order, a higher *RH-crit* should be required as model  $\Delta x$  decreases. An initial functional form of the *RH-crit* versus  $\Delta x$  relationship, is shown in Fig. 4-4. The Mocko and Cotton (1995) implementation was used to formulate initial values of *RH-crit* because the HWRF grid spacing is similar to the one used in their study. Also shown in Fig. 4-4 is the diagnosed fractional cloudiness as a function of model RH, based on the given starting value of *RH-crit* as an example showing the Sundqvist et al. (1989) formulation.

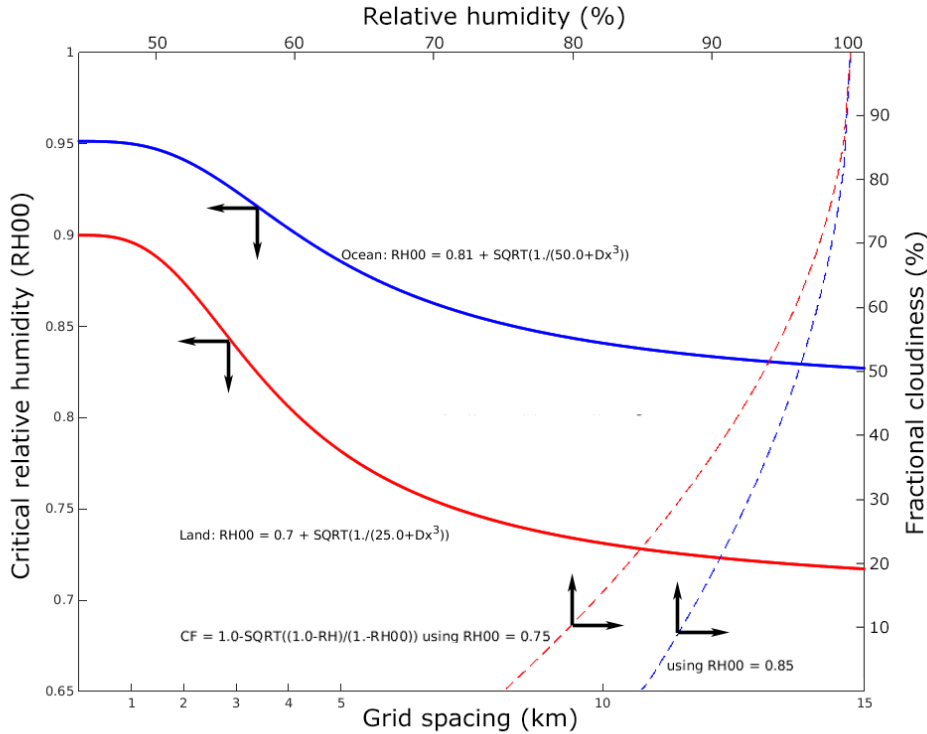


Figure 4-4: RH-crit as a function of model grid spacing,  $\Delta x$  (solid lines; bottom/left axes) for land (red curve) and ocean (blue curve) points. Fractional cloudiness as a function RH (dashed lines; top/right axes) following Sundqvist et al. (1989). The starting value on the ordinate represents RH-crit.

As implemented within WRF, the RRTMG shortwave and longwave radiation codes require more than just a simple cloud fraction. Within a grid volume of a certain cloud fraction, RRTMG requires the liquid and/or ice water contents (LWC and IWC, respectively) and radiative effective particle size to compute the radiative fluxes. The assignment of LWC and IWC adds complexity to the cloud-fraction scheme. First of all, if a model grid volume already contains a minimum cloud-water (ice) mixing ratio of  $1 \times 10^{-6} \text{ kg kg}^{-1}$  ( $1 \times 10^{-7} \text{ kg kg}^{-1}$ ), then the grid volume is declared 100% cloudy. For all other grid volumes and in the most basic manner possible, a simple plume of rising air within continuous layers of diagnosed cloud fraction greater than 1% is sought. First, the bottom ( $k_{bot}$ ) and top ( $k_{top}$ ) of such cloud layers is found, then the layer maximum LWC (or IWC) is determined from the difference of water-vapor mixing ratio ( $Q$ ) as the absolute value of  $(Q_{k_{bot}} - Q_{k_{top}})$ . Next, the total LWC is divided into each layer as a fraction of the total cloud depth multiplied by an entrainment factor. The 2017 updates included adjustments to the relative humidity threshold methodology to address solar radiation biases.

For additional information and results from the partial cloudiness scheme, readers are referred to [http://www.dtcenter.org/eval/hwrf\\_hdrf\\_hdgf/HFIP\\_GT2014Dec17.pdf](http://www.dtcenter.org/eval/hwrf_hdrf_hdgf/HFIP_GT2014Dec17.pdf).

## 4.8 Physics interactions

While the model physics parameterizations are categorized in a modular way, it should be noted that there are many interactions between them via the model-state variables (potential temperature, moisture, wind, etc.) and their tendencies, via the surface fluxes. The surface physics, while not explicitly producing tendencies of atmospheric-state variables, is responsible for updating the land-state variables as well as updating fluxes for ocean coupling. Note also that the microphysics does not output tendencies, but updates the atmospheric state at the end of the model time step. The radiation, cumulus parameterization, and PBL schemes all output tendencies, but the tendencies are not added until later in the solver, so the order of call is not important. Moreover, the physics schemes do not have to be called at the same frequency as each other or at the basic model dynamic time step. When lower frequencies are used, their tendencies are kept constant between calls or time interpolated between the calling intervals. The land-surface and ocean models, excluding simple ones, also require rainfall from the microphysics and cumulus schemes. The boundary-layer scheme is necessarily invoked after the land-surface scheme because it requires the heat and moisture fluxes.

## 5. DESIGN OF MOVING NEST

HWRF, which uses the NMM dynamic core under the WRF model software framework, supports moving, one- or two-way interactive nests. While WRF-NMM can handle multiple stationary domains at the same nest level, and/or multiple nest levels (telescoping) with two-way interaction, the HWRF configuration employs a single domain per nest level. In HWRF, the 4.5- and 1.5-km domains follow the storm, while the 13.5-km parent domain is stationary. When more than one tropical storm is observed, more than one independent run of HWRF is launched so that every storm has its own high-resolution moving nest.

In the current implementation of the nesting algorithm, only horizontal refinement is available; that is, there is no vertical nesting option. The nested grids adopt the ratio 1:3 to refine the resolution of the coarse and fine grids based on an Arakawa-E grid staggering structure. Correspondingly, the time-step ratio between the coarse and fine grids is 1:3 as well. The mass points of the nested grids are aligned with those of the coarser grids in which they are nested. The coincidence of grid points between the parent and nested domains simplifies remapping and feedback procedures. The design of constructing nesting grids also conforms to the parallel strategy within the WRF advanced software framework (Michalakes et al. 2004) and enhances code portability of the model for various applications. HWRF inherits time-controlling capabilities of WRF-NMM, which means that HWRF can initialize and terminate the integration of nested grids at any time during the model run. In the operational implementation, nested grids are present throughout the entire forecast.

### 5.1 Grid Structure

As described in the NMM scientific documentation (Janjic et al. 2010), the WRF-NMM is a non-hydrostatic model formulated on a rotated latitude-longitude, Arakawa E-grid, with a vertical-pressure sigma hybrid vertical coordinate system. The rotated latitude-longitude coordinate is transformed in such a way that the coordinate origin is located in the center of the parent domain, and the x-axis and y-axis are aligned with the new coordinate equator and the prime meridian through the domain center, respectively (Figure 5-1). To address multi-scale forecasting, a horizontal mesh refinement capability was developed for this system. All interpolations from the parent to the nested domain are achieved on a rotated latitude-longitude E-grid. The nested domain can be freely moved anywhere within the grid points of the parent domain, yet the nested domain rotated latitude-longitude lines will always coincide with the rotated latitude-longitude lines on the mass grid of the parent domain at fixed parent-to-nest grid-size ratio 1:3.

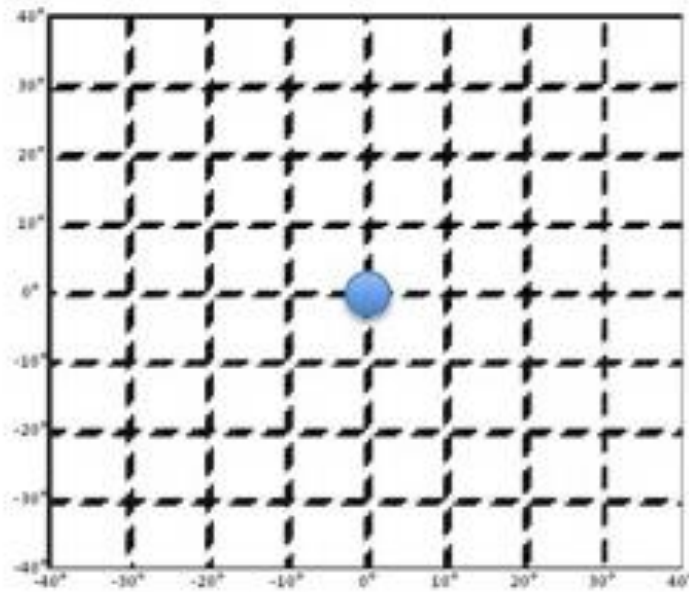


Figure 5-1: Schematic rotated latitude and longitude grid. The blue dot is the rotated latitude-longitude coordinate origin. The origin is the cross point of the new coordinate equator and zero meridian, and can be located anywhere on Earth.

Terrestrial properties provide important external forcing on the dynamics and thermodynamics of any numerical model. The impact of terrain on TC track, intensity and structure has been recognized in many previous studies (e.g., Lin 2007). Therefore, careful treatment of static terrestrial conditions such as terrain and land-sea contrast is necessary to contain contamination and possible computational noise in the modeled solution due to improper adjustment from coarse- to fine-resolution terrestrial information.

The terrain treatment in the HWRF system is tailored to the TC problem by using high-resolution topography to account for the detailed topographic effects of the complex islands and landmasses. Before the forecast starts, WPS is used to interpolate topography information from prescribed high-resolution-terrain datasets to the required grid resolution over the entire parent domain to ensure the movable nests always have access to high-resolution topography. For example, in a typical operational forecast at 13.5 km with two center-aligned movable nests at 4.5- and 1.5-km resolutions, terrestrial data are generated at all three resolutions for the entire static parent domain shown in Figure 5-2. This way, the model always has access to high-resolution topographic information when the grid moves during the forecast.

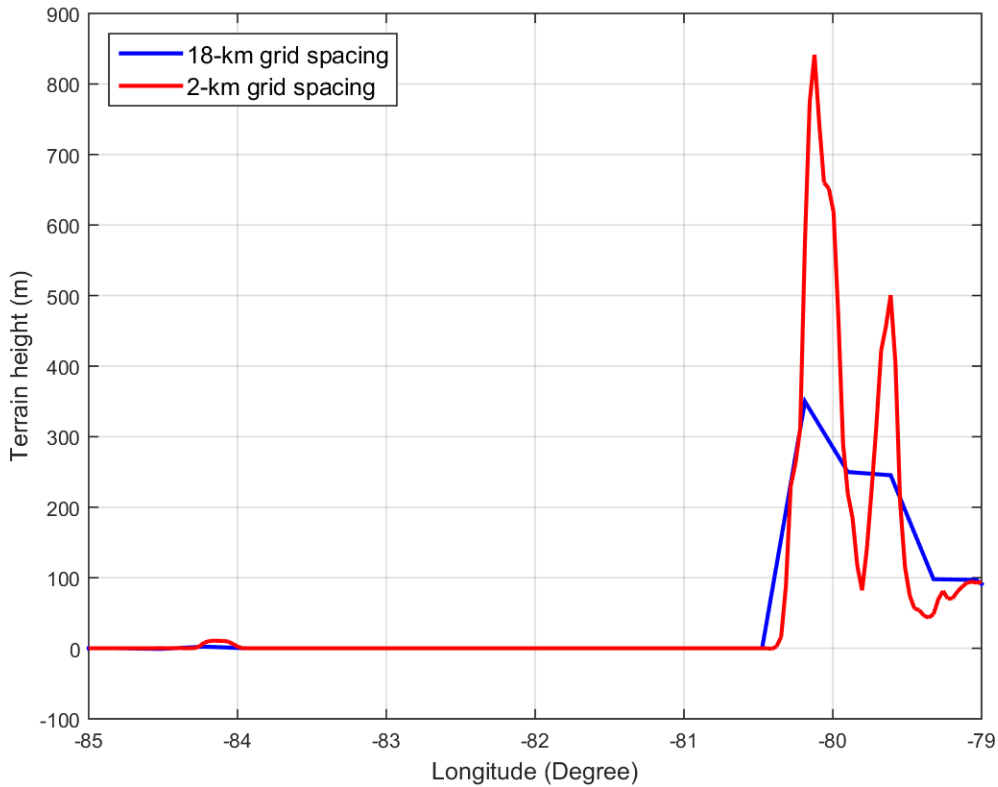


Figure 5-2: An example of model topography differences for domains at 18- (blue) and 2-km (red) resolutions, respectively. The cross section is along latitude  $\sim 22^\circ\text{N}$ , between longitudes  $\sim 85^\circ\text{W}$  and  $\sim 79^\circ\text{W}$ . The biggest differences are in the mountainous areas of Eastern Cuba.

Topography is the only static dataset generated in high resolution. For pragmatic considerations, all other static terrestrial information for nests is downscaled from the coarser-resolution parent domain.

The terrain within the nest is smoothed before being used. The grids are smoothed through a four-point weighted average with a special treatment at the four corners. Points in the inner part of the domain are smoothed using

$$\overline{t_{hr}}(i,j) = 0.25 * [t_{hr}(i+1,j) + t_{hr}(i,j+1) + t_{hr}(i-1,j) + t_{hr}(i,j-1)],$$

where  $t_{hr}$  is the high-resolution terrain in a nest. Points along the boundary use a modified equation. For example, for the western boundary, the equation is

$$\overline{t_{hr}}(1,j) = 0.125 * [t_{hr}(1,j-1) + t_{hr}(1,j+1)] + 0.75 * t_{hr}(1,j).$$

The smoothed topography in the corner points also follows a modified formula. For example, the average terrain at the southwest point is given by

$$\overline{t_{hr}}(1,1) = 0.75 * t_{hr}(1,1) + 0.125 * t_{hr}(2,2) + 0.0625 * [t_{hr}(2,1) + t_{hr}(1,2)]$$

Certainly, the high-resolution terrain conforms to land-sea mask binary categories, that is, only land points have terrain assigned.

## 5.2 Moving Nest Algorithm

The use of enhanced resolution only in the TC region is a pragmatic solution commonly adopted in the tropical cyclone NWP community to reduce computational costs. For the TC to be consistently contained in the highest-resolution domain, that domain has to move to follow the storm.

The nest motion for tropical cyclones and tropical depressions is currently based on the GFDL Vortex Tracker (Section 6). Nine fields are calculated, with pressure-level fields interpolated by log(P). Vorticity, MSLP, and geopotential height fields are smoothed using an iterative smoother. Then their extremes, known as *fix locations* are calculated:

- 1-3. Minimum wind speed at 10 m, 850 hPa and 700 hPa
- 4-6. Maximum 10-m vorticity at 10 m, 850 hPa and 700 hPa
- 7. Minimum MSLP
- 8-9. Minimum geopotential height at 700 and 850 hPa

Once all nine fix locations have been calculated, the standard deviation of the fix locations with respect to the domain center is calculated. Fix locations far from the domain center are discarded. The maximum allowed distance differs by parameter and varies with time, based on prior fix-to-center standard deviations. Once the final set of parameters is chosen, the mean fix location is used as the storm center. The standard deviation of the fix parameters is stored for discarding fix parameters at later time steps. Lastly, the nest is moved if the storm location is more than two parent gridpoints in the Y (rotated north-south) direction or more than one parent gridpoint in the X (rotated east-west) direction. One should note that, while at every time step numerous fields are passed between domains before and after the grid motion, the interpolation and hydrostatic mass balancing are also applied in the region of the leading edge of the moving nest as described in the next subsection.

## 5.3 Fine Grid Initialization

The generation of initial conditions for the HWRF parent domain was discussed in Chapter 2. For the nests, all variables, except topography, are initialized using the corresponding variables downscaled from the parent grid during the integration. To alleviate potential problems related to singularities due to high-resolution terrestrial information in the nested domain, the initialization of the land variables, such as land-sea mask, soil temperature, and vegetation type, are exclusively initialized through a nearest-neighbor approach at the initial time step and the leading edge during the integration.

To obtain the temperature, geopotential, and moisture fields for the nest initialization, hydrostatic mass balance is applied. The first step is to horizontally interpolate coarser-

resolution data to the fine-resolution grid. The second step is to apply the high-resolution terrain and the geopotential to determine the surface pressure on the nest. The pressure values in the nest hybrid surfaces are then calculated. The final step is to compute the geopotential, temperature, and moisture fields on the nest hybrid surfaces using linear interpolation in a logarithm of pressure vertical coordinate. The schematic procedure is illustrated in Figure 5-3. The zonal and meridional components of the wind are obtained by first performing a horizontal interpolation from the parent to the nest grid points using a bi-linear algorithm over the diamond-shaped area indicated in blue in Figure 5-4. The wind components are then linearly interpolated in the vertical from the parent hybrid surfaces onto the nest hybrid surfaces. Note that, while the hybrid levels of the nest and parent in sigma space coincide, the nest and the parent do not have the same levels in pressure or height space. This is due to the differing topography, and consequently different surface pressure between the nest and the parent.

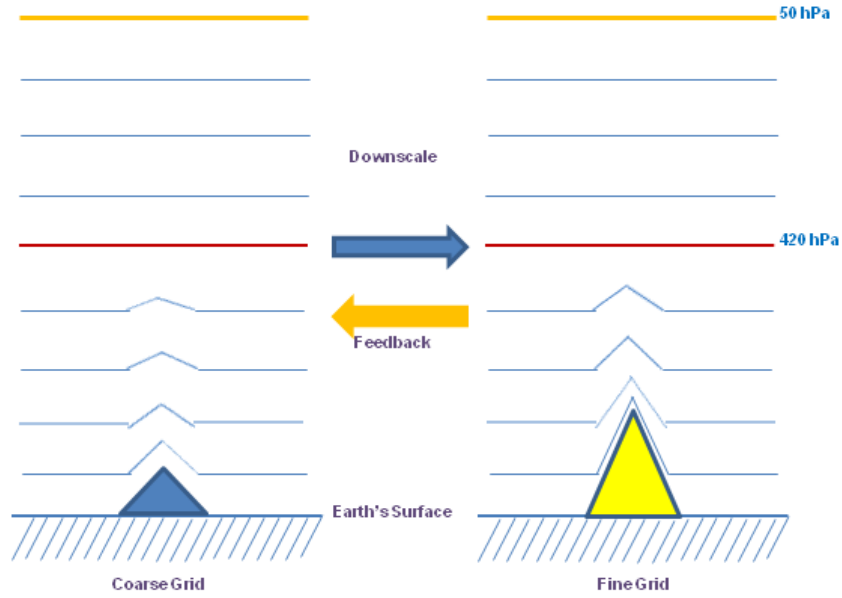


Figure 5-3: An illustration of the vertical interpolation process and mass balance. Hydrostatic balance is assumed during the interpolation process.

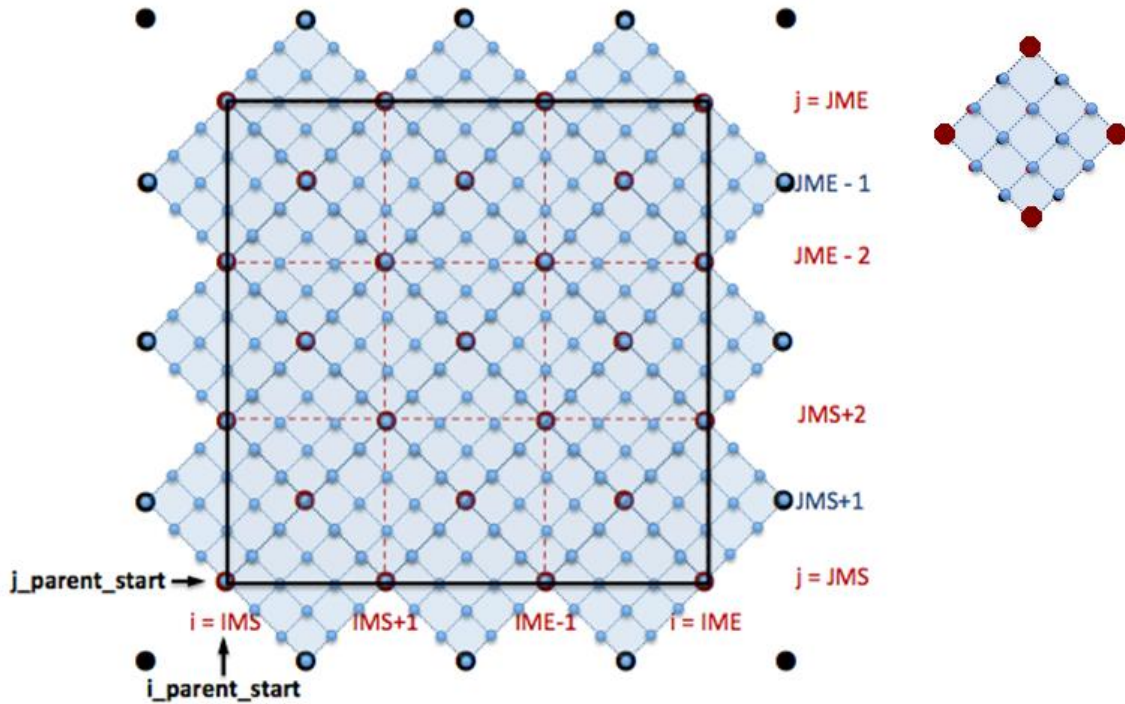


Figure 5-4: The schematic E-grid refinement - dot points represent mass grid. Big and small dots represent coarse- and fine-resolution grid points, respectively. The black square represents the nest domain. The

diamond square on the right side is composed of four big-dot points representing the bilinear interpolation control points.

## 5.4 Lateral Boundary Conditions

Figure 5-5 illustrates a sample E-grid structure, in which the outermost rows and columns of the nest are termed the prescribed interface, and the third rows and columns are termed the dynamic interface. The prescribed interface is forced to be identical to the parent domain interpolated to the nest grid points. The dynamic interface is obtained from internal computations within the nest. The second rows and columns are a blend of the first and third rows/columns. Because the prescribed interface is well separated from the dynamic interface in the E-grid structure, nested boundaries can be updated at every time step of the parent domain exactly the same way as the parent domain boundary is updated from the external data source. This is done with bi-linear interpolation and extrapolation using the same mass adjustment procedure previously described. This approach is simple, and yet produces an effective way of updating the interface without excessive distortion or noise.

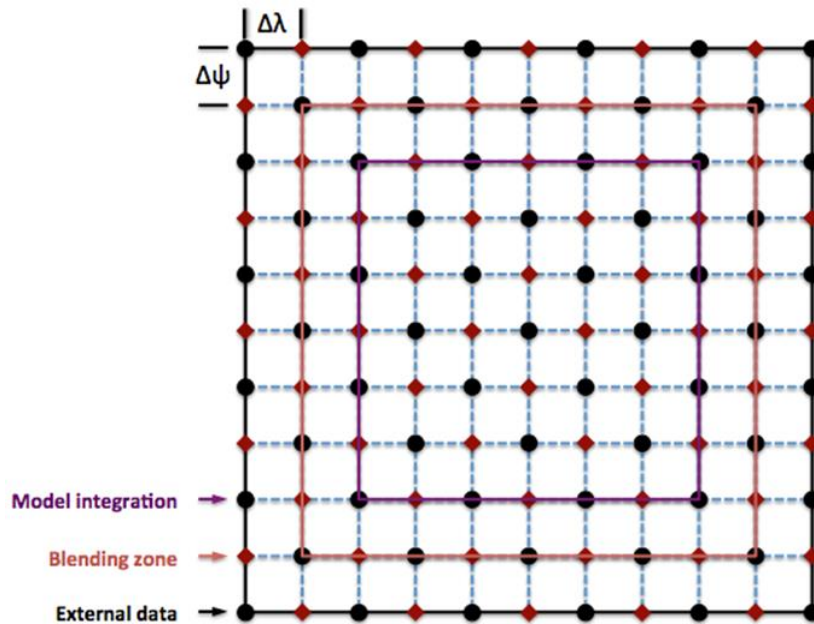


Figure 5-5: Lateral boundary-condition buffer zone - the outmost column and row are prescribed by external data from either a global model or regional model. The blending zone is an average of data prescribed by global or regional models and those predicted in the HWRF domain. Model integration is the solution predicted by HWRF.  $\Delta\psi$  and  $\Delta\lambda$  are the grid increment in the rotated latitude-longitude coordinate.

The feedback from a fine-resolution domain to a coarse-resolution domain is an important process for a hurricane forecast model. It reflects the multiple-scale physical interactions in the hurricane environment. This is done using the same mass adjustment procedure previously described, except that the parent pressure is retained. In addition, rather than horizontal interpolation, horizontal averaging is used: the nine fine-grid points surrounding a coarser-resolution grid point are used before the mass adjustment process. Furthermore, feedback is done with a 0.5 weighting factor, replacing the coarse-grid data

with the average of the coarse and fine-grid data. Also, to avoid a nest directly modifying its boundary conditions, a one-parent grid-point row and column buffer region is maintained in the parent domain that does not receive data from the nest. In cases with multiple nests at the same level, nests feed back to the parent in numerical order (grid 1, then 2, then 3, etc.) Each has 50% feedback, resulting in a smoothed average in the parent, in regions where nest domains overlap.

## 6. USE OF THE GFDL VORTEX TRACKER

### 6.1 Introduction

Numerical modeling has become an increasingly important component of hurricane research and operational hurricane forecasting. Advances in modeling techniques, as well as the fundamental understanding of tropical cyclones dynamics, have enabled numerical simulations of hurricanes to become more realistic and contribute to more skillful hurricane forecasts. One critical element of assessing the performance of a hurricane model is the evaluation of its track and intensity forecasts. These forecasts are typically represented in the form of text data output either directly from the forecast model or in a post-processing step of the modeling system using an external vortex tracker. This document provides a description of the GFDL vortex tracker (Marchok 2002), which operates as a standalone tracking system in a post-processing step. The GFDL vortex tracker has been used as an operational tool by NCEP since 1998, and it is flexible enough to operate on a variety of regional and global models of varying resolutions. The tracker will also detect new cyclones the model develops during the course of a forecast.

#### 6.1.1 Purpose of the vortex tracker

A numerical model produces an abundance of digital output, with up to hundreds of variables on dozens of vertical levels, including variables for mass, momentum, density, moisture, and various surface- and free-atmosphere fluxes. While a tropical cyclone's center is defined by its low-level circulation features, a comparison of synoptic plots of various low-level parameters will often reveal a range of variability in a storm's center position. This variability can be critical for storms that are either just forming or are undergoing extratropical transition. Figure 6-1 illustrates this variability for a case of Tropical Storm Debby (2006) in an analysis from the NCEP GFS. At this time, Debby was a weak, 40-kt tropical storm, and the variability in the center location fixes indicates that the model had not yet developed a coherent vertical structure for the storm.

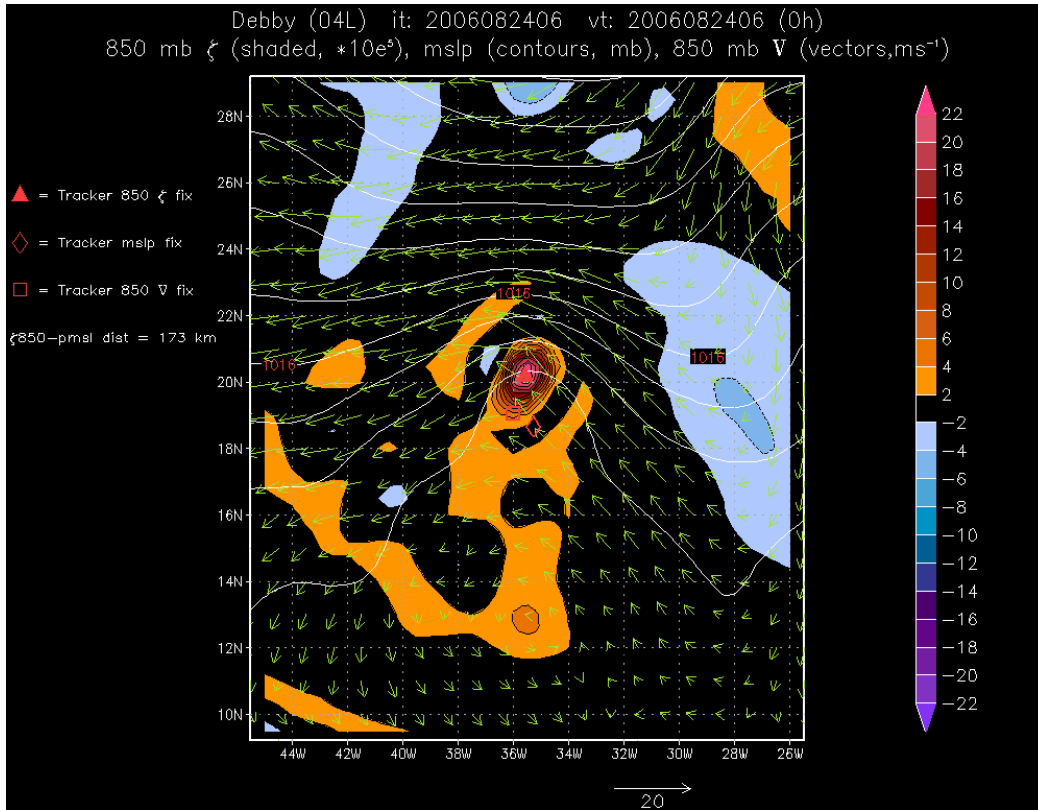


Figure 6-1: Mean sea-level pressure (contours, mb), 850-mb relative vorticity (shaded,  $\text{s}^{-1} \times 10^5$ ) and 850-mb winds (vectors,  $\text{ms}^{-1}$ ) from the NCEP GFS analysis for Tropical Storm Debby, valid at 06 UTC 24 August 2006. The triangle, diamond, and square symbols indicate the locations at which the GFDL vortex tracker identified the center position fix for each of the three parameters. The notation to the left of the synoptic plot indicates that the distance between the 850-mb vorticity center and the mslp center is 173 km.

A vortex tracker is used to analyze the data objectively and provide a best estimate of the storm's central position, then tracks the storm throughout the duration of the forecast. Depending on the complexity of the tracker, additional metrics can be reported, including the minimum sea-level pressure, the maximum near-surface wind speed, the radii of gale-storm- and hurricane-force winds in each storm quadrant, parameters that describe the thermodynamic structure or phase of the storm, and parameters that detail the spatial distribution of the near-surface winds. This document will focus primarily on the basic functioning of the tracker and its reporting of the track, intensity, and wind-radii parameters.

### 6.1.2 Key issues in the design of a vortex tracker

When designing a tracking scheme, some fundamental questions must be considered. The first question is deciding on the method used to locate a maximum or a minimum within some field of values. Numerous methods can be used for this purpose. The simplest method is to scan the field of values and find the maximum or minimum at one of the model output grid points. However, this method restricts the maximum or minimum value located at one of the fixed data points on the grid. For many grids, especially those with coarser resolutions, the actual maximum or minimum value may fall between grid points. The data can be interpolated to a finer resolution, but interpolation is a procedure

that can be both expensive and complicated to generalize for use with both regional and global grids over a range of resolutions. Furthermore, a problem can still remain after interpolation whereby the tracking scheme needs to choose between two or more candidate points with identical values located close to one another. The GFDL vortex tracker uses a scheme that employs a Barnes analysis of the data values at each candidate grid point to provide a field of values that have been weight-averaged based on distance from the candidate grid point. This technique, which is described in detail in Section 5.2, mitigates the issues described above.

The second issue is striking the balance between making the scheme sensitive enough so that it can detect and track weaker storms, and making it overly sensitive such that it continues tracking for too long and tracks weak remnants that no longer resemble a cyclone, or worse, it jumps to a stronger passing storm and begins tracking that storm instead. Several checks have been included in the GFDL vortex tracker, some with thresholds that can be adjusted either in the source code or via namelists as inputs to the executable. These checks are described in Section 6.2.

The remainder of this section describes in detail the design and functioning of the GFDL vortex tracker. Section 6.2 focuses on the design of the tracker and the input data it uses. Section 6.3 presents a discussion of the various low-level parameters that are tracked and how they are combined to produce a mean position fix at a given lead time. Section 6.4 describes how the maximum wind and the various wind radii in each storm quadrant are obtained. Section 6.5 describes diagnostic analyses performed by the tracker to evaluate the thermodynamic phase of a model cyclone. Section 6.6 details use of the tracker for the purpose of detecting and tracking new, model-generated storms, and Section 6.7 provides details regarding the tracker output.

## 6.2 Design of the tracking system

### 6.2.1 Input data requirements

The GFDL vortex tracker can operate in two different modes. In the basic mode, it will perform tracking only for storms that have been numbered by a Regional Specialized Meteorological Center (RSMC), such as NHC. It also operates in a mode whereby it detects and tracks new storms generated by a model during the course of a forecast.

#### 6.2.1.1 *Synoptic forecast data*

The tracker requires input data to be in either NetCDF or Gridded Binary (GRIB) format, with both GRIB1 and GRIB2 formats being acceptable. The data must be on a cylindrical equidistant, latitude-longitude (lat/lon) grid. While the dx and dy grid increments need to be uniform across the grid, dx does not need to be equal to dy. The data should be ordered so that j and i increment from north to south and east to west, respectively, such that point (1,1) is in the far northwestern part of the grid, and point (imax,jmax) is in the far southeastern part of the grid. Data files with values incrementing from south to north can be flipped prior to execution of the tracker using an external GRIB or NetCDF file manipulation tool.

The data files do not need to have regular spacing for the lead-time intervals. This flexibility allows the user to obtain tracker output using output model data at more frequent time intervals around a particular time of interest. The tracker reads in a list of forecast lead times from a text file the user prepares. For GRIB data, the tracker has the ability to process files that have the lead times identified in the Product Definition Section (PDS) of the GRIB header as either hours or minutes. The choice for using either minutes or hours is passed to the program via a namelist option. Regardless of which choice is made, those lead times must be listed in the user input text file as integers in units of minutes (the exact required format can be seen in the read statement in subroutine read\_fhours), and then the tracker can manipulate the hours and minutes as needed.

#### 6.2.1.2 Realtime observed storm data

The tracker works by searching for a vortex initially at a location specified by a 1-line text record produced by either NHC for storms in the Atlantic, eastern Pacific and central Pacific basins, or by the JTWC for storms in other global basins. This record contains just the basic, vital information necessary to define the observed location and intensity parameters of the storm, and it is commonly referred to as the “TC vitals” record. An example TC vitals record is shown here for Katrina for the observed time of 00Z 29 August 2005:

```
NHC 12L KATRINA 20050829 0000 272N 0891W 335 046 0904 1006 0649 72 037
0371 0334 0278 0334 D 0204 0185 0139 0185 72 410N 815W 0167 0167 0093 0167
```

The critical information needed from the TC vitals record for tracking is the Automated Tropical Cyclone Forecast (ATCF) ID number for the storm (12L), the observed time (20050829 0000), and the location of the storm, indicated here as “272N 0891W,” or 27.2° North, 89.1° West. For this example, the tracker would start looking for Katrina in the 00 UTC 29 August 2005 analysis for a given model at 27.2° North, 89.1° West, and if it finds a storm near there, it records its position, writes out a record in a specific text format that contains critical storm forecast location and intensity forecast data, and then makes a guess for the next position at the next forecast lead time to begin searching again.

#### 6.2.2 The search algorithm

To locate a maximum or minimum value for a given variable, a single-pass Barnes analysis (Barnes 1964, 1973) is employed at grid points in an array centered initially around the NHC-observed position of the storm. This position is referred to as the initial guess position. For a given variable  $F$ , the Barnes analysis,  $B$ , at a given point,  $g$ , in this array is given as:

$$B(g) = \frac{\sum_{n=1}^N w_n F(n)}{\sum_{n=1}^N w_n} \quad (6.2.1.2.1)$$

where  $w$  is the weighting function defined by:

$$w = e^{-(d_n^2/r_e^2)} \quad (6.2.1.2.2)$$

and where  $d_n$  is the distance from a data point,  $n$ , to the grid point,  $g$ , and  $r_e$  is the e-folding radius. The e-folding radius is the distance at which the weighting drops off to a value of  $1/e$ , and this value can be adjusted. Currently, most regional and global model grids fall into a category with output file grid spacing between about  $0.1^\circ$  and  $1.25^\circ$ , and for those we use a value of  $r_e = 75$  km. For any models with resolutions coarser than  $1.25^\circ$ , a value of  $r_e = 150$  km is used. For model grids with a grid spacing finer than  $0.1^\circ$ , a value of  $r_e = 60$  km is used. The overriding idea is to find a balance whereby enough points are included in the averaging process to produce a weighted average from the Barnes function that is representative of the surrounding region, but not so many points that finer scale details are smoothed out so much that it's difficult to differentiate the average value at one grid point from that of an adjacent point.

The Barnes analysis provides an array of Gaussian weighted-average data values surrounding the initial guess position. The center is defined as the point at which this function is maximized (e.g., Northern Hemisphere relative vorticity) or minimized (e.g., geopotential height, sea-level pressure, Southern Hemisphere relative vorticity), depending on the parameter being analyzed.

As described above, the center location for a given parameter will often lie between grid points, and this is especially true for coarser resolution grids. To produce a position fix with enough precision such that center fixes for variables with center locations between grid points can be properly represented, it may be necessary to perform several iterations of the Barnes analysis. In the initial iteration, a Barnes analysis grid is defined with grid spacing equal to that of the input data grid, and the weighted values from the Barnes analysis are assigned to the points on the analysis grid. The difference between the input data grid and the Barnes analysis grid is the following: the input data grid has specific  $(i,j)$  locations that are fixed, while for the analysis grid an array of points can be defined, relative to the guess position in latitude-longitude space. After a position fix is returned from the first iteration of the Barnes analysis, an additional iteration of the Barnes analysis can be performed, this time centering the analysis grid on the position fix from the first iteration. In this second iteration, the search area for the center location is restricted, and the grid spacing of the Barnes analysis grid is halved to produce a finer-resolution position fix. This process can be iterated a number of times and the Barnes analysis run over increasingly finer-resolution analysis grids to fix the center position more precisely. In the current version of the tracker, a variable ("nhalf") is specified to indicate that five additional iterations of the Barnes analysis should be done for grids with spacing greater than  $0.2^\circ$ . For example, for a grid with original grid spacing of  $1^\circ$ , halving the analysis grid spacing five times would result in a final analysis grid spacing of approximately 3 km, which is already beyond the one-tenth of a degree precision contained in the observational Best Track dataset. For data grids with original spacing of less than  $0.2^\circ$ , such as the operational HWRF, only two additional Barnes iterations are performed, and for grids with spacing less than  $0.05^\circ$ , only one additional Barnes iteration is performed.

### 6.2.3 Tracking a vortex throughout a forecast

A tracking algorithm ultimately produces a set of points that contains information on the forecast location of the storm at discrete time intervals. The challenge is ensuring that the

points that are connected from one lead time to the next do, in fact, represent points from the same storm and that there is no “contamination” introduced by accidentally having the tracker follow a different storm. This challenge becomes greater for model output with longer intervals between lead times. For example, it is far easier to know with certainty that a nearby storm is the same storm that has been tracked up to this time if the last position fix only occurred 30 minutes ago in model time as opposed to having occurred 12 hours ago. This section deals with how the model handles the tracking of a vortex from one lead time to the next and what types of quality control checks are applied.

#### 6.2.3.1 *Tracking from one lead time to the next*

If the tracker finds a storm at a given lead time, it has to know where to begin searching for the storm at the next lead time. There are two methods the tracker employs for this purpose. In the first method, a Barnes analysis is performed for the location at which the tracker position fix was made for the current lead time. This analysis is performed for the winds at 500, 700, and 850 hPa using a relatively large e-folding radius of 500 km. The idea here is to create smoothed fields that represent the mean fields at each level. The mean values from these three levels are then averaged together to give a wind vector that can be used as a deep-layer mean steering wind. A hypothetical parcel is then advected according to the deep-layer mean wind for the length of the lead time interval to produce a dynamically generated guess position for the next lead time.

The second method uses a basic linear extrapolation of the current model storm motion. For all lead times after the initial time, this method can be employed by using the previous and current forecast position fixes. For the initial time, there is obviously no previous position from the current model forecast to use for an extrapolation; however, this extrapolation method is still used at the initial time by instead using the observed storm motion vector information read from the TC vitals record. However, this method of using the storm-motion vector is not as reliable because the observed storm-motion vector may differ from the model storm motion vector.

The estimates from these two methods are averaged together to produce a position guess from which the tracker will begin searching for the storm at the next lead time. Both of these methods use estimates that are static in time, and therefore, error is introduced in the position guesses. Those errors obviously grow larger with increasingly longer lead-time intervals. However, it is important to note that these are only position guesses, and the tracker will allow a position fix to be made up to a certain distance from that position guess. Experience in operations has shown the combination of these two methods to be a reliable means of providing position guesses for successive lead times, even for model output with lead-time intervals of 12 h. Cases that should be scrutinized with this method include those in which the storm begins to rapidly accelerate or decelerate, and those in which the storm is rapidly recurving into the westerlies.

#### 6.2.3.2 *Quality control checks*

Once the tracker has produced a position fix at a given lead time, a number of checks are performed to help ensure that the system the tracker found not only a storm, but is the

same storm that has been tracked to this point in the forecast. As a first check, the sea-level pressures of the points surrounding the position fix are evaluated to determine whether a pressure gradient exceeding a particular threshold exists and is sloped in the correct direction. This criterion is fairly easy for a storm to satisfy because the requirement is that it be only satisfied for any azimuthal direction, and not that it be satisfied by a mean gradient value. The threshold can be set by the user in the run script by specifying its value in the “mslpthresh” variable. In the current version of the tracker, the mslpthresh variable is set to a value of 0.0015 mb/km, which is equivalent to 0.5 mb per 333 km.

A second check involves the wind circulation at 850 mb. The tangential component of the wind ( $V_T$ ) is computed for all points within 225 km of the position fix, and the mean  $V_T$  must be cyclonic and exceed a user-specified threshold. This threshold is also set in the run script by specifying the value of the v850thresh variable. This variable has units of  $m\ s^{-1}$  and is set by the user as a namelist option. A default value commonly used in the operational version of the tracker is  $1.5\ m\ s^{-1}$ .

For a third check, the distance between the position fixes for two parameters is evaluated to ensure it does not exceed a specified distance. As will be described below in Section 6.3, the tracker finds the center location of several different low-level parameters. If the distance between the mean sea-level pressure (mslp) and 850-mb relative vorticity position fixes becomes too large, it could indicate either that the storm is becoming too disorganized due to dissipation or that it is undergoing extratropical transition and the tracker may have incorrectly “locked on” to a different storm nearby having one of those two parameter fixes. In either case, if that distance is exceeded, the tracker will stop tracking for this particular storm. That distance threshold is specified by the variable “max\_mslp\_850” in subroutine tracker, and it is currently set at 323 km for most models, including HWRF.

One final check is made of the model storm’s translation speed. The current and previous position fixes are used to calculate the average speed that the model storm must have traveled to reach the current position, and if that speed exceeds a certain threshold, then the tracker assumes that it has incorrectly locked on to a different storm nearby and tracking is stopped for this storm. That speed is defined by the “maxspeed\_tc” variable in module error\_parms and is currently set to a value of 60 kt. It should be noted that during the evaluation of model forecasts from the HFIP High-Resolution Hurricane (HRH) test in 2008, this storm translation speed check was responsible for erroneously stopping a number of forecasts. The problem arose for cases in which a very weak model storm center reformed after only 30 minutes of model time at a location more than 100 km away. While such behavior is reasonable for a very weak, but developing storm, to exhibit, this large shifting of storm position over a very short time period resulted in a computed translation speed that exceeded the threshold. If necessary, this problem can be circumvented by setting the maxspeed\_tc threshold to an unrealistically high value.

It is important to emphasize that while these last two quality-control checks will occasionally terminate tracking for storms that are undergoing extratropical transition (ET), the intended purpose is not to stop tracking when ET is taking place. To the contrary, the goal is to continue tracking to provide track and intensity guidance for as

long as possible in the forecast. Furthermore, the model forecast of the onset of ET may not correspond at all of the observed storm's behavior. These last two checks are instead meant to stop tracking if the tracker detects that it may have erroneously begun to track a different, nearby storm.

The current version of the tracker includes code that will report on the thermodynamic phase of the system, that is, whether the system is tropical, extratropical, etc. This code requires input data that have been interpolated to certain levels and/or averaged, as described in Section 6.5.

### 6.3 Parameters used for tracking

The GFDL vortex tracker produces position fixes for several low-level parameters. The position fixes are then averaged together to produce the mean position fix reported for that lead time. This section describes the various parameters and how the tracker combines them to produce the mean position fix.

#### 6.3.1 Description of the tracking variables

Up to twelve parameters are available for tracking. All of these parameters are drawn from the lower levels of the troposphere. The parameters include relative vorticity at 10 m and at 850 and 700 mb; mslp; geopotential height at 850 and 700 mb; wind circulation at 10 m and at 850 and 700 mb; and geopotential thickness for the 500-850, 200-500 and 200-850 mb layers. Beginning with the version of the tracker released in 2017, users will have the option of selecting which parameters to use for tracking from a namelist.

Most models, including HWRF, output absolute vorticity. For those models, the tracker will subtract out the Coriolis component at each grid point. If vorticity is not included in the input data file, the tracker will compute it using the u- and v-components of the wind that have been read in. The Barnes analysis is performed for each of these six parameters. If the Barnes analysis returns a location for the maximum or minimum that is within a specified distance threshold, then that parameter's location fix is saved for later use in computing the average position fix. If it is not within that distance threshold, the position fix for that parameter is discarded for that lead time. If one or more of these parameters is missing from the input data file, the tracker simply continues tracking using the limited subset of available parameters.

The distance thresholds are defined initially by the "err\_gfs\_init" and "err\_reg\_init" parameters in module error\_parms. Values for this initial error parameter vary according to the resolution of the data grid, with finer resolution grids assigned a threshold of 275 km and coarser resolution global grids assigned a less restrictive 300-km threshold. For lead times after the initial time, this distance threshold is defined as a function of the standard deviation in the positions of the parameter location fixes including up to the three previous lead times. For example, for very intense, steady-state storms that have strong vertical coherence in their structure, the various parameter fixes are likely to be located closely together. In these cases, the distance threshold defined by the standard deviation of the parameter fixes will be small, as will be the tolerance for outliers in the parameter fixes. For weak systems, or for storms undergoing ET, the vertical structure has less coherence and often wider variance in the location of the parameter fixes. In

these cases, the higher distance thresholds defined by the larger standard deviation allow more flexibility in accepting parameter fixes that are not located close to the guess position for a given lead time.

In versions of the tracker prior to the 2017 release, additional searches were performed for the minimum in wind speed at the center of the storm at 10 m and at 850 and 700 mb. The intent was to locate the center of circulation, and this worked well years ago for coarse resolution data, e.g., data with grids having a horizontal resolution coarser than  $0.5^\circ$ . However, the use of this minimum wind speed began to experience problems with the advent of models with very fine horizontal resolution and more realistic storm structure, such as HWRF's 2-km resolution data. In some cases, particularly those with intense but small storms, the tracker would locate a minimum in wind speed that was actually outside the circulation of the storm. To correct this issue, the search for the minimum wind speed was replaced with an algorithm to locate the maximum in the wind circulation. It is important for the proper functioning of the tracker to have an accurate fix for the center of circulation because the strength of the circulation at 850 mb is one of the criteria used in determining whether to continue tracking.

### 6.3.2 Computation of the mean position fix

Once the center fixes have been completed for all of the various parameters, a mean location fix is computed for the storm. A parameter is only included in the mean computation if its location is found within the distance threshold, as described in Section 6.3.1. The mean computation is performed in two steps. In the first step, a mean position is computed using all available parameters found within the distance threshold. In the second step, the distance of each parameter fix from that mean position is computed, as is the standard deviation of the parameter fixes. The mean position fix is then recalculated using a Gaussian weighting predicated by the standard deviation of the position fixes. The goal here is to minimize the impact of an outlier parameter fix by weighting the mean towards the larger cluster of parameter-position fixes.

## 6.4 Intensity and wind radii parameters

The vortex tracker must also report on forecast data related to intensity and wind structure. For the mslp, the value reported during the search for the storm center was a smoothed value derived from the Barnes analysis. A separate call was made to subroutine `fix_latlon_to_ij` to return the minimum gridpoint value of mslp near the storm center. The tracker then analyzes the near-surface wind data (10 m for HWRF and most other models) to report on the value of the maximum wind speed. For high-resolution grids (spacing  $< 0.25^\circ$ ), the search for the maximum wind is restricted to points within 200 km of the center. For coarser resolution grids with spacing up to  $1.25^\circ$ , the search can extend out to 300 km from the center. The value of the radius of maximum winds is obtained at the same time.

As large storms such as Katrina, Isabel, and Sandy have demonstrated, it is important to obtain guidance on the structure of the wind field in addition to the forecast maximum wind value. The tracker provides basic reporting of the forecast near-surface wind structure by obtaining the radii of 34-, 50-, and 64-kt winds in each quadrant of the storm.

The values reported indicate the maximum distance at which winds of these magnitudes were found anywhere in the quadrant, and are not necessarily aligned along any particular azimuth within a quadrant. The values are then output in the standard ATCF text format, as described in Section 6.7.

The large wind field of Hurricane Sandy (2012) exposed an issue with the algorithm that diagnoses the wind radii in the model output. The maximum radius from which to search for the radii of 34-kt winds (R34) had been set at 650 km. The observed R34 values in Sandy easily exceeded 650 km, as did the forecast R34 values from many of the operational models. Simply increasing the maximum search radius by several hundred km is not advisable, because that could lead to the reporting of erroneous radii values for smaller storms. Instead, an iterative technique has been employed in which the maximum search radius is initially set to a small value (500 km), and if the diagnosed R34 value is returned as either 500 km or very close to it, then the search is done again, but after increasing the maximum search radius by 50 km. This process may reiterate up to a maximum search radius of 1,050 km. Results indicated much more reasonable results from a sample of storms with widely varying R34 values, including large storms such as Hurricane Sandy.

## 6.5 Thermodynamic phase parameters

The fundamental tracking algorithm used by the tracker is designed such that it will analyze data to find the central location of a cyclone and report on its intensity. However, additional diagnostics can be performed after the tracker has located the cyclone center at a given lead time to determine whether a model cyclone is tropical or not. This section describes two different methods used in the tracker for diagnosing the thermodynamic phase of a cyclone.

The first method used by the tracker to diagnose the thermodynamic phase of cyclones is the cyclone phase space methodology developed by Hart (2003). The tracker ingests the average temperature from 300 to 500 hPa and the geopotential height every 50 hPa from 300 to 900 hPa. Three critical parameters are diagnosed: (1) the storm motion-relative, left-to-right asymmetry in the lower-troposphere (900-600 hPa); (2) warm- / cold-core structure in the lower troposphere (900-600 hPa) as diagnosed by assessing the vertical variation of the near-storm isobaric height gradient; and (3) warm- / cold-core structure in the upper troposphere (600-300 hPa), as diagnosed by assessing the vertical variation of the near-storm isobaric height gradient.

The second method for diagnosing the thermodynamic phase employs a more basic algorithm, loosely based on Vitart et al. (1997), to determine the existence of a temperature anomaly in the 300-500-hPa layer near the cyclone center. The tracker ingests a field containing mean temperatures in the 300-500 hPa layer and it runs the tracking algorithm to locate the maximum temperature in that mean layer. It then calls a routine to analyze the 300-500-hPa mean temperature field to determine whether a closed contour exists in the temperature field surrounding the maximum temperature. The value of the contour interval checked is set by the user as an input parameter in the script, and it has been found empirically that setting the contour interval to 1°K provides an acceptable threshold.

Analyses for both the cyclone phase space and for the simple check of the warm-core return values are output in a modified ATCF format, described in Section 5.7. It is important to note that the calculations and determinations made by these thermodynamic diagnostics are provided as auxiliary information and will not affect how a cyclone is tracked or how long the cyclone is tracked. In particular, the tracker will not cease tracking a cyclone if the values returned from these thermodynamic-phase diagnostics return values that indicate the storm has either begun or completed transition to an extratropical or subtropical cyclone. It is up to the user to interpret the tracking and phase diagnostic results that are reported in the ATCF output.

## 6.6 Detecting genesis and tracking new storms

As the forecasting community becomes increasingly interested in forecasts of cyclones at longer lead times, there also exists increased interest in predicting cyclone genesis. In recent years, global models have shown the ability to develop cyclones without the aid of synthetic bogusing techniques. The tracker algorithm has been updated to detect genesis in numerical models and track any such new disturbances the models develop.

Creating an algorithm for detecting new storms generated by a model presents a somewhat more complex problem than for tracking already-existing storms. For a storm that is already being tracked by an RSMC, an observed location is provided by that RSMC and the tracker begins searching near that location for what is known to be a coherent circulation in nature and is assumed to be a coherent circulation in the model. In the case of detecting genesis, no assumptions are made about the coherence of any circulation, and extra steps must be taken to ensure that any systems detected by the tracker in the model output are not only cyclones, but tropical cyclones. It is important to note, however, that these additional checks to determine whether the system is of a tropical nature are only done if the `trkrinfo%type` is set to “`tcgen`” in the input namelist file. If `trkrinfo%type` is instead set to “`midlat`,” then the tracker only uses `mslp` for locating the storm center, and no checks are performed to differentiate tropical from non-tropical cyclones.

The tracker begins by searching at the forecast initial time for any RSMC-numbered systems that may have been listed on the input TC vitals record (if provided). This step ensures these systems are accurately identified by the tracker and are not mistakenly detected and identified as new cyclones by the tracker. For each RSMC-numbered cyclone found, a routine named `check_closed_contour` is called. The primary purpose of this routine is to determine whether at least one closed contour in the `mslp` field exists surrounding the cyclone. An additional, but crucial function of this routine is to continue searching outwards from the center of the low to find all closed contours surrounding the low. All grid points contained within these closed contours are then masked out so that when the tracker searches for additional lows at the same lead time, masked-out points will not be detected again as a new low.

After finding any RSMC-numbered systems and masking out grid points surrounding those systems, the tracker performs a two-step searching procedure over the remainder of the model domain. First, a search is performed to identify any candidate cyclones, and then a detailed tracking scan is performed to more accurately determine the location and

intensity of the candidate cyclones found in the first search and to perform additional diagnostics.

In the first search to identify candidate cyclones, a looping procedure is conducted in which the grid points are scanned to find the lowest mslp on the grid. For the grid point with the lowest mslp found, a check determines whether there is at least one closed mslp contour surrounding the system. If so, then this grid point is saved into an array as a candidate low to be analyzed in the second step. The looping procedure then continues searching for grid points with the next lowest mslp, and this procedure continues until the lowest pressure found is greater than one half standard deviation above the mean mslp on the grid.

In the second step, the candidate cyclones found in the first step are analyzed more critically using the full tracking algorithm outlined in Section 6.2 to more accurately determine the location and intensity of the cyclone. The quality-control checks outlined above in Section 6.2.3.2 are employed to ensure the system being tracked has the fundamental characteristics of a cyclone and are used as input to determine whether to continue tracking for a given system.

Some of the more critical checks for newly detected storms include the check for a closed mslp contour as well as the check to determine whether the azimuthally averaged 850-mb winds are cyclonic and exceed a user-specified threshold. However, due to the fact that incipient, developing cyclones have structures that are often weak and vacillating in intensity, some leniency is used when applying these checks from one lead time to the next for the purpose of genesis tracking. In particular, for the closed mslp contour check, the checks must return a positive result for at least 50% of the lead times over the past 24-h period to continue tracking. For the 850-mb circulation check, the threshold is a positive result returned for at least 75% of the lead times. The threshold is more rigorous for the 850-mb circulation check than for the mslp check because 850 mb is above the boundary layer and the storm circulation there is generally more inertially stable and less prone to high-frequency fluctuations in intensity than the surface layer.

Additional diagnostics can be performed at this time to determine the thermodynamic phase of the system, as described in Section 6.5. Results from the thermodynamic phase diagnostics are included in the output, as described below in Section 6.7, but are not used in any algorithms for determining whether to continue tracking a system.

## 6.7 Tracker output

The motivation behind making the GFDL tracker operational in 1998 was to provide track and intensity guidance from forecasts for a number of models in as short a time as possible. One of the requirements was that the output data be in the same text ATCF format as used by NHC. The two primary output files from the tracker include one file in ATCF format and another in a format just slightly modified from the ATCF format. The advantage of using the ATCF format is that user forecasts can easily be compared with those from some of the operational modeling centers.

### 6.7.1 Description of the ATCF format

The ATCF format contains information on the ocean basin, the storm number, the model ID, the initial date, the forecast hour, and various track, intensity, and wind radii guidance. Up to three ATCF records can be output for each lead time. A sample segment with some ATCF records from a GFDL hurricane model forecast for Hurricane Emilia (2012) is shown here:

```
EP, 05, 2012071000, 03, GFDL, 000, 131N, 1118W, 98, 951, XX, 34, NEQ, 0080,
0072, 0057, 0078, 0, 0, 17, 0, 0, , 0, , 0, 0, , , , , 0, 0, 0, 0,
THERMO PARAMS, -9999, -9999, -9999, Y, 10, DT, -999
```

```
EP, 05, 2012071000, 03, GFDL, 000, 131N, 1118W, 98, 951, XX, 50, NEQ, 0056,
0047, 0036, 0053, 0, 0, 17, 0, 0, , 0, , 0, 0, , , , , 0, 0, 0, 0,
THERMO PARAMS, -9999, -9999, -9999, Y, 10, DT, -999
```

```
EP, 05, 2012071000, 03, GFDL, 000, 131N, 1118W, 98, 951, XX, 64, NEQ, 0040,
0028, 0017, 0037, 0, 0, 17, 0, 0, , 0, , 0, 0, , , , , 0, 0, 0, 0,
THERMO PARAMS, -9999, -9999, -9999, Y, 10, DT, -999
```

```
EP, 05, 2012071000, 03, GFDL, 006, 134N, 1129W, 80, 963, XX, 34, NEQ, 0100,
0084, 0057, 0088, 0, 0, 34, 0, 0, , 0, , 0, 0, , , , , 0, 0, 0, 0,
THERMO PARAMS, 45, 1405, 1742, Y, 10, DT, -999
```

```
EP, 05, 2012071000, 03, GFDL, 006, 134N, 1129W, 80, 963, XX, 50, NEQ, 0061,
0053, 0027, 0058, 0, 0, 34, 0, 0, , 0, , 0, 0, , , , , 0, 0, 0, 0,
THERMO PARAMS, 45, 1405, 1742, Y, 10, DT, -999
```

```
EP, 05, 2012071000, 03, GFDL, 006, 134N, 1129W, 80, 963, XX, 64, NEQ, 0045,
0034, 0008, 0038, 0, 0, 34, 0, 0, , 0, , 0, 0, , , , , 0, 0, 0, 0,
THERMO PARAMS, 45, 1405, 1742, Y, 10, DT, -999
```

```
EP, 05, 2012071000, 03, GFDL, 012, 137N, 1137W, 78, 964, XX, 34, NEQ, 0084,
0071, 0068, 0078, 0, 0, 22, 0, 0, , 0, , 0, 0, , , , , 0, 0, 0, 0,
THERMO PARAMS, 26, 1609, 1879, Y, 10, DT, -999
```

```
EP, 05, 2012071000, 03, GFDL, 012, 137N, 1137W, 78, 964, XX, 50, NEQ, 0054,
0048, 0041, 0050, 0, 0, 22, 0, 0, , 0, , 0, 0, , , , , 0, 0, 0, 0,
THERMO PARAMS, 26, 1609, 1879, Y, 10, DT, -999
```

```
EP, 05, 2012071000, 03, GFDL, 012, 137N, 1137W, 78, 964, XX, 64, NEQ, 0039,
0033, 0023, 0036, 0, 0, 22, 0, 0, , 0, , 0, 0, , , , , 0, 0, 0, 0,
THERMO PARAMS, 26, 1609, 1879, Y, 10, DT, -999
```

The first two columns represent the ATCF ID, here indicating that Emilia was the fifth named storm in the eastern Pacific basin in 2012. The next column indicates the initial time for this forecast. The “03” is constant and simply indicates that this record contains model forecast data. After the column with the model ID is the column indicating the lead time for each forecast record. Note that in the current version of the tracker, the frequency at which ATCF data are written out is defined by the `atcfreq` variable defined in the `namelist`. That variable should be specified as an integer \* 100. The next two columns indicate the latitude and longitude, respectively, in degrees multiplied by 10. The next two columns, respectively, are the maximum wind speed, in kt, and the minimum sea-level pressure, in mb. The “XX” is a placeholder for character strings that indicate whether the storm is a depression, tropical storm, hurricane, subtropical storm, and so on. Currently, the storm-type character string is only used for the observed storm data in the NHC Best Track dataset.

The next six columns are used to report wind radii forecast data. The first entry in those six columns is an identifier indicating whether this record contains radii for the 34-, 50-, or 64-kt wind thresholds. The “NEQ” indicates the four radii values that follow will begin in the northeast quadrant. Each subsequent value is derived from the next quadrant clockwise. The radii are listed in units of nautical miles (n mi). If the tracker has detected winds of at least 50 kt in the 10-m wind data, then an additional record is output for this lead time. This record is identical to the first record, with the exception that the wind radii threshold identifier is “50” instead of “34,” and the radii values are included for the 50-kt threshold. Similarly, if the tracker has detected winds of at least 64 kt at this lead time, then an additional record is output containing those 64-kt wind radii. For any of these thresholds for which at least one quadrant has wind value exceedance, if one or more of the remaining quadrants does not have exceedance, then for each of those quadrants a value of zero is output.

After the four quadrant values for wind radii, there are two placeholders that are always zero, and then a column that indicates the radius of maximum winds, in n mi. This value is reported using the location of the maximum wind speed the tracker returned.

After the radius of maximum winds, there is a series of commas and zeroes, followed by a user-defined section of the ATCF record, which is used here to output the values for the thermodynamic diagnostics. The first three values listed after the “THERMO PARAMS” character string are the three cyclone-phase space parameters, and all values shown have been multiplied by a factor of 10. The values are listed in the following order: (1) Parameter B (left-right thickness asymmetry); (2) Thermal-wind (warm/cold core) value for lower troposphere (900-600 mb); and (3) Thermal-wind value for upper troposphere (600-300 mb). Note that for the first lead time listed for a given model storm, the cyclone-phase space parameters will always have undefined values of -9999. This is because the calculation of Parameter B is highly sensitive to the direction of motion, and for the first lead time listed for a storm, it is not possible to know which direction the model storm is heading.

After the cyclone-phase space parameters a character indicates whether the simple check for a warm core in the 300-500-hPa layer was successful. The possible values listed here are “Y,” “N,” and a “U” for “undetermined” if, for any reason, the warm-core check

couldn't be performed. The next parameter indicates the value of the contour interval used in performing the check for the warm core in the 300-500-hPa layer (that value is listed with a magnitude of \*10). The last two parameters are currently unsupported and will always be listed as "DT, -999."

### 6.7.2 Output file with a modified ATCF format for sub-hourly lead times

As described in Section 6.2, the tracker can process lead times that are not in regular intervals. In addition, it can process sub-hourly lead times (e.g., tracking using data every 20 minutes). However, the standard ATCF format described in Section 6.7.1 cannot represent non-integral, sub-hourly lead times. To mitigate this problem, a separate file with a format just slightly modified from the standard ATCF format is also output. The only difference is that the lead time in the modified format contains five digits instead of three and is represented as the lead time \* 100. For example, a lead time of 34 hours, 15 minutes would be 34.25 hours and would be represented in the modified ATCF format as 03425.

To summarize, the modified ATCF format can be output at every lead time, including sub-hourly, non-integral lead times. The standard ATCF format was only designed to handle integral, hourly lead times. Therefore, if a user is processing code that has data at sub-hourly temporal resolutions, a standard ATCF formatted record will not be output for those sub-hourly times.

### 6.7.3 Output file with a modified ATCF format for use with genesis tracking features

A modified ATCF format is required for the output from genesis tracking runs. In these runs, there will often be a mixture of RSMC-numbered storms as well as new storms that the model develops on its own. For the model-generated storms, a new storm-naming convention is devised to account for the fact that these storms have no previous, set identity as assigned by an RSMC, and the identifiers for the storms must be unique.

Shown below is an example of output from a genesis tracking run for the NCEP GFS model, which is the output for one model-generated storm as well as for one RSMC-numbered storm, 99L. The first column is reserved for either the ATCF basin ID (AL, EP, WP, etc.) for an RSMC-numbered storm or an identifier to indicate the type of tracking run being performed ("TG" = tropical cyclogenesis). The second column will either be the ATCF ID for an RSMC-numbered storm (e.g., 99L) or a tracker-defined cyclone ID for this particular tracking run. This cyclone ID is unique to this particular tracking run, and it should not be used for counting storms throughout a season, because the number may be repeated in the next run of the tracker, but for a different storm.

The third column contains the unique identifier for the storm. Using 2012080100\_F150\_138N\_0805W\_FOF from the first record below as an example, the first element indicates the initial date/time group for this particular tracker run, the "F150" indicates the forecast hour when this particular storm was first detected in the model, and the next two elements ("138N\_0805W") indicate the latitude and longitude where the storm was first detected. The "FOF" indicates that this storm was "Found On the Fly" by

the tracker in a genesis tracking run, as opposed to being tracked from the initial time as an RSMC-numbered storm.

After the unique identifier in the third column, the format is the same as the standard ATCF described above in Section 6.7.1, through and including the wind radii values. After the wind radii values, the next two parameters listed are the pressure and radius (n mi) of the last closed isobar (1009 and 196 in the first record below), and that is followed by the radius of maximum winds (n mi).

The next four values listed are the thermodynamic diagnostics. The first three values are the three cyclone-phase space parameters; note that all values shown have been multiplied by a factor of 10. The values are listed in the following order: (1) Parameter B (left-right thickness asymmetry); (2) Thermal wind (warm/cold core) value for lower troposphere (900-600 mb); and (3) Thermal wind value for upper troposphere (600-300 mb). Refer to Hart (2003) for interpretation of the three cyclone phase space parameters.

Following the cyclone phase space parameters is a character that indicates whether the simple check for a warm core in the 300-500-mb layer was successful. The possible values are “Y,” “N,” and a “U” for “undetermined” if, for any reason, the warm-core check couldn’t be performed.

After the warm-core flag, the next two values (259 and 31 in record 1) indicate the direction and translation speed of storm motion, with the speed listed in  $\text{m s}^{-1} \times 10$ . The final four values (112, 144, 69, 89) are, respectively, the values for the mean relative vorticity returned from the tracker at 850 mb, the gridpoint maximum vorticity near the cyclone center at 850 mb, the mean relative vorticity returned from the tracker at 700 mb, and the gridpoint maximum vorticity near the cyclone center at 700 mb. All vorticity values have been scaled by  $1\text{E}6$ .

```
TG, 0048, 2012080100_F150_138N_0805W_FOF, 2012080100, 03, GFSO, 150,
138N, 805W, 18, 1008, XX, 34, NEQ, 0000, 0000, 0000, 0000, 1009,
196, 80, -999, -9999, -9999, N, 259, 31, 112, 144, 69,
89
```

```
TG, 0048, 2012080100_F150_138N_0805W_FOF, 2012080100, 03, GFSO, 156,
134N, 813W, 17, 1008, XX, 34, NEQ, 0000, 0000, 0000, 0000, 1010,
251, 98, 19, 106, -89, N, 252, 36, 126, 168, 67,
93
```

```
TG, 0048, 2012080100_F150_138N_0805W_FOF, 2012080100, 03, GFSO, 162,
134N, 816W, 17, 1008, XX, 34, NEQ, 0000, 0000, 0000, 0000, -999, -
999, 55, -11, 162, 77, N, 266, 17, 110, 150, 70,
91
```

```
TG, 0048, 2012080100_F150_138N_0805W_FOF, 2012080100, 03, GFSO, 168,
133N, 818W, 16, 1007, XX, 34, NEQ, 0000, 0000, 0000, 0000, 1008,
92, 74, -27, 95, -26, N, 253, 16, 96, 118, 87, 113
TG, 0048, 2012080100_F150_138N_0805W_FOF, 2012080100, 03, GFSO, 174,
133N, 822W, 17, 1008, XX, 34, NEQ, 0000, 0000, 0000, 0000, 1010,
378, 56, -6, 100, -102, Y, 275, 24, 99, 139, 83,
105
```

```
TG, 0048, 2012080100_F150_138N_0805W_FOF, 2012080100, 03, GFSO, 180,
136N, 826W, 20, 1008, XX, 34, NEQ, 0000, 0000, 0000, 0000, 1009,
```

118, 57, -19, 123, -131, Y, 293, 29, 111, 150, 87,  
113  
TG, 0048, 2012080100\_F150\_138N\_0805W\_FOF, 2012080100, 03, GFSO, 192,  
140N, 835W, 14, 1008, XX, 34, NEQ, 0000, 0000, 0000, 0000, 1009,  
74, 62, -25, 137, -141, N, 294, 24, 108, 139, 96, 126  
TG, 0048, 2012080100\_F150\_138N\_0805W\_FOF, 2012080100, 03, GFSO, 204,  
143N, 846W, 17, 1009, XX, 34, NEQ, 0000, 0000, 0000, 0000, -999, -  
999, 159, -3, -41, -106, Y, 292, 30, 64, 73, 62,  
68  
TG, 0048, 2012080100\_F150\_138N\_0805W\_FOF, 2012080100, 03, GFSO, 216,  
153N, 859W, 14, 1009, XX, 34, NEQ, 0000, 0000, 0000, 0000, 1012,  
89, 155, 30, -19, -118, Y, 293, 31, 51, 56, 50, 55  
AL, 99L, 2012080100\_F000\_097N\_0430W\_99L, 2012080100, 03, GFSO, 000,  
105N, 430W, 28, 1012, XX, 34, NEQ, 0000, 0000, 0000, 0000, 1013,  
68, 92, -999, -9999, -9999, N, 279, 83, 221, 267, 207, 258  
AL, 99L, 2012080100\_F000\_097N\_0430W\_99L, 2012080100, 03, GFSO, 006,  
110N, 443W, 33, 1011, XX, 34, NEQ, 0000, 0000, 0000, 0000, 1013,  
178, 81, 41, 73, 112, Y, 286, 73, 265, 402, 230,  
352  
AL, 99L, 2012080100\_F000\_097N\_0430W\_99L, 2012080100, 03, GFSO, 012,  
113N, 459W, 33, 1012, XX, 34, NEQ, 0000, 0000, 0000, 0000, 1014,  
122, 68, 41, 278, 200, N, 282, 78, 302, 403, 257,  
358  
AL, 99L, 2012080100\_F000\_097N\_0430W\_99L, 2012080100, 03, GFSO, 018,  
116N, 474W, 34, 1010, XX, 34, NEQ, 0000, 0000, 0000, 0000, 1012,  
104, 61, 49, 379, 174, N, 280, 72, 283, 390, 225,  
291  
AL, 99L, 2012080100\_F000\_097N\_0430W\_99L, 2012080100, 03, GFSO, 024,  
115N, 488W, 31, 1011, XX, 34, NEQ, 0000, 0000, 0000, 0000, 1013,  
107, 72, 47, 427, 21, N, 271, 70, 255, 330, 189,  
239  
AL, 99L, 2012080100\_F000\_097N\_0430W\_99L, 2012080100, 03, GFSO, 030,  
117N, 501W, 29, 1009, XX, 34, NEQ, 0000, 0000, 0000, 0000, 1011,  
334, 79, 7, 494, 67, N, 278, 67, 240, 323, 175,  
233  
AL, 99L, 2012080100\_F000\_097N\_0430W\_99L, 2012080100, 03, GFSO, 036,  
121N, 511W, 36, 1011, XX, 34, NEQ, 0083, 0000, 0000, 0000, 1013,  
315, 62, 2, 471, 12, Y, 284, 62, 290, 505, 231,  
400  
AL, 99L, 2012080100\_F000\_097N\_0430W\_99L, 2012080100, 03, GFSO, 042,  
123N, 526W, 39, 1009, XX, 34, NEQ, 0085, 0000, 0000, 0073, 1011,  
114, 70, -10, 599, 217, Y, 277, 71, 359, 640, 302,  
536  
AL, 99L, 2012080100\_F000\_097N\_0430W\_99L, 2012080100, 03, GFSO, 048,  
124N, 542W, 43, 1010, XX, 34, NEQ, 0094, 0000, 0000, 0072, 1012,  
102, 70, -17, 620, 154, Y, 269, 78, 376, 627, 323,  
543  
AL, 99L, 2012080100\_F000\_097N\_0430W\_99L, 2012080100, 03, GFSO, 054,  
123N, 560W, 39, 1008, XX, 34, NEQ, 0080, 0000, 0000, 0081, 1011,  
216, 53, -31, 778, 249, Y, 270, 82, 336, 523, 280,  
472  
AL, 99L, 2012080100\_F000\_097N\_0430W\_99L, 2012080100, 03, GFSO, 060,  
121N, 579W, 39, 1010, XX, 34, NEQ, 0075, 0000, 0000, 0067, 1013,  
249, 56, -37, 810, 150, Y, 270, 84, 298, 457, 253,  
398

AL, 99L, 2012080100\_F000\_097N\_0430W\_99L, 2012080100, 03, GFSO, 066,  
121N, 596W, 34, 1009, XX, 34, NEQ, 0065, 0000, 0000, 0000, 1010,  
71, 65, -41, 729, 63, N, 273, 77, 264, 415, 208, 320  
AL, 99L, 2012080100\_F000\_097N\_0430W\_99L, 2012080100, 03, GFSO, 072,  
122N, 611W, 34, 1010, XX, 34, NEQ, 0061, 0000, 0000, 0000, 1012,  
146, 60, -34, 882, 35, N, 274, 71, 242, 376, 186,  
273  
AL, 99L, 2012080100\_F000\_097N\_0430W\_99L, 2012080100, 03, GFSO, 078,  
125N, 626W, 31, 1009, XX, 34, NEQ, 0000, 0000, 0000, 0000, 1011,  
228, 49, -48, 893, 12, N, 282, 74, 240, 342, 178,  
262  
AL, 99L, 2012080100\_F000\_097N\_0430W\_99L, 2012080100, 03, GFSO, 084,  
127N, 644W, 30, 1011, XX, 34, NEQ, 0000, 0000, 0000, 0000, 1013,  
125, 67, -23, 864, 3, N, 282, 80, 214, 289, 164,  
213  
AL, 99L, 2012080100\_F000\_097N\_0430W\_99L, 2012080100, 03, GFSO, 090,  
131N, 659W, 29, 1009, XX, 34, NEQ, 0000, 0000, 0000, 0000, 1010,  
66, 86, -32, 607, 86, N, 288, 73, 199, 251, 152, 204  
AL, 99L, 2012080100\_F000\_097N\_0430W\_99L, 2012080100, 03, GFSO, 096,  
134N, 674W, 29, 1010, XX, 34, NEQ, 0000, 0000, 0000, 0000, -999, -  
999, 108, -48, 688, 59, N, 282, 71, 194, 249, 140,  
178  
AL, 99L, 2012080100\_F000\_097N\_0430W\_99L, 2012080100, 03, GFSO, 102,  
137N, 692W, 31, 1009, XX, 34, NEQ, 0000, 0000, 0000, 0000, 1010,  
73, 88, -51, 423, 123, N, 282, 79, 182, 250, 142, 191  
AL, 99L, 2012080100\_F000\_097N\_0430W\_99L, 2012080100, 03, GFSO, 108,  
140N, 711W, 29, 1011, XX, 34, NEQ, 0000, 0000, 0000, 0000, 1012,  
83, 85, -45, 462, 49, N, 283, 84, 159, 217, 112, 154  
AL, 99L, 2012080100\_F000\_097N\_0430W\_99L, 2012080100, 03, GFSO, 114,  
145N, 729W, 28, 1010, XX, 34, NEQ, 0000, 0000, 0000, 0000, 1012,  
83, 149, -74, 327, 174, N, 287, 80, 143, 204, 87, 125

## 7. THE IDEALIZED HWRF FRAMEWORK

A mass-consistent idealized tropical cyclone initialization is available within the HWRF framework. The idealized simulation is configured for the operational HWRF triple-domain configuration with grid spacing of 13.5-, 4.5-, and 1.5 km. The sea-surface temperature is constant in time and space (currently 302 °K) as ocean coupling is not yet supported for the idealized configuration in HWRF. Initial conditions are specified using an idealized vortex superposed on a base-state quiescent sounding.

To initialize the idealized vortex, the nonlinear balance equation in the pressure-based sigma coordinate system described in Wang (1995), and reported briefly in Bao et al. (2012) and Gopalakrishnan et al. (2011, 2013), is solved within the rotated latitude–longitude E-grid framework. Sundqvist (1975) first used the balance equation to determine the wind (in terms of stream function) and the mass field (geopotential height). Kurihara and Bender (1980) adopted the inverse-balance procedure to obtain the mass field from the wind field and then solved for surface pressure at the lower boundary of the sigma coordinates and geopotential elsewhere. A variant of this procedure, discussed in Wang (1995), is adopted in the HWRF system.

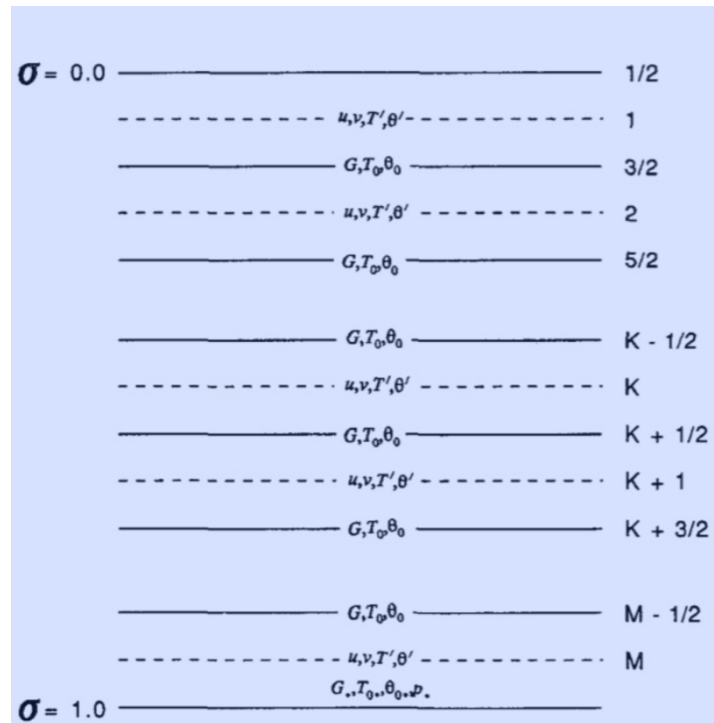


Figure 7.1. Vertical structure of the pressure-sigma coordinate used to create the idealized vortex.

Figure 7.1 provides an overview of the vertical structure of the sigma coordinate system used in the idealized initialization. The atmosphere is divided into M layers. The initial base-state temperature ( $T_0$ ), along with the forcing term G that approximates the momentum fields, is provided at the interface. The zonal (u) and meridional (v) wind components, along with the temperature perturbation ( $T'$ ) from the initial base state, are computed at half levels between the interfaces. The forcing term and the pressure at the

lower boundary ( $\sigma=1$ ) are represented by  $G_d$  and  $p_*$ , respectively. The base-state temperature and moisture fields, required in the hydrostatic equation to compute the geopotential from temperature and pressure, are prescribed in file *sound.d*. Wang (1995) provides an extensive overview of the initialization procedure. We describe here only the relevant equations as used in the code *module\_initialize\_tropical\_cyclone.F*

The initial wind field, in cylindrical polar coordinates, is prescribed at each sigma level by:

$$V(\mathbf{r}, \sigma) = V_m(\mathbf{r}/r_m) \sin(\pi \sigma/2) \exp\{1 - (\mathbf{r}/r_m)^b\} / b \quad (7.1)$$

where  $V_m$  is the maximum wind at radius  $r_m$ . Both these variables are supplied in file *input.d*. Parameter  $b$  is set to 1. The momentum field is a function of the  $u$  and  $v$  wind components and is given by:

$$G(\mathbf{u}, \mathbf{v}) = 2J(\mathbf{u}, \mathbf{v}) + f\zeta - u\mathbf{v} \quad (7.2)$$

where  $J$  is the Jacobian,  $f$  is the Coriolis parameter,  $\zeta$  is the vorticity and  $\mathbf{\beta}$  is the meridional gradient of the Coriolis parameter.

$$\nabla^2 \ln(p_*) = G_d / RT_{0d} \quad (7.3)$$

The pressure at  $\sigma=1$  is obtained by solving the Poisson equation where subscript  $d$  denotes the variable evaluated at  $\sigma=1$  and  $R$  is the gas constant. The temperature perturbations at the sigma levels are determined from solving the Poisson equation:

$$\nabla^2 T'_k = \nabla \cdot [(\partial T' / \partial \ln \sigma) \nabla \ln p_*]_k + [(\partial T_0 / \partial \ln \sigma) \nabla^2 \ln p_*]_k - [\partial G / R \partial \ln \sigma]_k \quad (7.4)$$

Finally, using the hydrostatic approximation, the geopotential heights are obtained from the total temperature and moisture fields.

Even though generation of the idealized initial conditions is based on the base-state sounding provided in file *sound.d* and on the vortex properties specified in file *input.d*, it is still necessary to provide the model with initial and boundary conditions from the GFS. The GFS-based initial and boundary conditions, processed through WPS, are overwritten with the idealized initialization in the *ideal\_nmm\_tropical\_cyclone* code as explained in the HWRF User's Guide. The lateral boundary conditions used in the HWRF idealized simulation are the same as used in real data cases. This practice inevitably leads to some reflection when gravity waves emanating from the vortex reach the outer domain lateral boundaries.

Tropical cyclone landfalling capability is also available in the idealized HWRF framework. To avoid the spurious convection over land and instability due to gravity waves bouncing off the lateral boundaries, a moving land surface is incorporated. Instead of introducing an environmental flow to move the tropical cyclones over land, land surface is moved underneath the vortex to realize relative landfall (similar to idealized HWRF configuration in Halliwell et al. (2015) where ocean-only experiments were conducted). The apparent speed at which landfall is realized can be altered in the source

code and is explained in the HWRF User's Guide. Currently only the GFDL Slab land-surface physics option is supported for landfall capability and efforts are underway to include other land-surface physics options. A namelist file for land-surface configuration introduces a switch for landfalling capability, specifies the type of land surface, initial land-surface temperature to be used over land. The default configuration introduces a homogeneous land surface but can be modified to account for heterogeneity through the source code. The direction of land motion can also be chosen. Two options are available – West to East or East to West. A complete explanation of the options and configurations available for landfalling capability is available in the HWRF User's Guide.

In the experiments described by Bao et al. (2012) and Gopalakrishnan et al. (2011, 2013), the simulations were performed on an f-plane centered at 12.5°N. The idealized vortex initial intensity was 20 m s<sup>-1</sup> with a radius of maximum winds of about 90 km, embedded in a uniform easterly flow of 4 m s<sup>-1</sup> or in a quiescent ambient. The base-state temperature and humidity profile was based on Jordan's Caribbean sounding (Gray et al. 1975). In their experiments, the sea-surface temperature was set to 302 °K, and no land was present in the domain.

Variables that can be customized for the HWRF idealized capability are the base-state sounding thermodynamic structure, the choice of f- or  $\beta$ -plane, the latitude of the storm, the radius of maximum wind, and the maximum wind speed. Sea-surface temperature can be changed in the source code. Additional settings may be changed by altering the source code, but these changes are not currently part of the code supported by the DTC. Examples of possible changes are the introduction of base-state non-zero winds, land surface, or coupling to an ocean model. Finally, all the operational physics, as well as the supported experimental physics options in HWRF, can be used in the idealized framework.

## 8. REFERENCES

- Alaka, G. J., X. Zhang, S. G. Gopalakrishnan, S. B. Goldenberg, and F. D. Marks, 2017: Performance of basin-scale HWRF tropical cyclone track forecasts. *Wea. Forecasting*, **32**, 1253–1271, <https://doi.org/10.1175/WAF-D-16-0150.1>
- Aligo, E., Ferrier, B., J. Carley, E. Rodgers, M. Pyle, S. J. Weiss, and I. L. Jirak, 2014: Modified microphysics for use in high resolution NAM forecasts. 27 AMS Conference on Severe Local Storms. 3-7 November, Madison, WI.
- Aligo, E., Ferrier, B., G. Thompson, J. R. Carley, E. Rogers, J. Dimego, 2017: The New-Ferrier-Aligo Microphysics in the NCEP 3-km NAM nest, 97<sup>th</sup> AMS Annual Meeting, 21-26 January, Seattle, WA.
- Andersson, E and H. Järvinen, 1999: Variational quality control. *Quart. J. Roy. Meteor. Soc.*, **125**: 697–722.
- Arakawa, A. and W. H. Schubert, 1974: Interaction of a Cumulus Cloud Ensemble with the Large-Scale Environment, Part I. *J. Atmos. Sci.*, **31**, 674-701.
- Bao, J.-W., S. G. Gopalakrishnan, S. A. Michelson, F. D. Marks, and M. T. Montgomery, 2012: Impact of physics representations in the HWRF on simulated hurricane structure and pressure–wind relationships. *Mon. Wea. Rev.*, **140**, 3278-3299.
- Barker, H., J.N.S. Cole, J.-J. Morcrette, R. Pincus, P. Raisanen, Monte Carlo Independent Column Approximation (McICA), 2007: Up and running in North America and Europe, Talk presented at the 17th Atmospheric Radiation Measurement (ARM) Science Team Meeting, Monterey, CA, March 26-30, 2007.
- Barnes, S. L., 1964: A technique for maximizing details in numerical weather map analysis. *J. Appl. Meteor.*, **3**, 396-409.
- Barnes, S. L., 1973: Mesoscale objective analysis using weighted time-series observations. NOAA Tech. Memo. ERL NSSL-62, National Severe Storms Laboratory, Norman, OK 73069, 60 pp. [NTIS COM-73-10781].
- Bell, Michael M., M. T. Montgomery, and K. A. Emanuel, 2012, Air–Sea Enthalpy and Momentum Exchange at Major Hurricane Wind Speeds Observed During CBLAST." *Journal of the Atmospheric Sciences* **69**, 3197-3222
- Bender, M. A. and I. Ginis, 2000: Real case simulation of hurricane-ocean interaction using a high-resolution coupled model: Effects on hurricane intensity. *Mon. Wea. Rev.*, **128**, 917-946.
- Bender, M. A., I. Ginis, R. Tuleya, B. Thomas and T. Marchok, 2007: The operational GFDL Coupled Hurricane-Ocean Prediction System and a summary of its performance. *Mon. Wea. Rev.*, **135**, 3965-3989.

- Bi, X., and Coauthors, 2015: Observed drag coefficients in high winds in the near offshore of the South China Sea. *J. Geophys. Res. Atmos.*, **120**, 6444–6459, doi:<https://doi.org/10.1002/2015JD023172>.
- Bister, M. and K. A. Emanuel, 1998: Dissipative heating and hurricane intensity. *Meteor. Atmos. Phys.*, **65**, 233-240.
- Biswas, M.K., L. Carson, K. Newman, L. Bernardet, E. Kalina, E. Grell, and J. Frimel, 2018: Community HWRF Users's Guide v4.0a. 160 pp.
- Black, P. G., E. A. D'Asaro, W. M. Drennan, J. R. French, T. B. Sanford, E. J. Terrill, P. P. Niiler, E. J. Walsh and J. Zhang, 2007: Air-Sea Exchange in Hurricanes: Synthesis of Observations from the Coupled Boundary Layer Air-Sea Transfer Experiment. *Bull. Amer. Meteor. Soc.*, **88**, 357-374.
- Blumberg, A. F. and G. L. Mellor, 1987: A description of a three-dimensional coastal ocean circulation model. *Three-Dimensional Coastal Ocean Models*. N. Heaps, Ed., Vol. 4, Amer. Geophys. Union, 1-16.
- Boyer, T. P. and S. Levitus, 1997: *Objective Analysis of Temperature and Salinity for the World Ocean on a 1/4 Grid*. NOAA Atlas NESDIS 11, 62 pp.
- Bu, Y., 2015: Influence of cloud-radiative forcing and the planetary boundary layer on tropical cyclone structure, PhD Thesis submitted to UCLA., PhD Thesis submitted to UCLA.
- Buehner, M., 2005: Ensemble-derived stationary and flow-dependent background-error covariances: Evaluation in a quasi-operational NWP setting. *Quart. J. Roy. Meteor. Soc.*, **131**, 1013–1043.
- Carnes, M. R., 2009: Description and evaluation of GDEM-V 3.0. Naval Research Laboratory, Stennis Space Center, MS 39529, 21 pp. [NRL/MR/7330--09-9165].
- Chassignet, E. P., H. E. Hurlburt, E. J. Metzger, O. M. Smedstad, J. Cummings, G. R. Halliwell, R. Bleck, R. Baraille, A. J. Wallcraft, C. Lozano, H. L. Tolman, A. Srinivasan, S. Hankin, P. Cornillon R. Weisberg, A. Barth, R. He, F. Werner, and J. Wilkin, 2009: US GODAE: Global ocean prediction with the HYbrid Coordinate Ocean Model (HYCOM). *Oceanogr.*, **22**, 64-75.
- Chen, F., and Coauthors, 1996: Modeling of land-surface evaporation by four schemes and comparison with FIFE observations. *J. Geophys. Res.*, **101**, 7251–7268.
- Chen, F., and J. Dudhia, 2001: Coupling an advanced land surface–hydrology model with the Penn State–NCAR MM5 modeling system. Part I: Model description and implementation. *Mon. Wea. Rev.*, **129**, 569–585, doi:10.1175/1520-0493(2001)129<0569:CAALSH>2.0.CO;2.
- Chen, F., J. Dudhia, Z. Janjic, and M. Baldwin, 1997: Coupling a land-surface model to the NCEP mesoscale Eta model. Preprints, *13th Conf. on Hydrology*, Long Beach, CA, Amer. Meteor. Soc., 99–100.

- Cintineo, R., Otkin, J.A., Xue, M., Kong, F., 2014. Evaluating the performance of planetary boundary layer and cloud microphysical parameterization schemes in convection-permitting ensemble forecasts using synthetic GOES-13 satellite observations. *Mon. Weather Rev.*, **142**, 163–182.
- Cummings, J. A., 2005: Operational multivariate ocean data assimilation. *Quart. J. Royal Meteor. Soc.*, **131**, 3583-3604.
- Cummings, J.A. and O. M. Smedstad, 2013: *Variational data assimilation for the global ocean. Data Assimilation for Atmospheric, Oceanic and Hydrologic Applications*, Vol. II, S. Park and L. Xu, Eds., Springer, 303–343.
- Derber, J.C., and W.-S Wu, 1998: The use of TOVS cloud-cleared radiances in the NCEP SSI analysis system. *Mon. Wea. Rev.*, **126**, 2287-2299.
- Edson, J. B., and Coauthors, 2013: On the exchange of momentum over the open ocean. *J. Phys. Oceanogr.*, **43**, 1589–1610, doi:<https://doi.org/10.1175/JPO-D-12-0173.1>.
- Eikenberg, S., C. Kohler, A. Seifert, and S. Crewell, 2015: How microphysical choices affect simulated infrared brightness temperatures. *Atmos. Res.*, **156**, 67–79.
- Ek, M. B., K. E. Mitchell, Y. Lin, E. Rogers, P. Grunmann, V. Koren, G. Gayno, and J. D. Tarpley, 2003: Implementation of Noah land surface model advancements in the National Centers for Environmental Prediction operational mesoscale Eta model, *J. Geophys. Res.*, 108(D22), 8851, doi:10.1029/2002JD003296.
- Fairall, C. W., E. F. Bradley, J. E. Hare, A. A. Grachev, and J. B. Edson, 2003: Bulk parameterization of air–sea fluxes: Updates and verification for the COARE algorithm. *J. Climate*, **16**, 571–591, doi:[https://doi.org/10.1175/1520-0442\(2003\)016<0571:BPOASF>2.0.CO;2](https://doi.org/10.1175/1520-0442(2003)016<0571:BPOASF>2.0.CO;2).
- Falkovich, A., I. Ginis and S. Lord, 2005: Ocean data assimilation and initialization procedure for the Coupled GFDL/URI Hurricane Prediction System. *J. Atmos. Oceanic Technol.*, **22**, 1918-1932.
- Ferrier, B.S., Y. Jin, Y. Lin, T. Black, E. Rogers, and G. DiMego, 2002: Implementation of a new grid-scale cloud and precipitation scheme in the NCEP Eta model, 19th Conf. on weather Analysis and Forecasting/15th Conf. on Numerical Weather Prediction.
- French, J.R., W.M. Drennan, J.A. Zhang, and P.G. Black, 2007: Turbulent fluxes in the boundary layer. Part I: Momentum flux. *J. Atmos. Sci.*, **64**, 1089-1102.
- Fu, Q, P. Yang, and W. B. Sun, 1998: An Accurate Parameterization of the Infrared Radiative Properties of Cirrus Clouds for Climate Models. *J. Climate*, **11**, 1998, 2223–2237.
- Gall, R., F. Toepfer, F. Marks, E. Rappaport, A. Aksoy, S. Aberson, J.W. Bao, M. Bender, S. Benjamin, L. Bernardet, M. Biswas, B. Brown, J. Cangialosi, C. Davis, M. DeMaria, J. Doyle, M. Fiorino, J. Franklin, I. Ginis, S. Gopalakrishnan, T. Hamill, R. Hodur, H.S. Kim, T. Krishnamurti, P. Kucera, Y. Kwon, W. Lapenta,

- N. Lett, S. Lord, T. Marchok, P. McCaslin, E. Mifflin, L. Nance, C. Reynolds, V. Tallapragada, H. Tolman, R. Torn, G. Vandenberghe, T. Vukicevic, X. Wang, Y. Weng, J. Whittaker, R. Yablonsky, D-L. Zhang, F. Zhang, J. Zhang, X. Zhang: 2012 HFIP R & D Activities Summary, 2013: Recent Results and Operational Implementation (available at [http://www.hfip.org/documents/HFIP\\_2012\\_Annual\\_Report\\_Final.pdf](http://www.hfip.org/documents/HFIP_2012_Annual_Report_Final.pdf))
- Gamache, J. F., F. D. Marks Jr., and F. Roux, 1995: Comparison of three airborne Doppler sampling techniques with airborne in situ wind observations in Hurricane Gustav (1990). *J. Atmos. Oceanic Technol.*, **12**, 171–181.
- Gaspari, G., and S. E. Cohn, 1999: Construction of correlation functions in two and three dimensions. *Quart. J. Roy. Meteor. Soc.*, **125**, 723–757.
- Gopalakrishnan, S. G., F. Marks, X. Zhang, J.-W. Bao, K.-S. Yeh, and R. Atlas, 2011: The experimental HWRF System: a study on the influence of horizontal resolution on the structure and intensity changes in tropical cyclones using an idealized framework. *Mon. Wea. Rev.*, **139**, 1762–1784.
- Gopalakrishnan, S. G., F. Marks Jr., J. A. Zhang, X. Zhang, J.-W. Bao, and V. Tallapragada, 2013: Study of the impacts of vertical diffusion on the structure and intensity of the tropical cyclones using the high-resolution HWRF system. *J. of the Atmos. Sci.*, **70**, 524–541.
- Gray, W., E. Ruprecht, and R. Phelps, 1975: Relative humidity in tropical weather systems. *Mon. Wea. Rev.*, **103**, 685–690.
- Grell, G.A., 1993: Prognostic evaluation of assumptions used by cumulus parameterizations. *Mon. Wea. Rev.*, **121**, 764–787.
- Grell, G. A. and S.R. Freitas, 2017: A scale and aerosol aware stochastic convective parameterization for weather and air quality modeling, 2014, *Atmos. Chem. Phys.*, 14, 5233–5250, doi:10.5194/acp-14-5233-2014.
- Han, J. and H.-L. Pan, 2011: Revision of Convection and Vertical Diffusion Schemes in the NCEP Global Forecast System. *Wea. Forecasting*, **26**, 520–533.
- Han, J., M. Witek, J. Teixeira, R. Sun, H.-L. Pan, J. K. Fletcher, and C. S. Bretherton, 2016: Implementation in the NCEP GFS of a Hybrid Eddy-Diffusivity Mass-Flux (EDMF) Boundary Layer Parameterization with Dissipative Heating and Modified Stable Boundary Layer Mixing. *Weather and Forecasting*, **31**, 341–352.
- Han, Jongil, W. Wang, Y. Kwon, S. Hong, V. Tallapragada and F. Yang 2017: Updates in the NCEP GFS Cumulus Convection Schemes with Scale and Aerosol Awareness, *Wea. Forecasting* (In review).
- Harris, B. A. and G. Kelly, 2001: A satellite radiance-bias correction scheme for data assimilation. *Q.J.R. Meteorol. Soc.*, **127**: 1453–1468.  
doi: 10.1002/qj.49712757418
- Hart, R.E., 2003: A cyclone phase space derived from thermal wind and thermal asymmetry. *Mon. Wea. Rev.*, **131**, 585–616.

- Halliwell, G.R., S. Gopalakrishnan, F. Marks, and D. Willey, 2015. Idealized study of ocean impacts on tropical cyclone intensity forecasts. *Monthly Weather Review*, 143(4):1142-1165, doi:10.1175/MWR-D-14-00022.1
- Holthuijsen L. H., M. D. Powell, J. D. Pietrzak, 2012: Wind and waves in extreme hurricanes. *J. Geoph. Res.* **117**:C09003-1-15
- Hong, S.-Y. and H.-L. Pan, 1996: Nonlocal boundary layer vertical diffusion in a medium-range forecast model. *Mon. Wea. Rev.*, **124**, 2322-2339.
- Hong, S.-Y. and H.-L. Pan, 1998: Convective trigger function for a mass flux cumulus parameterization scheme. *Mon. Wea. Rev.*, **126**, 2621-2639.
- Hu, Y. X., and K. Stamnes, 1993: An accurate parameterization of the radiative properties of water clouds suitable for use in climate models. *J. Climate*, **6**, 728-742.
- Iacono, M. J., J. S. Delamere, E. J. Mlawer, M. W. Shephard, S. A. Clough, and W. D. Collins, 2008: Radiative forcing by long-lived greenhouse gases: Calculations with the AER radiative transfer models, *J. Geophys. Res.*, **113**, D13103, doi:10.1029/2008JD009944.
- Janjic, Z. I., 1990a: The step-mountain coordinate: physical package. *Mon. Wea. Rev.*, **118**, 1429-1443.
- Janjic, Z. I., 1990b: The step-mountain coordinate model: further developments of the convection, viscous sublayer and turbulence closure schemes. *Mon. Wea. Rev.* **122**, 927-945.
- Janjic, Z. I., 1996: The Mellor-Yamada level 2.5 scheme in the NCEP Eta model. *Preprints*, 11<sup>th</sup> Conf. on Numerical Weather Prediction, Norfolk, VA, 19-23 August 1996; Amer. Meteor. Soc. Boston, MA, 333-334.
- Janjic, Z. I., 2002: Nonsingular Implementation of the Mellor–Yamada Level 2.5 Scheme in the NCEP Meso model, *NCEP Office Note*, No. 437, 61 pp.
- Janjic, Z. I., R. Gall and M. E. Pyle, 2010: Scientific Documentation for the NMM Solver. NCAR Technical Note NO. NCAR/TN–477+STR, 1-125, 53 pp. (Available from NCAR, P.O. Box 3000, Boulder, CO 80307)
- Jarosz E, D. A. Mitchell, D. W. Wang, W. J. Teague, 2007: Bottomup determination of air-sea momentum exchange under a major tropical cyclone. *Science* **315**, 1707–1709
- Jordi, A., and D.-P. Wang, 2012: sbPOM: A parallel implementation of Princeton Ocean Model. *Environ. Modelling & Software*, **38**, 59-61.
- Kleist, D. T., D. F. Parrish, J. C. Derber, R. Treadon, R.M. Errico and R. Yang, 2009: Introduction of the GSI into the NCEP Global Data Assimilation System. *Mon. Wea. Rev.*, **24**, 1691-1705.

- Koren, V., J. Schaake, K. Mitchell, Q.-Y. Duan, and F. Chen, 1999: A parameterization of snowpack and frozen ground intended for NCEP weather and climate models. *J. Geophys. Res.*, **104**, 19 569–19 585.
- Kurihara Y. and R. E. Tuleya, 1974: Structure of a tropical cyclone developed in a three-dimensional numerical simulation model. *J. Atmos. Sci.*, **31**, 893–919.
- Kurihara, Y., and M. A. Bender, 1980: Use of a movable nested-mesh model for tracking a small vortex. *Mon. Wea. Rev.*, **108**, 1792–1809.
- Kwon Y. C., and S. Lord, B. Lapenta, V. Tallapragada, Q. Liu and Z. Zhang, 2010: Sensitivity of Air-Sea Exchange Coefficients (Cd and Ch) on Hurricane Intensity. [29th Conference on Hurricanes and Tropical Meteorology](#), **13C.1**
- Lin, Y.-L., 2007. *Mesoscale Dynamics*. Cambridge University Press, U.K.
- Liu, Q., N. Surgi, S. Lord, W.-S. Wu, S. Parrish, S. Gopalakrishnan, J. Waldrop and J. Gamache, 2006: Hurricane Initialization in HWRF Model. *Preprints*, 27th Conference on Hurricanes and Tropical Meteorology, Monterey, CA.
- Lorenc, C., 1981: A global three-dimensional multivariate statistical interpolation scheme. *Mon. Wea. Rev.*, **109**, 701–721.
- Lorenc, A. C., 2003: The potential of the ensemble Kalman filter for NWP—A comparison with 4D-VAR. *Quart. J. Roy. Meteor. Soc.*, **129**, 3183–3203.
- Ma, H.-Y., and Coauthors, 2014: On the Correspondence between mean forecast errors and climate errors in CMIP5 Models. *J. Climate*, **27**, 1781–1798.
- Mahrt, L., and H. L. Pan, 1984: A two-layer model of soil hydrology. *Bound.-Layer Meteor.*, **29**, 1–20.
- Mahrt, L., and M. Ek, 1984: The influence of atmospheric stability on potential evaporation. *J. Climate Appl. Meteor.*, **23**, 222–234.
- Marchok, T. P., 2002: How the NCEP tropical cyclone tracker works. *Preprints*, 25<sup>th</sup> Conf. on Hurricanes and Tropical Meteorology, Amer. Meteor. Soc., San Diego, CA, 21–22.
- McNally, A. P. (2000), Estimates of short-range forecast-temperature error correlations and the implications for radiance-data assimilation. *Q.J.R. Meteorol. Soc.*, **126**: 361–373. doi: 10.1002/qj.49712656218
- Mehra, A. and I. Rivin, 2010: A real time ocean forecast system for the North Atlantic Ocean. *Terr. Atmos. Ocean. Sci.*, **21**, 211–228, doi: 10.3319/TAO.2009.04.16.01(IWNOP)
- Mellor, G. L. and T. Yamada, 1982: Development of a turbulence closure model for geophysical fluid problems. *Rev. Geophys. Space Phys.*, **20**, 851–875.
- Mellor, G. L., 1991: An equation of state for numerical models of oceans and estuaries. *J. Atmos. Oceanic Technol.*, **8**, 609–611.

- Mellor, G. L., 2004: *Users guide for a three-dimensional, primitive equation, numerical ocean model (June 2004 version)*. Prog. in Atmos. and Ocean. Sci, Princeton University, 56 pp.
- Michalakes, J., J. Dudhia, D. Gill, T. Henderson, J. Klemp, W. Skamarock and W. Wang, 2004: The Weather Research and Forecast Model: Software Architecture and Performance. *Eleventh ECMWF Workshop on the Use of High Performance Computing in Meteorology*, Reading, U.K., Ed. George Mozdzyński.
- Mitchell, K., 2005: The community Noah Land Surface Model (LSM). [http://www.ral.ucar.edu/research/land/technology/lsm/noah/Noah\\_LSM\\_USERGUIDE\\_2.7.1.pdf](http://www.ral.ucar.edu/research/land/technology/lsm/noah/Noah_LSM_USERGUIDE_2.7.1.pdf)
- Mocko, D. M. and W. R. Cotton, 1995: Evaluation of fractional cloudiness parameterizations for use in a mesoscale model. *J. Atmospheric Sciences*, **52**, 2284-2901.
- Pan, H.-L., 2003: The GFS Atmospheric Model. NCEP Office Note, No. 442, 14 pp. (Available from NCEP, 5200 Auth Road, Washington, DC 20233)
- Pan, H.-L. and J. Wu, 1995: Implementing a Mass Flux Convection Parameterization Package for the NMC Medium-Range Forecast Model. NMC Office Note, No. 409, 40 pp. (Available from NCEP, 5200 Auth Road, Washington, DC 20233)
- Pan, H.-L., and L. Mahrt, 1987: Interaction between soil hydrology and boundary-layer development. *Bound.-Layer Meteor.*, **38**, 185–202.
- Phillips, N. A., 1957: A coordinate system having some special advantages for numerical forecasting. *J. Meteor.*, **14**, 184-185.
- Pincus, R., C. Hannay, S. A. Klein, K.-M. Xu, and R. Hemler, 2005: Overlap assumptions for assumed probability distribution function cloud schemes in large-scale models, *J. Geophys. Res.*, 110, D15S09, doi:10.1029/2004JD005100.
- Pincus, R., H. W. Barker, J.-J. Morcrette, 2003: A fast, flexible, approximate technique for computing radiative transfer in inhomogeneous cloud fields, *J. Geophys. Res.*, 108, D13.
- Potter, H., C. O. Collins, W. M. Drennan, and H. C. Graber, 2015: Observations of wind stress direction during Typhoon Chaba (2010). *Geophys. Res. Lett.*, **42**, 9898–9905, doi:<https://doi.org/10.1002/2015GL065173>.
- Powell, M. D., P. J. Vickery and T. A. Reinhold, 2003: Reduced drag coefficient for high wind speeds in tropical cyclones, *Nature*, **422**, 279-283.
- Price, J., 1981: Upper ocean response to a hurricane. *J. Phys. Oceanogr.*, **11**, 153-175.
- Reynolds, R. W. and T. M. Smith, 1994: Improved global sea surface temperature analyses using optimum interpolation. *J. Climate*, **7**, 929-948.
- Rogers, E., T. Black, B. Ferrier, Y. Lin, D. Parrish, and G. DiMego, 2001: Changes to the NCEP Meso Eta Analysis and Forecast System: Increase in resolution, new cloud

- microphysics, modified precipitation assimilation, modified 3DVAR analysis. Technical Procedures Bulletin.  
<http://www.emc.ncep.noaa.gov/mmb/mmbppl/eta12tpb/>.
- Richter DH, R. Bohac, D. P. Stern, 2016: An assessment of the flux profile method for determining air-sea momentum and enthalpy fluxes from dropsonde data in tropical cyclones. *J Atmos Sci* 73:2665–2682. doi:[10.1175/JAS-D-15-0331.1](https://doi.org/10.1175/JAS-D-15-0331.1)
- Ryan, B. F., 1996: On the global variation of precipitating layer clouds. *Bull. Amer. Meteor. Soc.*, **77**, 53–70.
- Schaake, J. C., V. I. Koren, Q. Y. Duan, K. Mitchell, and F. Chen, 1996: A simple water balance model (SWB) for estimating runoff at different spatial and temporal scales. *J. Geophys. Res.*, **101**, 7461–7475.
- Sirutis, J. J. and K. Miyakoda, 1990: Subgrid scale physics in 1-month forecasts. Part I: Experiment with four parameterization packages. *Mon. Wea. Rev.*, 118(5), 1043–1064.
- Skamarock, W. C., J. B. Klemp, J. Dudhia, D. O. Gill, D. M. Barker, M. G. Duda, X–Y. Huang, W. Wang and J. G. Powers, 2008: A Description of the Advanced Research WRF Version 3, NCAR Technical Note NO. NCAR/TN–475+STR, 1–125
- Smagorinsky, J., 1963: General circulation experiments with primitive equations. Part I: The basic experiments. *Mon. Wea. Rev.*, **91**, 99–164.
- Sundqvist, H., 1975: Initialization for models using sigma as the vertical coordinate. *J. Appl. Meteor.*, **14**, 153–158.
- Sundqvist, H., E. Berge and J.E. Krisjansson, 1989: Condensation and cloud parameterization studies with a mesoscale numerical weather prediction model. *Mon. Wea. Rev.*, **117**, 1641–1657.
- Teague, W. J, M. J. Carron and P. J. Hogan, 1990: A comparison between the Generalized Digital Environmental Model and Levitus climatologies. *J. Geophys. Res.*, **95**, 7167–7183.
- Trahan, S. and L. Sparling, 2012: An analysis of NCEP tropical cyclones vitals and potential effects on forecasting models. *Weather and Forecasting*, **27**, 744–756..
- Troen, I. and L. Mahrt, 1986: A simple model of the atmospheric boundary layer: Sensitivity to surface evaporation. *Bound. Layer Meteor.*, **37**, 129–148.
- Vitart, F., J. L. Anderson, and W. F. Stern, 1997: Simulation of the interannual variability of tropical storm frequency in an ensemble of GCM integrations. *J. Climate*, **10**, 745–760.
- Wang, X., 2010: Incorporating ensemble covariance in the Gridpoint Statistical Interpolation (GSI) variational minimization: A mathematical framework. *Mon. Wea. Rev.*, **138**, 2990–2995.

- Wang W., J. Sippel, S. Abarca, L. Zhu, B. Liu, Z. Zhang, A. Mehra, and V. Tallapragada, 2018, Improving the HWRF simulations of surface wind and inflow angle in the eyewall area. *Wea and Forecasting*, **33**, 887-898, <https://doi.org/10.1175/WAF-D-17-0115.1> .
- Wang, X., C. Snyder, and T. M. Hamill, 2007a: On the theoretical equivalence of differently proposed ensemble/3D-Var hybrid analysis schemes. *Mon. Wea. Rev.*, **135**, 222–227.
- Wang, X., T. M. Hamill, J. S. Whitaker, and C. H. Bishop, 2007b: A comparison of hybrid ensemble transform Kalman filter-OI and ensemble square-root filter analysis schemes. *Mon. Wea. Rev.*, **135**, 1055–1076.
- Wang, Y., 1995: An inverse balance equation in sigma coordinates for model initialization. *Mon. Wea. Rev.*, **123**, 482–488.
- Yablonsky, R. M. and I. Ginis, 2008: Improving the ocean initialization of coupled hurricane-ocean models using feature-based data assimilation. *Mon. Wea. Rev.*, **136**, 2592-2607.
- Yablonsky, R. M. and I. Ginis, 2009: Limitation of one-dimensional ocean models for coupled hurricane-ocean model forecasts. *Mon. Wea. Rev.*, **137**, 4410–4419.
- Yablonsky, R. M. and I. Ginis, 2013: Impact of a warm ocean eddy's circulation on hurricane-induced sea surface cooling with implications for hurricane intensity. *Mon. Wea. Rev.*, **141**, 997-1021.
- Yablonsky, R. M., I. Ginis, B. Thomas, 2015a: Ocean modeling with flexible initialization for improved coupled tropical cyclone-ocean prediction, *Environmental Modelling & Software*, **67**, 26-30.
- Yablonsky, R. M., I. Ginis, B. Thomas, V. Tallapragada, D. Sheinin, and L. Bernardet, 2015b: Description and analysis of the ocean component of NOAA's operational Hurricane Weather Research and Forecasting (HWRF) Model. *J. Atmos. Oceanic Technol.*, **32**, 144–163. doi: <http://dx.doi.org/10.1175/JTECH-D-14-00063.1>
- Yablonsky, R. M., I. Ginis, E. W. Uhlhorn and A. Falkovich, 2006: Using AXBTs to improve the performance of coupled hurricane–ocean models. *Preprints, 27th Conf. on Hurricanes and Tropical Meteorology*, Monterey, CA, Amer. Meteor. Soc., 6C.4. (Available online at <http://ams.confex.com/ams/pdfpapers/108634.pdf>).
- Zhao, Z.-K., C.-X. Liu, Q. Li, G.-F. Dai, Q.-T. Song, and W.-H. Lv, 2015: Typhoon air-sea drag coefficient in coastal regions, *J. Geophys. Res. Oceans*, **120**, 716–727, doi:[10.1002/2014JC010283](https://doi.org/10.1002/2014JC010283).
- Zhu, Y., J. Derber, A. Collard, D. Dee, R. Treadon, G. Gayno, and J. A. Jung, 2014: Enhanced radiance bias correction in the National Centers for Environmental Prediction's Gridpoint Statistical Interpolation data assimilation system. *Quart. J. Roy. Meteor. Soc.*, **140**, 1479-1492.



## 9. ACRONYMS

3D-VAR	Three-Dimensional Variational data assimilation system
AL	Northern Atlantic basin
AOML	Atlantic Oceanographic and Meteorological Laboratory
AXBT	Airborne eXpendable BathyThermograph
CFL	Courant-Friedrichs-Lewy
CP	Central Pacific
CPHC	Central Pacific Hurricane Center
DSHP	Decay Statistical Hurricane Intensity Prediction System
DTC	Developmental Testbed Center
ECMWF	European Center for Medium Range Weather Forecast
EDMF	Eddy Diffusivity Mass-Flux
EMC	Environmental Modeling Center
EnKF	Ensemble Kalman Filter
EP	Eastern North Pacific basin
FA	Ferrier-Aligo
FV3	Finite-Volume Cubed-Sphere
GDAS	Global Data Assimilation System
GFDL	Geophysical Fluid Dynamics Laboratory
GFS	Global Forecast System
GSI	Gridpoint Statistical Interpolation
HAFS	Hurricane Analysis and Forecast System
HDAS	HWRF Data Assimilation System
HDOBS	High-Density Observations
HFIP	Hurricane Forecast Improvement Program
HMON	Hurricane in a Multi-scale Ocean-coupled Non-hydrostatic model
HRD	Hurricane Research Division
HWRF	Hurricane Weather Research and Forecast System
HYCOM	Hybrid Coordinate Ocean Model
IAU	Incremental Analysis Updating
JTWC	Joint Typhoon Warning Center
LGEM	Linear Growth Equation Model
LSM	Land Surface Model
MPIPOM-TC	Message Passing Interface Princeton Ocean Model-Tropical Cyclone
MPMD	Multiple Program Multiple Data
MWW3	Multi-grid Wave Model
NAM	North America Mesoscale Model
NCEP	National Center for Environmental Prediction
NCO	NCEP Central Operations
NCODA	Navy Coupled Ocean Data Assimilation
NEMS	NOAA's Environmental Modeling System
NGGPS	Next-Generation Global Prediction System

NHC	National Hurricane Center
NIO	Northern Indian Ocean
NMM	Non-Hydrostatic Mesoscale Model
NOAA	National Oceanic and Atmospheric Administration
NOS	National Ocean Service
NUOPC	National Unified Operational Prediction Capability
NWS	National Weather Service
MPI	Message Passing Interface
PBL	Planetary Boundary Layer
RMW	Radius of Maximum Wind
ROCI	Radius of Outermost Closed Isobar
RRTMG	Rapid Radiative Transfer Model for GCMs
RTOFS	Real Time Ocean Forecast System
SASAS	Scale Aware Simplified Arakawa Schubert
SFMR	Stepped-Frequency Microwave Radiometer
SIO	Southern Indian Ocean
SIP	Strategic Implementation Plan
SP	Southern Pacific
SREF	Short-Range Ensemble Forecast
T&E	Testing and Evaluation
TC	Tropical Cyclone
TDR	Tail Doppler Radar
TDR	Tail Doppler Radar
UAV	Unmanned Aerial Vehicle
UFS	Unified Forecast System
UPP	Unified Post-Processor
URI	University of Rhode Island
WCOSS	Weather & Climate Operational Supercomputing System
WFO	Weather Forecast Office
WP	Western North Pacific basin
WPS	WRF Preprocessing System
WRF	Weather Research and Forecasting
WW3	Wave Watch III